

THEORY AND APPLICATIONS OF SURFACE
PLASMON RESONANCE SENSORS

A THESIS SUBMITTED TO
THE GRADUATE SCHOOL OF NATURAL AND APPLIED SCIENCES
OF
MIDDLE EAST TECHNICAL UNIVERSITY

BY

FURKAN ÖZDEMİRCAN

IN PARTIAL FULFILLMENT OF THE REQUIREMENTS
FOR
THE DEGREE OF MASTER OF SCIENCE
IN
ELECTRICAL AND ELECTRONICS ENGINEERING

FEBRUARY 2021

Approval of the thesis:

**THEORY AND APPLICATIONS OF SURFACE
PLASMON RESONANCE SENSORS**

submitted by **FURKAN ÖZDEMİRCAN** in partial fulfillment of the requirements
for the degree of **Master of Science in Electrical and Electronics Engineering,**
Middle East Technical University by,

Prof. Dr. Halil Kalıpçılar
Dean, Graduate School of **Natural and Applied Sciences** _____

Prof. Dr. İlkay Ulusoy
Head of the Department, **Electrical and Electronics
Engineering, METU** _____

Prof. Dr. Gönül (Turhan) Sayan
Supervisor, **Electrical and Electronics Engineering, METU** _____

Examining Committee Members:

Prof. Dr. Mustafa Kuzuoğlu
Electrical and Electronics Engineering, METU _____

Prof. Dr. Gönül (Turhan) Sayan
Electrical and Electronics Engineering, METU _____

Prof. Dr. Kemal Leblebicioğlu
Electrical and Electronics Engineering, METU _____

Assoc. Prof. Dr. Serdar Kocaman
Electrical and Electronics Engineering, METU. _____

Prof. Dr. Metin Sabuncu
Electrical and Electronics Engineering, Dokuz Eylül University _____

Date: 12.02.2021

I hereby declare that all information in this document has been obtained and presented in accordance with academic rules and ethical conduct. I also declare that, as required by these rules and conduct, I have fully cited and referenced all material and results that are not original to this work.

Name, Surname: Furkan Özdemircan

Signature :

ABSTRACT

THEORY AND APPLICATIONS OF SURFACE PLASMON RESONANCE SENSORS

Özdemircan, Furkan
Master of Science, Electrical and Electronics Engineering
Supervisor : Prof. Dr. Gönül (Turhan) Sayan

February 2021, 142 pages

In this thesis, the electromagnetic theory of the surface plasmon resonance (SPR) phenomenon and its applications in optical sensing are investigated. An SPR sensor's operation is based on the excitation of surface plasmon waves (SPWs) at an interface between two different media, a metal layer, and a dielectric layer, with real parts of dielectric constants having opposite signs. The presence of the SPR shows itself with a sharp minimum in the reflection curve of the sensor that is operated by either the angular interrogation approach or the wavelength interrogation approach. The minimum SPR reflection location is highly sensitive to variations in relative permittivity and thickness parameters of the material layers. Even small changes in any one of these parameters can be accurately sensed by measuring the corresponding shift in the minimum point of the SPR reflection curve's location. Using the prism-based coupling method for the excitation of SPWs, the three-layer SPR sensor structure composed of the prism, the thin metal film, and the bulk dielectric layer is investigated by both analytical solutions and numerical simulations. Dielectric function models of different metals widely used in SPR sensors are included in the analyses to compare resulting sensor designs'

performances. The feasibility of multi-purpose sensing with the same SPR topology is also investigated via numerical CST simulations using multi-section receptor patches in the sensing dielectric layer to detect the presence of different types of test targets in a given sample solution.

Keywords: Surface Plasmon Waves, Surface Plasmon Resonance Sensor, Optical Sensing, Dielectric Function of Metals, Plasmonics.

ÖZ

YÜZEY PLAZMON REZONANS SENSÖRLERİN TEORİSİ VE UYGULAMALARI

Özdemircan, Furkan
Yüksek Lisans, Elektrik ve Elektronik Mühendisliği
Tez Yöneticisi: Prof. Dr. Gönül (Turhan) Sayan

Şubat 2021, 142 sayfa

Bu tezde, yüzey plazmon rezonans (YPR) olayı ve optik algılama uygulamaları incelenmiştir. YPR sensörler, biri metal biri yalıtkan olmak üzere, gerçek kısmı birbiriyle zıt işaretli elektriksel geçirgenlik değerine sahip iki malzeme arasındaki ortak yüzeyde, yüzey plazmon dalgalarının (YPD) uyarılması ile çalışırlar. YPRnin varlığı, açt taraması ya da dalga boyu taraması ile edilen yansıma profili eğrisinde, en küçük değere doğru kesin bir düşük şeklinde kendisini gösterir. En küçük YPR yansıma değerinin konumu, malzeme katmanlarının elektriksel geçirgenlik ve kalınlık değerlerine karşı oldukça hassastır. Bu parametrelerden birinde meydana gelen en küçük bir değışiklik bile YPR yansıma eğrisinde en küçük değerin konum değışikliğine göre, yüksek bir doğruluk ile ölçülebilir. YPD uyarılmasında prizma temelli eşleme yöntemi kullanılarak prizma, ince metal film ve yalıtkan katmandan oluşan üç katmanlı YPR sensör yapıları, analitik çözümler ve sayısal benzetimler kullanılarak incelendi. YPR sensör yapılarında sıklıkla kullanılan metallerin elektriksel geçirgenlik fonksiyonu modelleri, bu metallerin sensör tasarımlarındaki performanslarını karşılaştırma amacıyla incelendi. Aynı YPR yapısı ve çok sektörlü algılama yüzeyleri kullanılarak, çoklu-kullanım özelliğine sahip ve belli bir test

özeltisinde yer alan birden fazla malzemeyi test edebilen sensörlerin uygulama olanakları CST simülasyonları aracılığıyla incelendi

Anahtar Kelimeler: Yüzey Plazmon Dalgaları, Yüzey Plazmon Rezonans Sensör, Optik Algılama, Metallerin Dielektrik Fonksiyonları, Plazmonik.

To The Little Black Fish, and The Star Thrower...

ACKNOWLEDGMENTS

First and foremost, I would like to express my gratitude to my advisor Prof. Dr. Gönül Turhan Sayan, for her endless patience, support, and guidance; not only for my thesis studies, also for my whole carrier and life decisions during the most challenging days of my master's studies. I am fortunate to have her as a supervisor and a mentor. I am glad that I had a chance to meet and study with her.

I would also like to thank Prof. Dr. Mustafa Kuzuoğlu, Prof. Dr. Kemal Leblebicioğlu, Assoc. Prof. Dr. Serdar Kocaman, Prof. Dr. Metin Sabuncu for their participation in my thesis committee, valuable suggestions and comments regarding my thesis, and for their valuable ideas on future research on SPR sensors.

I want to thank Dr. Sultan Can for her support in CST Studio Suite simulations; Dr. Deniz Karaçor and Salih Ünsal for their help in proof-reading and moral support during my studies; Gökтуğ Işıklar for arranging and formatting of the thesis and his moral companionship throughout my 3,5 years in METU; and Kaan Arda, Mert Belörenoğlu, Gökhan Öztürk, Burçin Topuz and Fatma Gül Altun for their moral support and friendship; Prof. Dr. Yeşim Zoral and once again, Prof. Dr. Metin Sabuncu for inspiring me to study electromagnetics and pursue a career to be a scientist, and showing me the right path, which made all of this possible.

Finally, I would like to thank my sister Tuğçe Özdemircan for her initial idea about working on biosensors due to the requirements in Turkey, and my parents Leyla Kıdış and Yüksel Özdemircan for everything they have done for me.

TABLE OF CONTENTS

ABSTRACT.....	v
ÖZ.....	vii
ACKNOWLEDGMENTS	x
TABLE OF CONTENTS.....	xi
LIST OF TABLES	xiv
LIST OF FIGURES	xv
LIST OF ABBREVIATIONS.....	xix
LIST OF SYMBOLS	xx
CHAPTERS	
1 INTRODUCTION	1
1.1 Optical Sensing	2
1.2 Plasmonics and Surface Plasmons	2
1.3 Surface Plasmon Resonance and Sensing	4
1.3.1 Physical Structure and Basic Components of SPR Sensors.....	6
1.3.2 Theoretical Aspects, Modeling Materials and Post Processing of SPR Sensors	8
1.3.3 SPR Sensing Procedure.....	9
1.3.4 Future of SPR Sensors	11
1.4 Organization of the Thesis	12
2 ELECTROMAGNETIC THEORY OF SURFACE PLASMONS.....	15

2.1	Derivations of Reflection Coefficient for a Planar Multilayer Structure..	16
2.1.1	The Reflectivity of a Three-Layer System	27
2.1.2	The Reflectivity of N-layer Systems	33
2.2	Dispersion Relation of Surface Plasmons.....	36
2.2.1	Coupling of Surface Plasmons	40
2.2.2	Penetration Depth of Surface Plasmons	44
2.3	The Requirement of P-Polarization in SPR Sensor Operation	45
2.4	The Requirement of Wavevector Increment.....	47
2.5	The Sensitivity of SPR Sensors	48
3	MATERIAL MODELING FOR SPR ANALYSIS	51
3.1	Outline of Material Modeling for SPR Simulations	51
3.2	Lorentz-Drude Model for Permittivity of Metals	52
3.2.1	Complex Permittivity and Refractive Index Functions of Selected Metals	57
3.2.2	Concluding Remarks: Metal Selection for SPR Sensors.....	62
3.3	Modeling of Coupling Prisms.....	63
3.4	Modeling of the Test Material	67
3.4.1	Empirical Model for Water Permittivity	68
3.4.2	Biological Test Material Modeling	71
4	EFFECTS OF METAL SELECTION ON SENSOR PERFORMANCE	77
4.1	Analysis Method	78
4.1.1	Materials and Dimensions of Structure	79
4.1.2	Properties and Parameters of CST Studio Suite Simulations	79
4.2	Results.....	82

4.3	Conclusions on Metal Selection	88
5	MULTI-SECTIONAL SPR SENSOR DESIGN	93
5.1	Two-Sectional SPR Sensor Design: Basic Approach	94
5.2	Case 1: SPR Sensor to Detect BSA Protein	96
5.3	Case 2: SPR Sensor to Detect Protein G	98
5.4	SPR Sensor with Striped (Double-patch) Sensing Film Design	100
5.4.1	Two-sectional Sensing Film with Two Lossless Target Molecules	101
5.4.2	Two-sectional Sensing Film with One Lossless / One Lossy Target Molecules	106
6	CONCLUSION.....	115
6.1	Future Work	116
	REFERENCES	119
	APPENDIX	
A.	SUM OF GEOMETRIC SERIES	141

LIST OF TABLES

TABLES

Table 3.1: Lorentz-Drude Parameters of Selected Metals.....	57
Table 5.1: Resonant wavelength positions and shifts (in nm), for BSA/Protein G bonding, at 68° and 76° incidence angles.....	104
Table 5.2: Resonant wavelength positions and shift amounts for BSA/Lossy molecule bonding	110
Table 5.3 Minimum Value of Resonant Dip and Shifts from the Empty Case	111

LIST OF FIGURES

FIGURES

Figure 1.1: Various types of gold-coated Biacore SPR sensor chips [27].	5
Figure 1.2: Standard SPR Measurement Block Diagram.	7
Figure 2.1: Reflection/Refraction problem in a 2-media system. Both media are infinite in the z-direction, making the system semi-infinite and 2-dimensional.	18
Figure 2.2: 3-layer / 2-boundary reflection problem, the thin film in the middle has a finite thickness of d , and medium 3 assumed to be infinite.	29
Figure 2.3: Geometry for N-layer reflectivity problem. The wave is sent from medium 1, with no reflections within medium N (thickness of the first and last medium are assumed to be infinite).	34
Figure 2.4: The equation gives a theoretical limit for the resolution of an SPR sensor as reported in [106]. The results indicated by small circles are reported in a) [138], b) [139] c) [56], d) [140], e) [137], f) Biacore 3000 (GE Healthcare, USA), g) [92], h) [141], i)[142]. Figure is taken from the original article.	49
Figure 3.1: a) Complex permittivity, and b) complex refractive index of gold.	60
Figure 3.2: a) Complex permittivity, and b) complex refractive index of silver.	60
Figure 3.3: a) Complex permittivity, and b) complex refractive index of aluminium.	61
Figure 3.4: a) Complex permittivity, and b) complex refractive index of copper.	61
Figure 3.5: Simulated reflectance curves for an SPR sensor with lossless and lossy silver layers. The structure consists of BK7 type prism glass, silver, BAF10, and pure water ($n=1.33$, lossless) operated at 632nm. Lossless silver does not generate any resonance, while a well-developed SPR curve is observed for lossy silver.	62
Figure 3.6: Complex Refractive Index of BK7, low values of k , and small variation of n can be observed.	65
Figure 3.7: Refractive Index and Extinction Coefficient of BAF10 Optical Glass.	66

Figure 3.8: Real part of the refractive index of sapphire. The extinction coefficient for sapphire is negligibly small, assumed zero.....	66
Figure 3.9: Refractive index of water calculated by Equation 3.8 at a fixed temperature of $T = 25^{\circ}\text{C}$, over the ranges $0\text{‰} < S < 35\text{‰}$, and $400\text{nm} < \lambda < 700\text{nm}$	69
Figure 3.10: Refractive index of water calculated by Equation 3.8 at a fixed salinity level of $S = 25\text{‰}$ over the ranges $0^{\circ}\text{C} < T < 30^{\circ}\text{C}$, and $400\text{nm} < \lambda < 700\text{nm}$	70
Figure 3.11: Refractive index of water calculated by Equation 3.8 at a fixed wavelength of $\lambda = 500\text{nm}$ over the ranges $0^{\circ}\text{C} < T < 30^{\circ}\text{C}$, and $0\text{‰} < S < 35\text{‰}$...	70
Figure 3.12: Four-layer system produced after binding proteins to the sensing layer.	73
Figure 3.13: Change of refractive index with the antibody concentration of the test solution. The thickness of the protein layer is assumed to be constant at 14 nm for all concentrations. The figure is taken from the original article [167]......	74
Figure 3.14: 5-layer system with a new layer formed below the Prolinker sensing layer.	76
Figure 4.1: Semi-infinite, four-layer SPR sensor topology modeled in CST.....	80
Figure 4.2: The periodic sensor structure simulated by the Unit Cell module of the CST Studio Suite, where each identical cell is described in Figure 4.1. The structure seen from a) the xy-plane, and from b) the xz-plane.....	81
Figure 4.3: Simulation results for Au; a) Analytical simulations results with Matlab, b) Numerical simulation results with CST Studio Suite.	84
Figure 4.4: Simulation results for Ag; a) Analytical simulations results with Matlab, b) Numerical simulation results with CST Studio Suite.	85
Figure 4.5: Simulation results for Cu; a) Analytical simulations results with Matlab, b) Numerical simulation results with CST Studio Suite	86
Figure 4.6: Simulation results for Al; a) Analytical simulations results with Matlab, b) Numerical simulation results with CST Studio Suite	87
Figure 4.7: Resolution (in RIU) of selected metals ($\sigma_{\text{RI,metal}}$) for 600-1000 nm.....	90
Figure 4.8: Skin depth of selected metals for 600-1000 nm range.....	91

Figure 4.9: a) Resolution (RIU) of selected metals, and b) skin depth of selected metals, for 900-1600 nm range.	91
Figure 5.1: Four-layer SPR sensor structure with two-sectional SF, prior to molecular bonding: a) Single Cell topology on the xz -plane, b) Multiple-cells, seen from the xz -plane c) Striped pattern of sensing films, seen from the xy -plane (the SF layer is preceded by the prism and metal layers, and followed by the test substrate).	95
Figure 5.2: Analytical results for Case 1 computed by Matlab programming (refractive index data are provided by [167]) before and after the binding of BSA molecules for the incidence angle of a) 68° b) 76°	97
Figure 5.3. Results of numerical simulations for Case 1 obtained by CST Studio Suite (refractive index data are provided by [167]) before and after the binding of BSA molecules for the incidence angle of a) 68° b) 76°	98
Figure 5.4: Analytical results obtained for Case 2 by Matlab programming (refractive index data are provided by [168]) before and after the binding of protein G molecules for the incidence angle of a) 68° b) 76°	99
Figure 5.5: Results of numerical simulations for Case 2 by CST Studio Suite (refractive index data are provided by [168]) before and after the binding of protein G molecules for the incidence angle of a) 68° b) 76°	100
Figure 5.6: Results of numerical simulations for SPRFs by CST Studio Suite (refractive index data are provided by [167], [168]) for four different combinations of molecular bonding regarding the BSA and G proteins at the incidence angle of a) 68° and b) 76°	102
Figure 5.7: Results of numerical simulations by CST Studio Suite (the zoomed-in version of the plots shown in Figure 5.6).	103
Figure 5.8: Effects of the increasing refractive index on the SPRF curve (computed using the sensor topology given in [167]) for the incidence angle of 68°	105
Figure 5.9: Variation of the SPRF curve (from [167]) in response to the change in the imaginary part of the permittivity of the test medium.	107

Figure 5.10: Results of the numerical simulations for the SPRF by CST Studio Suite for the hypothetical lossy material, prior to and after the molecular bonding for the incidence angle of a) 68° and b) 76°. 108

Figure 5.11: Results of numerical simulations for the SPRF curves by CST Studio Suite, before and after the bonding of BSA and lossy molecule in four different bonding scenarios for the incidence angle of a) 68° and b) 76°. 109

Figure 5.12: The zoomed-in version of Figure 5.11. 110

Figure 5.13: Change of the minimum value of resonance dip versus the change in the imaginary part of the complex permittivity. Curves for only lossy material coupled and both BSA/Lossy coupled in two-material cases are overlapping; it proves the effect on minimum resonant dip value comes only from lossy material. 112

Figure 5.14: Change in resonance minimum value with varying thickness values and for 68° and 76° incidence angle cases where $\epsilon''=0.3$ is kept constant. 113

LIST OF ABBREVIATIONS

ABBREVIATIONS

SP: Surface Plasmon

SPW: Surface Plasmon Wave

SPR: Surface Plasmon Resonance

TIR: Total Internal Reflection

ATR: Attenuated Total Reflection

KR: Kretschmann-Raether Configuration

POI: Plane of Incidence

UPW: Uniform Plane Wave

BSA: Bovine Serum Albumin

PBS: Phosphate Buffered Saline

RIU: Refractive Index Unit

SPRF: Surface Plasmon Reflectance Spectrum

UC: Unit Cell

SF: Sensing Film

FWHM: Full Width at Half Maximum

LIST OF SYMBOLS

SYMBOLS

ϵ_0 : Free Space Permittivity

$\epsilon = \epsilon_r \epsilon_0$: Complex Permittivity

$\epsilon_r = \epsilon' + j\epsilon''$: Complex Relative Permittivity

μ_0 : Free Space Permeability

μ : Permeability

k_0 : Free Space Wavenumber

$n = n' + jn''$: Complex Refractive Index

c : Speed of Light in Vacuum

η : Intrinsic Impedance

χ_e : Electric Susceptibility

ω : Angular Frequency

ω_p : Angular Plasma Frequency

CHAPTER 1

INTRODUCTION

Accurate sensing is necessary for scientific and industrial applications in the modern era of advanced technologies. The design of high-precision, low-cost, and miniaturized optical sensors, in particular, made the widespread use of sensing systems possible in almost every aspect of our daily lives. Temperature sensors, smoke detectors, motion sensors, and air quality monitors are some common examples used to improve safety measures and quality of life. Various sensing systems are also used to ensure food safety by detecting harmful pathogens. Water quality measurements require high precision sensing to detect the molecular amounts of poisonous substances in tap water; medical centers use various sensing systems to analyze patients' health status; many sensors are used in all kinds of process control systems in factories and different vehicle types. These are well-known examples, among many.

Optical sensors are widely preferred in the sensing applications mentioned above. Due to the nature of light, optical sensors are fast, light-weight, small in size, highly precise, and they can also be designed as non-destructive sensors for many applications. Surface Plasmon Resonance (SPR) sensors are very popular among the optical sensors as they can perform molecular-level, high accuracy, label-free measurements in real-time. Reusability, reliability, and mass production, and hence the lower cost, are other properties that make SPR sensors a feasible choice for many applications.

The aim of this thesis is to study the surface plasmon resonance (SPR) phenomenon with its theoretical background with physical and mathematical modeling; to learn the basic analytical methods for analysis and design of SPR sensing, and to investigate the feasibility of designing multi-analyte type SPR sensors using CST based numerical simulations.

1.1 Optical Sensing

An optical sensor can be defined as a device that encodes the data of measurand into the properties of light. Optical sensing is a rapidly developing field of natural sciences and closely related to different engineering branches, primarily electrical and electronics engineering [1]–[3]. Optical sensors generally operate within or around the visible range. Ranging from the optical point sensors that sense the measurand(s) of concern at a specific location in space to distributed fiber optical sensors that can monitor a measurand almost continuously over the length of a specially designed sensor fiber, optical sensors designed by many different methods and manufactured by different technologies are widely used in a vast number of applications.

1.2 Plasmonics and Surface Plasmons

Plasmonics is a sub-field of optics studying plasmons' nature and applications. Plasmons are quasiparticles or quantum of collective charge density oscillations in the free electron gas, which was first suggested by Pines and Bohm in 1952 [4]. When the light interacts with matter and transfers its energy to electrons, delocalized electrons collectively oscillate as a response to the oscillating electric field, and their quantum is called plasmons. In other words, plasmons are generated by the coupling of photons to electron plasma.

Since their discovery, the theory and applications of plasmons have been developed rapidly. The concept of plasmonics is widely used in many areas of optics and photonics, including subwavelength applications, sensing, waveguiding, light enhancement, breaking the diffraction limit, among many others, in nanoscale [1], [5]–[12].

Plasmons can exist in different forms, such as bulk plasmons, surface plasmons (SPs), localized plasmons. Surface plasmons are widely used in sensing applications and provide a basis for SPR sensors.

Surface plasmons (SPs) can be excited at planar dielectric/metal interfaces; this can be interpreted by considering the requirement of delocalized electrons, which exists in solid metals. Metallic structures contain an alignment of positive ions covered by a cloud of the free electron gas. Oscillation of these electron charges in metals creates an electromagnetic surface wave that penetrates through metal and dielectric and propagates parallel to the surface while decaying exponentially in the direction normal to the boundary (i.e., interface between metal and dielectric). Typically, penetration depth in the metal and the dielectric is 20 to 30 nm and 200 to 400 nm, respectively, and the propagation length of SPs is up to a few micrometers [13].

Surface plasmons were first discovered by Robert W. Wood; he observed anomalous diffraction of light when he shone the light on a metallic diffraction grating [14], [15]. Wood stated that he observed sharp, dark lines in the spectrum when the light shone on the grating surface under certain conditions. He reported that the intensity ratio of bright to dark lines is more than 10 to 1. Wood's discovery was first examined theoretically by Rayleigh and Fano, separately [16], [17]. Though Pines and Bohm [4], [18], Watanabe [19], and Leder [20] contributed to the field in the following years, the rise of the Surface Plasmons came after the discovery of the attenuated total reflection (ATR) method, suggested by Otto, and Kretschmann and Raether independently [21], [22].

1.3 Surface Plasmon Resonance and Sensing

The incident photon's momentum and frequency must match the SP momentum and frequency to excite the SPs. In case this condition is not satisfied, SPs will not be excited, as coupling will be very weak, resulting in a total internal reflection (TIR). Full coupling of surface photons and SPs with matching frequency and momentum creates a resonance, and this phenomenon is called Surface Plasmon Resonance (SPR). The resonance condition and the properties of SP waves are extremely dependent on the properties of the materials forming the boundary (i.e., dielectric and metal), that present in the form of thin layers and usually forming the boundary. Any change in the layer properties, such as an increase in layer thicknesses and/or a change in the effective refractive index due to binding of molecules in SP based biosensors, for instance, the resonance condition is vastly affected, making the SP approach a highly preferred choice for sensing applications.

The first implementation of the SPR phenomenon in a sensing apparatus was provided by Nylander, and Liedberg, in the 1980s [23]–[25]. During their first experiments, Nylander and Liedberg placed human IgG on a silver film to detect antibodies. In the mid-80s, instrumentation of SPR sensors in immunochemical interactions was completed and presented in the literature. However, the commercialization of SPR sensors happened in the '90s. In 1990, Swedish biosensing company Pharmacia AB released the first commercial SPR biosensor in the market, Biacore. Many other companies followed Biacore in implementing SPR as a biosensing apparatus. Due to these achievements, the number of published articles on SPR increased rapidly from the early to late '90s. While the SPR sensors can detect the presence of a large variety of matters, the most popular applications have been demonstrated for sensing bio-molecular interactions [26]–[31].

Demonstration of the use of SP phenomenon in optical sensing is done by shining a lightwave onto the metallic surface of the SPR sensor before and after the test

specimen is introduced and comparing the properties of the reflected wave under the reference and the test conditions, respectively. The light properties to be monitored for sensing may be frequency, reflection angle, intensity, or phase of the reflected light. As the SPR reflectance curve has a sharp minimum (or absorption curve has a maximum), in most applications, observation of the minimum reflection (the darkest case observable for the reflected light) condition reveals that the SPs are excited. If the properties (thickness and/or refractive index) of the material layers in the sensor change by the presence of a measurand, the position of the dark line (i.e., the SPR reflectance minimum) will shift.



Figure 1.1: Various types of gold-coated Biacore SPR sensor chips [27].

The direct coupling of light and surface plasmons is not possible since the momentum of free space photons is always lower than the momentum of surface plasmons. Matching the momentum of the photons to the SPs is done either by using a prism, an ATR scheme [21], [22], [32], or introducing irregularities in the metal surface such as gratings [33], [34]. While a prism employs its high refractive index for matching, gratings are used to increase the parallel component of the incident wave vector where gratings shift the magnitude of the propagation vector by order of diffraction periods. LEDs and lasers can be used as light sources. Though, in

general, laser sources are highly preferred due to their very narrow spectral band [35]–[37]. An SPR chip manufactured by Biacore is shown in Figure 1.1.

Presently, SPR biosensors are widely used in biosensing and chemical sensing due to their fast and accurate measurement capacities with no labeling requirements. Various SPR sensors have been designed so far to provide molecular-level measurement results. Also, they can be manufactured as reusable sensors employing suitable washing methods.

1.3.1 Physical Structure and Basic Components of SPR Sensors

An SPR sensing apparatus consists of a sensor chip, a light source, and a light detector. SPR sensor chip is a planar, multilayered structure created with thin layers of dielectrics and a metal; an example of an SPR sensor chip has shown in Figure 1.1. The primary purpose of sensor operation is to measure and calibrate the shift in the resonance minimum position under the presence of a test sample. The other parameters of the surface plasmon resonance curve, such as the intensity at the minimum reflection and the full width at half maximum of the SPR curve, also depend on the material parameters of the multilayered sensor structure.

SPR sensor measurements are performed by scanning a specific range of (incidence/reflection) angle or a band of wavelengths. The light source used in the apparatus is selected according to the preferred interrogation method. In the wavelength interrogation approach, the light source must scan a required band of wavelengths. The use of either LEDs or lasers is reported in the literature of SPR sensors in this case. For measurements in the visible light region, a LED can be used as the light source, although the measurements are generally performed in a narrower part of its operation bandwidth [38]. For the angular interrogation approach, on the other hand, a mechanical rotation system is needed both in the source and detector ends. A laser-type source is preferred in the angular scanning method for higher

sensitivity that requires a narrow bandwidth of wavelengths and a small beamwidth. Since angular measurements are ideally performed at a single frequency, variations in the electrical parameters of design materials with frequency are negligible. Thus, the reconstruction of measured data from the sensors' measurements is easier for angular interrogation, in general. It should be noted that the incident light is generally passed through a polarization filter first since plasmons can be excited by p-polarized light only.

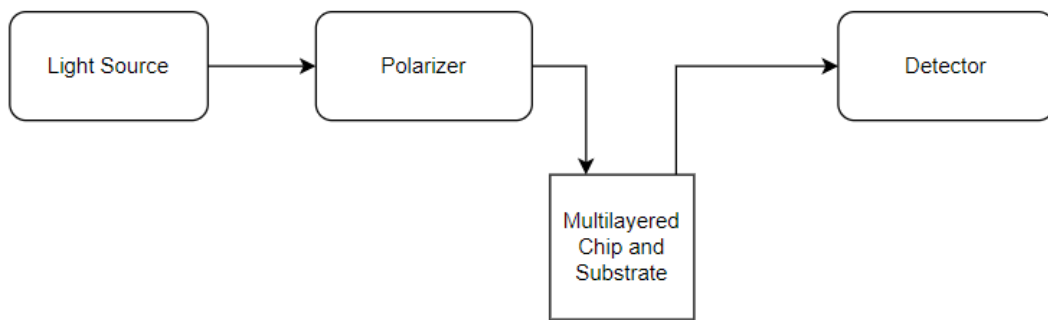


Figure 1.2: Standard SPR Measurement Block Diagram.

Requirements for the detector choice are similar to those of the source. The detector should precisely detect the minimum of the SPR curve over a given wavelength spectrum or the range of reflection angle for the chosen interrogation approach.

The challenging part of the SPR sensor design is to improve the multilayered topology design, in general. The multilayered system is fabricated as a chip with a thin, multilayered structure containing a metallic film. The design normally reflects light but displays a sharp absorption peak upon the excitation of surface plasmon waves (SPW) at the interface of the metal film and the dielectric sensing layer. Previously mentioned light coupling systems are designed within the sensor chip too. As plasmons occur in metals, the main element of the sensor chip is the metal layer, whose thickness varies from 50 to 100 nm, in general. Low-loss metals are preferred in the sensor design to enhance the extent of the SPR sensor along the propagation direction (that is parallel to the metal/dielectric interface). For efficient operation,

the sensor must have only a single absorption peak caused by the excitation of plasmons on the metal/dielectric surface. Prism couplers are placed directly over the metal, using special liquids or by evaporating the metal layer on the base of the prism. On the other hand, the grating couplers are directly carved on the metal layer.

The simplest form of the sensor chip consists of only a coupler, metal, and a dielectric bulk medium (where measurement happens). However, additional layers of dielectric materials may be used in the SPR design to attract specific molecules to the sensor surface; or increase sensor sensitivity by sharpening the resonance dip or providing larger shifts in SPR minimum. Dielectric layers are generally placed under metal or rarely between metal and coupler. In applications like biological sensing, an additional layer is usually required to attract specific molecules in the specimen, as in the antibody/antigen binding.

1.3.2 Theoretical Aspects, Modeling Materials and Post Processing of SPR Sensors

Computation of the reflectance spectrum of an SPR sensor is the primary design task where the sensor topology is modeled as a planar multilayered structure [26], [39]–[42]. Then, using Maxwell's equations and applying the boundary conditions at each interface, the SPR curve of the sensor is calculated, provided that the requirements for the excitation of SPW are met. While prism-coupled sensors can be analyzed directly with this multilayer modeling approach, some extra steps are needed to obtain the reflectance curve of the grating coupled sensors [43], [44]. SPR sensor analysis for the angular interrogation and the wavelength interrogation approaches are essentially the same; though, calculating SPR curves for wavelength interrogation sensors requires the frequency-dependent modeling of the relative permittivity function.

The relative permittivity function (i.e., the dielectric function) of the metal component used in the SPR sensors needs to be represented by the Lorentz-Drude model in general [45], [46]. This modeling task is critical for accurate simulation and design work as SPs are highly sensitive to metal properties [1], [47]. Multiple oscillators in the Lorentz-Drude model can be neglected since SPR sensors generally operate at visible and near-IR regions, well below the plasma frequency. A few different types of metals satisfy the SPR coupling condition in these ranges, such as gold and silver, which are the most popular metals used in SPR sensors [1], [47].

Prisms used to couple incoming light to SP modes generally have large refractive index values (in the real part) with very low material dispersion [48], [49]. Therefore, they can be assumed nondispersive for narrow-range scanning applications. Grating couplers are generally built from the same metal already used in the sensor. So, the same metal modeling can be used for the grating couplers [12], [37], [50]–[57].

Modeling the dielectric substrate layer of an SPR sensor may be relatively more complicated. Based on the application's aim, the substrate may be in different states (solid, liquid, or gas) and various thicknesses (a bulk region or a very thin layer with a thickness of molecular size). Water is often used as a liquid substrate containing ions, molecules, or various pathogens in biological or chemical sensing applications. For this purpose, modeling the dielectric function of water is critical in SPR sensor design [58]–[63]. Researchers have also kept searching for different and better materials for SPR sensing applications to improve SPR sensor performances [64], [65].

1.3.3 SPR Sensing Procedure

The measurement procedure with SPR sensors depends on the application. Many applications, particularly in biosensing, require sample preparation to begin with [38]. SPR sensors can detect any effect that can change the refractive index or the

thickness of sensor layers [66]–[73]. Taking reference measurements with an SPR sensor without any measurement sample is essential for calibration purposes to eliminate the shifts in the SPR curve's minimum caused by unrelated factors to the target of concern. In SPR biosensing, real-time measurements are also desired, such as protein interaction applications and food safety measurements [74]–[79]. Light-wave can be shone into the sensor surface for a specific time to observe the course of interactions for these applications.

Various parameters of light can be monitored in SPR sensors:

- **Angular Interrogation:** Incident light (at a selected wavelength) is sent to the sensor surface while changing the incidence angle (hence the angle of reflectance). The minimum of the SPR curve (almost no-reflection case) occurs at a certain reflection angle, implying the excitation of SPW at the metal/dielectric interface [55], [66], [80]–[82].
- **Wavelength Interrogation:** Incident light (at a selected incidence angle) is sent to the sensor surface while changing the wavelength over a suitable bandwidth. The minimum of the SPR curve occurs at a particular wavelength implying the excitation of SPW at the metal/dielectric interface [83]–[87].
- **Intensity Sensors:** Change in the reflected (in some cases, transmitted) light intensity is monitored at a particular "wavelength and angle" pair to detect the excitation of SPW [24], [25], [88].
- **Phase Shift Sensor:** Phase shift change in the reflected wave is monitored to detect the excitation of SPW [89]–[94]

Among the approaches listed above, angular and wavelength interrogation methods are the most popular ones reported in the literature due to their robustness and ease of application. Sensors can also be operated in a multichannel form by combining these two methods to scan both reflection angle and wavelength to detect SPR minimum [95]–[98].

SPR Sensors can theoretically operate in most of the realistic conditions for biological and chemical measurements. However, as the SPR decodes properties of its target to the refractive index, any factors affecting the refractive index would seriously influence the measurement performance or can be used to create a new sensor. SPR sensors can be used to measure temperature [66], [99]; humidity [100], [101]; or various other sensors with such corrections [102]–[105]. Accurate measurements can still be achieved without any correction if test measurements are available or the ambient conditions do not radically affect the refractive index of the layers of the sensor chip or the substrate. Since one of the most important tasks of SPR sensors is biosensing, ambient conditions can be assumed as "not extreme" during its operation as a biosensor.

The main limitation of SPR sensor measurement is the inability to measure more than one target in complex substrates simultaneously. SPR sensors can very effectively measure many molecules; however, they can only measure one type of molecule simultaneously. Sensing multiple target molecules simultaneously is not very effectively implemented yet.

1.3.4 Future of SPR Sensors

Currently, SPR sensors are sensitive enough to provide even molecular level detections. As some researchers state, SPR sensors have almost reached their theoretical limits for detection sensitivity and accuracy, fulfilling their potential completely [64], [106]. However, recent studies have focused on designing low-cost and multi-purpose SPR based measurement systems. Further improvements in sensor performance can be achieved by optimizing the sensor topology and material choices in application-specific design problems.

A breakthrough in SPR research may occur if more effective sensors are designed to detect multiple targets in complex substrates simultaneously, such as detecting more than one antigens present in a blood sample. Currently, SPR sensors can measure only one type of molecule found in such liquid substrates. There have been only a few attempts in the literature to measure multiple analytes simultaneously [107]–[109]. An SPR sensor can accurately measure the number of glucose molecules in a blood sample; however, it cannot detect (or fail in separating data of) another molecule. Achievement in multi-analyte sensing would be revolutionary for the healthcare industry since SPR sensors can provide high-speed and highly accurate measurements with relatively low maintenance and personnel cost. One of this thesis's purposes is to investigate the feasibility of designing SPR sensors with multi-analyte sensing capacity.

Finally, a well-designed standard SPR apparatus in a mobile station form would help underdeveloped countries with food safety and healthcare applications. Crucial sensing for measuring tap water quality, food safety, and medical diagnostic purposes can be accomplished by a portable and reusable SPR based sensor rapidly and accurately would be very valuable when well-equipped laboratories are out of reach [36], [110]–[113].

1.4 Organization of the Thesis

The thesis is organized into six chapters, as follows:

The aim of the thesis is given in the Introduction Chapter, together with the definition and basics of SPR sensing, its possible applications, and the associated literature review.

Electromagnetic analysis of planar multilayer topologies is given in Chapter 2 to compute the Surface Plasmon Reflectance curve that provides the basic tool in SPR

sensing. The occurrence of the reflectance minimum refers to the excitation of SPW in the structure. The sensitivity of the minimum location to refractive indices and the thicknesses of sensor layers provides an accurate sensing mechanism.

Theoretical calculations and simulations require accurate modeling of materials used in the sensor design. The dielectric function modeling is critical for the dielectric prism, the dielectric substrate, and especially for the metal layer. These issues are addressed in Chapter 3.

The effects of using different types of metals in SPR sensor performance are investigated in Chapter 4 by analytical solutions with Matlab [114] and numerical CST simulations [115].

A feasibility study for a Double-Analyte SPR Sensor design is presented in Chapter 5. The dielectric substrate is slightly modified to have two different binding patches to detect the presence of two different molecules in the testing specimen, if possible.

Finally, the thesis is concluded with a summary of basic achievements and the important results in Chapter 6, the Conclusions Chapter.

CHAPTER 2

ELECTROMAGNETIC THEORY OF SURFACE PLASMONS

In this Chapter, electromagnetic analysis of a planar multilayer sensor topology is presented to compute the Surface Plasmon Reflectance curve of the SPR sensor. The occurrence of the reflectance minimum of this curve indicates that SPWs are excited at the boundary of the metal layer and the sensing dielectric layer. The position of the SPR minimum is highly sensitive to even very small changes in the refractive indices and the thicknesses of the sensor layers providing an accurate sensing mechanism.

Surface plasmons can be excited with only p-polarized waves. The incident electric field intensity vector lies in the plane of incidence and has a normal component regarding the planar boundaries. Hence, excitation of the bound charges in the multilayer system is possible. On the other hand, for an s-polarized wave, the incident electric field component will be perpendicular to the plane of incidence, being parallel to the material boundaries. Therefore, it cannot excite surface waves. Since the only relevant excitation for SPR systems is p-polarized excitation, derivations of the reflectivity will be given only for the p-polarized case. As the light coupling mechanism, a common approach of using a dielectric prism will be adopted due to its simplicity and ease of application. More details on alternative coupling methods will be given in later chapters.

2.1 Derivations of Reflection Coefficient for a Planar Multilayer Structure

The structure of a typical 3-layer or a more advanced 4-layer SPR sensor can be analyzed using a planar multilayer structure composed of different materials, which will be assumed to be linear, homogeneous, isotropic, and source-free media [39], [116]–[120]. Additionally, in the optical frequency range, all the materials used in SPR design can be assumed nonmagnetic with $\mu = \mu_0$ where $\mu_0 = 4\pi 10^{-7} \text{ (H/m)}$ is the free space permeability. The prism layer is needed to couple input the light waves into SP waves. This layer is assumed to be a lossless and nondispersive medium with a high value of real relative permittivity. The dielectric substrate layer (or the sensing layer as it is usually called) and the metal layer, in particular, need to be modeled as lossy media with complex permittivity values. Assuming that the top layer (the prism layer) of the sensor is illuminated by a uniform plane wave (UPW), which is a TEM wave, the total reflected field. Hence, the reflection coefficient can be computed by applying Maxwell's Equations, constitutive relations, and the boundary conditions, in general.

Starting with the fundamental problem of two media separated from each other by a planar boundary, the solution for the Fresnel Formulas for reflection and transmission coefficients can be obtained easily in the parallel polarization (p-polarization) case. The derivation steps are summarized below using the problem geometry shown in Figure 2.1 as a reference. The plane of incidence (POI) is selected to be the x-y plane in this problem, where the planar boundary between medium 1 and medium 2 is placed at $x = 0$.

As shown in this Figure 2.1, a p-polarized incident UPW with the propagation vector $\vec{k}_{1,i}$ hits the boundary at the incidence angle θ_i , which is the angle made between the direction of the propagation vector and the normal direction to the interface. The reflected and transmitted UPWs with p-polarization are created in the process whose

propagation vectors $\vec{k}_{1,r}$ and $\vec{k}_{2,t}$ both lie on the POI, making the reflection angle θ_r and the transmission angle θ_t with the interface normal.

In general, the \vec{E} and \vec{H} field phasor vectors of a UPW are related to each other as

$$\vec{H} = \frac{1}{\eta} \hat{u} \times \vec{E} \quad (2.1)$$

where \hat{u} is the unit vector in the direction of propagation vector, and η is intrinsic impedance defined as

$$\eta = \sqrt{\frac{\mu_0}{\epsilon}} \quad (2.2)$$

In optical range, materials can be assumed nonmagnetic, as previously mentioned, with $\mu = \mu_0$. Also, in the general case of lossy media, ϵ is a complex-valued permittivity defined as

$$\epsilon = \epsilon_r \epsilon_0 \quad (2.3)$$

where $\epsilon_0 = 8.854 * 10^{-12}$ (F/m) is the vacuum permittivity and ϵ_r is the complex relative permittivity that can be expressed as

$$\epsilon_r = \epsilon' + j\epsilon'' \quad (2.4)$$

The refractive index of any material can be defined as

$$n = \frac{c}{v_p} \quad (2.5)$$

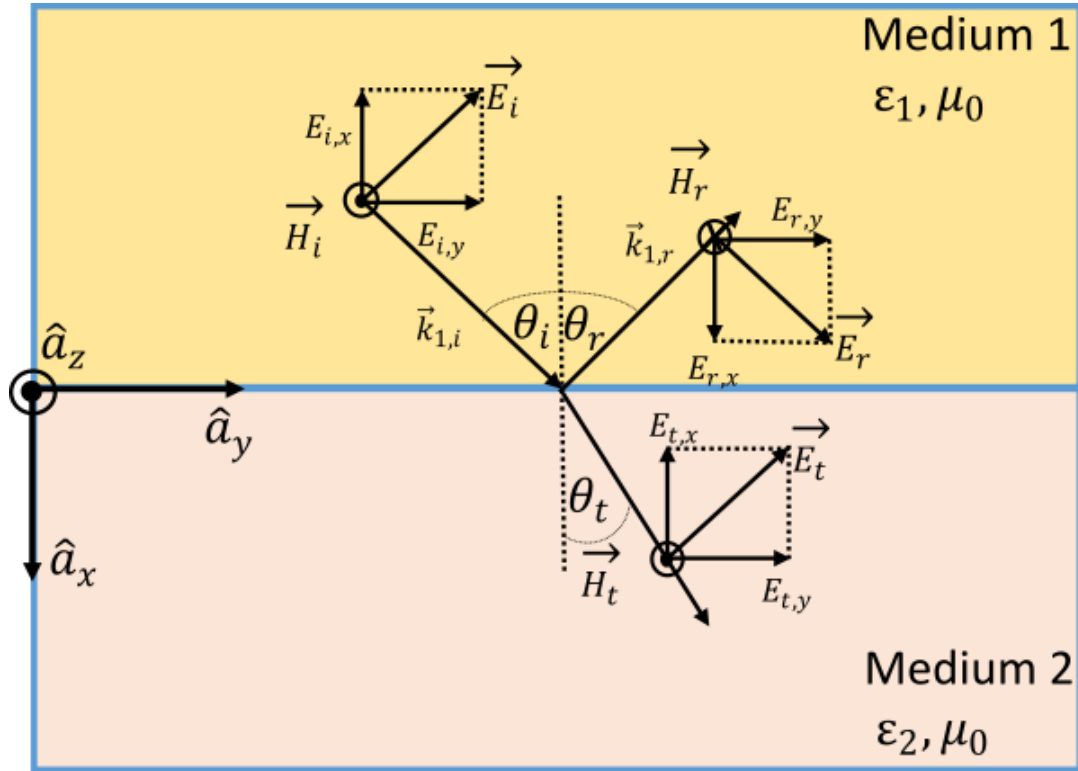


Figure 2.1: Reflection/Refraction problem in a 2-media system. Both media are infinite in the z -direction, making the system semi-infinite and 2-dimensional.

where c is the speed of light in the vacuum, and v_p is the phase velocity in the given medium. For a lossless or low-loss medium, the phase velocity can be written as

$$v_p = \frac{1}{\sqrt{\mu\epsilon}} \quad (2.6)$$

Then, using Equations 2.6 and 2.7 and noting that $\mu=\mu_0$ for the optical range, we can obtain

$$n = \sqrt{\epsilon_r} \quad (2.7)$$

Assuming $e^{j\omega t}$ time convention, for p-polarized (or TM polarized; E-field components is on the POI) case, the electric field intensity and magnetic field

intensity phasor vectors for the incident, reflected and transmitted UPWs of the two-layer media problem can be formulated as given below:

$$\vec{E}_i(x, y) = E_{0i}(-\hat{a}_x \sin\theta_i + \hat{a}_y \cos\theta_i) e^{-jk_1(x \cos\theta_i + y \sin\theta_i)} \quad (2.8a)$$

$$\vec{H}_i(x, y) = \frac{E_{0i}}{\eta_1} (\hat{a}_z) e^{-jk_1(x \cos\theta_i + y \sin\theta_i)} \quad (2.8b)$$

$$\vec{E}_r(x, y) = E_{0r}(\hat{a}_x \sin\theta_r + \hat{a}_y \cos\theta_r) e^{-jk_1(-x \cos\theta_r + y \sin\theta_r)} \quad (2.8c)$$

$$\vec{H}_r(x, y) = \frac{E_{0r}}{\eta_1} (-\hat{a}_z) e^{-jk_1(-x \cos\theta_r + y \sin\theta_r)} \quad (2.8d)$$

$$\vec{E}_t(x, y) = E_{0t}(-\hat{a}_x \sin\theta_t + \hat{a}_y \cos\theta_t) e^{-jk_2(x \cos\theta_t + y \sin\theta_t)} \quad (2.8e)$$

$$\vec{H}_t(x, y) = \frac{E_{0t}}{\eta_2} (\hat{a}_z) e^{-jk_2(x \cos\theta_t + y \sin\theta_t)} \quad (2.8f)$$

where E_{0i} , E_{0r} and E_{0t} are the amplitudes of the incident, reflected, and transmitted electric fields, respectively. At a given frequency $\omega = 2\pi f$, the wavenumbers are k_1 and k_2 while the intrinsic impedances are η_1 and η_2 in medium 1 and medium 2, respectively.

One of the two boundary conditions to be satisfied in time-varying electromagnetics requires that the tangential component of the total electric field is always continuous across the boundary

$$E_{1,tan}(x = 0) = E_{2,tan}(x = 0) \quad (2.9)$$

where $E_{1,tan}$ and $E_{2,tan}$ are tangential components of the total electric field in medium 1 and medium 2. Equation 2.9 can be written in a more explicit form

$$E_{i,tan}(x = 0) + E_{r,tan}(x = 0) = E_{t,tan}(x = 0) \quad (2.10)$$

The y-components are the tangential components of the total electric field vectors with respect to the boundary at $x = 0$ as given below

$$\vec{E}_{i,tangential}(x, y) = E_{0i}(\hat{a}_y \cos \theta_i) e^{-jk_1(x \cos \theta_i + y \sin \theta_i)} \quad (2.11a)$$

$$\vec{E}_{r,tangential}(x, y) = E_{0r}(\hat{a}_y \cos \theta_r) e^{-jk_1(-x \cos \theta_r + y \sin \theta_r)} \quad (2.11b)$$

$$\vec{E}_{t,tangential}(x, y) = E_{0t}(\hat{a}_y \cos \theta_t) e^{-jk_2(x \cos \theta_t + y \sin \theta_t)} \quad (2.11c)$$

Therefore, evaluating these tangential electric field components at $x = 0$, we get

$$\vec{E}_{i,tangential}(x = 0, y) = E_{0i}(\hat{a}_y \cos \theta_i) e^{-jk_1(y \sin \theta_i)} \quad (2.12a)$$

$$\vec{E}_{r,tangential}(x = 0, y) = E_{0r}(\hat{a}_y \cos \theta_r) e^{-jk_1(y \sin \theta_r)} \quad (2.12b)$$

$$\vec{E}_{t,tangential}(x = 0, y) = E_{0t}(\hat{a}_y \cos \theta_t) e^{-jk_2(y \sin \theta_t)} \quad (2.12c)$$

When Equations 2.12a-b and c are inserted into the Boundary Conditions in Equation 2.10, the non-trivial solution exists only if the phase terms of the incident, reflected, and transmitted wave components in Equation 2.12 must be equal to each other (phase-matching condition) as

$$k_1(y \sin \theta_i) = k_1(y \sin \theta_r) = k_2(y \sin \theta_t) \quad (2.13)$$

Thus, Snell's Laws of Reflection (in Equation 2.14a) and the Snell's Law of Refraction (in Equation 2.14b) follow from Equation 2.13 as

$$\theta_i = \theta_r \quad (2.14a)$$

$$k_1 \sin \theta_i = k_2 \sin \theta_t \quad (2.14b)$$

writing the wavenumbers k_1 and k_2 (in media 1 and 2, respectively) in terms of the refractive indices n_1, n_2 and the free-space wavenumber $k_0 = \omega \sqrt{\epsilon_0 \mu_0}$, the Snell's Law of refraction can also be written as

$$n_1 \sin \theta_i = n_2 \sin \theta_t \quad (2.14)$$

Substituting Equations 2.12 through 2.14 into Equation 2.10 results in

$$(E_{0i} + E_{0r}) \cos \theta_i = E_{0t} \cos \theta_t \quad (2.15)$$

Note: All the angles θ_i , θ_r and θ_t are confined to the first quadrant (i.e., they are defined in the range from zero to 90 degrees). To obtain the Fresnel Reflection coefficient for this p-polarization problem as

$$r_{12} = \frac{E_{0r}}{E_{0i}} \quad (2.16)$$

The second boundary condition for the continuity of the tangential component of the total magnetic field intensity vector should be imposed at the boundary, $x = 0$, as there exists no free surface current density vector on the interface. This second boundary condition is stated as

$$H_i(x = 0) + H_r(x = 0) = H_t(x = 0) \quad (2.17)$$

Using the H-field expressions given in Equation set 2.8 and imposing the phase-matching condition again at $x = 0$, we obtain

$$\vec{H}_i(x = 0, y) = \frac{E_{0i}}{\eta_1} (\hat{a}_z) e^{-jk_1(y \sin \theta_i)} \quad (2.18a)$$

$$\vec{H}_r(x = 0, y) = \frac{E_{0r}}{\eta_1} (-\hat{a}_z) e^{-jk_1(y \sin \theta_r)} \quad (2.18b)$$

$$\vec{H}_t(x = 0, y) = \frac{E_{0t}}{\eta_2} (\hat{a}_z) e^{-jk_2(y \sin \theta_t)} \quad (2.18c)$$

Substituting Equations 2.18a,b,c into Equation 2.17 yields Equation 2.19a or 2.19b as

$$\frac{E_{0i}}{\eta_1} - \frac{E_{0r}}{\eta_1} = \frac{E_{0t}}{\eta_2} \quad (2.19a)$$

or

$$\frac{\eta_2}{\eta_1}(E_{0i} + E_{0r}) = E_{0t} \quad (2.19b)$$

Solving Equation 2.19b and Equation 2.15 simultaneously, while using the definition in Equation 2.16, the reflection coefficient $r_{12,p}$ for the p-polarization (TM-polarization) case is obtained as

$$r_{12,p} = \frac{E_{0r}}{E_{0i}} = \frac{\eta_2 \cos \theta_t - \eta_1 \cos \theta_i}{\eta_2 \cos \theta_t + \eta_1 \cos \theta_i} \quad (2.20)$$

The transmission coefficient for p-polarization, $t_{12,p}$, can also be defined and obtained in the meantime as

$$t_{12,p} = \frac{E_{0t}}{E_{0i}} = \frac{2\eta_2 \cos \theta_t}{\eta_2 \cos \theta_t + \eta_1 \cos \theta_i} \quad (2.21)$$

The expressions in Equations 2.20 and 2.21 are known as Fresnel Formulas for reflection and transmission coefficients for a 2-layer system under p-polarized excitation. The analysis presented so far applies to lossy as well as lossless media, including lossy dielectric materials and lossy conductors.

For the problems in optical frequencies, expressing Equations 2.20 and 2.21 in terms of the refractive indices of layers is more convenient. Using the well-known expression $\eta = \frac{\eta_0}{n}$, it can be written that

$$r_{12,p} = \frac{n_2 \cos \theta_i - n_1 \cos \theta_t}{n_2 \cos \theta_i + n_1 \cos \theta_t} \quad (2.22a)$$

$$t_{12,p} = \frac{2n_1 \cos \theta_i}{n_2 \cos \theta_i + n_1 \cos \theta_t} \quad (2.22b)$$

It can be easily shown that the reflection and transmission coefficients satisfy the following equality

$$\frac{n_2}{n_1} t_{12,p} = r_{12,p} + 1 \quad (2.23)$$

In addition, when the incident UPW comes from the 2nd medium onto the 1st medium, associated reflection and transmission coefficients can be written by analogy just by interchanging the indices as

$$r_{21,p} = \frac{n_1 \cos \theta_t - n_2 \cos \theta_i}{n_1 \cos \theta_t + n_2 \cos \theta_i} \quad (2.24a)$$

$$t_{21,p} = \frac{2n_2 \cos \theta_t}{n_1 \cos \theta_t + n_2 \cos \theta_i} \quad (2.24b)$$

where θ_t acts like the incidence angle.

We need to extend these formulations to a system of planar multilayers with the ultimate purpose of applying it to the SPR problem. For the ease of analysis, the equations obtained for the reflection and transmission coefficients above can be expressed in terms of the x-components of the propagation vectors, k_x , and the relative permittivity, ϵ_r only by eliminating the cosine terms of the incidence and

transmission angles. Let the subscript 'a' denote either the first or the second medium in Equation 2.25 below

$$\vec{k}_a = n_a \vec{k}_0 = \hat{a}_x k_{ax} + \hat{a}_y k_{ay} \quad (2.25)$$

where \vec{k}_0 is the free space propagation vector, and its amplitude, the free space wavenumber, is $k_0 = 2\pi/\lambda_0$. Thus,

$$k_a^2 = k_{ax}^2 + k_{ay}^2 \quad (2.26a)$$

$$k_a^2 = n_a^2 k_0^2 = \epsilon_a k_0^2 \quad (2.26b)$$

Since the angle of the propagation vector \vec{k}_a concerning boundary normal is θ_a where $\theta_1 = \theta_i$ (the incidence angle) and $\theta_2 = \theta_t$ (the transmission angle) for $a = 1$, or 2,

$$k_{ax} = k_a \cos \theta_a = n_a k_0 \cos \theta_a \quad (2.27a)$$

$$k_{ay} = k_a \sin \theta_a = n_a k_0 \sin \theta_a \quad (2.27b)$$

As imposed by the phase-matching condition (resulting from the application of boundary conditions), we have

$$k_{1y} = k_{2y} = n_1 k_0 \sin \theta_i \quad (2.28)$$

However, such a relation does not exist for x-components of the propagation vectors. Rewriting

$$k_1 = n_1 k_0 \quad (2.29a)$$

$$k_2 = n_2 k_0 \quad (2.29b)$$

where k_1 and k_2 are magnitudes of propagation vectors \vec{k}_1 and \vec{k}_2 . Using Equations 2.26a and 2.26b to express the x-components of the propagation vectors in both media, we get

$$k_{ax}^2 = \epsilon_a k_0^2 - k_{ay}^2 = \epsilon_a k_0^2 - (k_0 n_a \sin \theta_a)^2 \quad (2.30)$$

Using Equations 2.28 through 2.30,

$$k_{1x}^2 = \epsilon_1 k_0^2 - (k_0 n_1 \sin \theta_i)^2 \quad (2.31a)$$

$$k_{2x}^2 = \epsilon_2 k_0^2 - (k_0 n_1 \sin \theta_t)^2 \quad (2.31b)$$

Equation 2.31b defines the propagation constant in medium 2 in terms of incidence angle, eliminating the refraction angle calculations. The square root of the x-component of the propagation vector can be calculated as

$$k_{1x} = \pm \sqrt{k_{1x}^2} \quad (2.32a)$$

$$k_{2x} = \pm \sqrt{k_{2x}^2} \quad (2.32b)$$

Correct roots must be selected with the proper signs for k_{ax} ($a = 1, \text{ or } 2$) in Equation 2.32 as the physical constraints require that the electromagnetic fields must remain finite in both media as $|x|$ grows to infinity in both semi-infinite layers. Then, the x-components of the propagation vectors can be used to eliminate angle terms in the reflection coefficient expression. Using Snell's Law of refraction to express refractive indices in terms of each other

$$n_1 = \frac{\sin \theta_2}{\sin \theta_1} n_2 \quad (2.33a)$$

$$n_2 = \frac{\sin \theta_1}{\sin \theta_2} n_1 \quad (2.33b)$$

And then, using Equation 2.29 in 2.33, we get

$$n_1 = \frac{\sin \theta_2 k_2}{\sin \theta_1 k_0} \quad (2.34a)$$

$$n_2 = \frac{\sin \theta_1 k_1}{\sin \theta_2 k_0} \quad (2.34b)$$

Substituting 2.34 into Equation 2.22a, the reflection coefficient is rewritten as

$$r_{12,p} = \frac{\frac{\sin \theta_2 k_2}{\sin \theta_1 k_0} \cos \theta_t - \frac{\sin \theta_1 k_1}{\sin \theta_2 k_0} \cos \theta_i}{\frac{\sin \theta_2 k_2}{\sin \theta_1 k_0} \cos \theta_t + \frac{\sin \theta_1 k_1}{\sin \theta_2 k_0} \cos \theta_i} \quad (2.35)$$

Equation 2.35 can be simplified by canceling the k_0 terms and substituting $k_{ax} = k_a \cos \theta_a$ for values for $a = 1$, or 2, for both media, to get

$$r_{12,p} = \frac{\frac{\sin \theta_2}{\sin \theta_1} k_{2x} - \frac{\sin \theta_1}{\sin \theta_2} k_{1x}}{\frac{\sin \theta_2}{\sin \theta_1} k_{2x} + \frac{\sin \theta_1}{\sin \theta_2} k_{1x}} \quad (2.36)$$

Finally, using Snell's Law of refraction to express the ratio of the sine of the incidence and transmittance angles as shown below,

$$\sin \theta_1 \sqrt{\epsilon_1} = \sin \theta_2 \sqrt{\epsilon_2} \rightarrow \frac{\sin \theta_1}{\sin \theta_2} = \frac{\sqrt{\epsilon_2}}{\sqrt{\epsilon_1}} \quad (2.37)$$

Equation 2.36 can be further simplified as

$$r_{12,p} = \frac{\frac{\sqrt{\epsilon_1}}{\sqrt{\epsilon_2}} k_{2x} - \frac{\sqrt{\epsilon_2}}{\sqrt{\epsilon_1}} k_{1x}}{\frac{\sqrt{\epsilon_1}}{\sqrt{\epsilon_2}} k_{2x} + \frac{\sqrt{\epsilon_2}}{\sqrt{\epsilon_1}} k_{1x}} \quad (2.38)$$

Multiplying both numerator and denominator by $\sqrt{\epsilon_1 \epsilon_2}$ will yield

$$r_{12,p} = \frac{k_{2x} \epsilon_1 - k_{1x} \epsilon_2}{k_{2x} \epsilon_1 + k_{1x} \epsilon_2} \quad (2.39)$$

Equation 2.39 gives the reflection coefficient for the 2-layer p-polarization problem in terms of the permittivity values and the x-components of the propagation vectors.

The transmission coefficient can also be obtained similarly as

$$t_{12,p} = \frac{2k_{1x} \epsilon_1}{k_{2x} \epsilon_1 + k_{1x} \epsilon_2} \quad (2.40)$$

Similar derivation steps can be repeated for the reverse reflection and transmission coefficients $r_{21,p}$ and $t_{21,p}$ as

$$r_{21,p} = \frac{k_{1x} \epsilon_2 - k_{2x} \epsilon_1}{k_{1x} \epsilon_2 + k_{2x} \epsilon_1} \quad (2.41a)$$

$$t_{21,p} = \frac{2k_{2x} \epsilon_2}{k_{1x} \epsilon_2 + k_{2x} \epsilon_1} \quad (2.41b)$$

to be used in the derivations of the next subsection of a Three-Layer system.

2.1.1 The Reflectivity of a Three-Layer System

The three-layer system contains three material layers separated by two boundaries and represents the simplest SPR sensor structure. Three-layer systems include a

finite-thickness slab sandwiched between two semi-infinite media, as shown in Figure 2.2. For an SPR sensor, the slab is a lossy metal that is sandwiched between the dielectric prism layer and another dielectric layer, which is the sample medium to be tested. The sample medium is also called the sensing layer or the bulk layer or the substrate layer depending upon the application of the SPR sensor. Reflection coefficients at the boundaries of this three-layer system can be calculated using Equation 2.39 as

$$r_{12} = \frac{k_{2x}\epsilon_1 - k_{1x}\epsilon_2}{k_{2x}\epsilon_1 + k_{1x}\epsilon_2} \quad (2.42a)$$

$$r_{23} = \frac{k_{3x}\epsilon_2 - k_{2x}\epsilon_3}{k_{3x}\epsilon_2 + k_{2x}\epsilon_3} \quad (2.42b)$$

Reflected field components must be calculated to find reflectivity, as implied in the previous section. Since the sample (medium 3) is assumed to be infinitely thick along the x-direction, the incident wave will be reflected from boundary 12, then from 23. The wave transmitted to medium 3 will only propagate in the forward direction. Similarly, for the reflected waves, after the wave reaches medium 1, there will be no backward traveling component. For the sake of simplicity, additional phase and loss caused by traveling in medium 1 can be neglected; this phase component and loss can be easily eliminated in final calculations, or by calibration, in the case of real measurements.

As explained, the reflected wave sensed by the detector will be formed in the steady-state as the result of multiple (infinitely many) reflections/refractions occurring at boundary 12 (between media 1 and 2) and at boundary 23 (between media 2 and 3). The signal is transmitted to medium 2 at boundary 12 will propagate in medium 2. It will then be reflected from boundary 23 and propagate in medium 2 again towards boundary 12 to go through another cycle of reflection/refraction; this will be repeated infinitely many times.

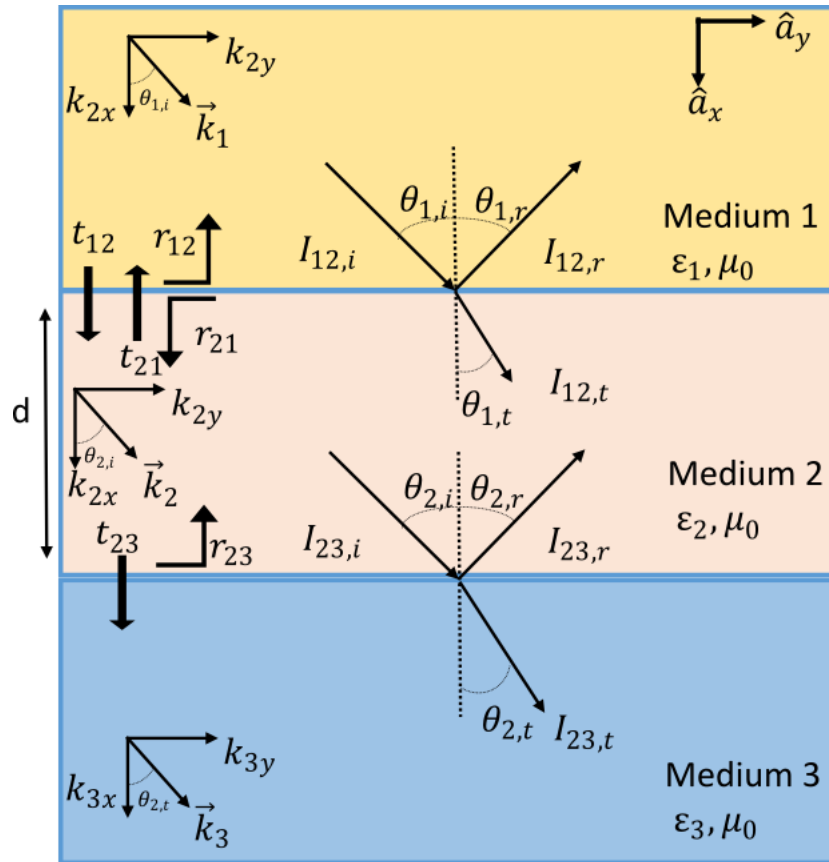


Figure 2.2: 3-layer / 2-boundary reflection problem, the thin film in the middle has a finite thickness of d , and medium 3 assumed to be infinite.

The magnitude of the reflection coefficient for the reflected (backward traveling) waves will be equal with transmitted (forward traveling) waves as seen from Equations 2.39 and 2.41a for any boundary ab

$$r_{ab} = -r_{ba} \quad (2.43)$$

Reverse and forward transmission coefficients can be expressed in terms of the forward reflection coefficient for any boundary ab . Using Equation 2.23, it can be shown that

$$t_{ab} = (r_{ab} + 1) \frac{n_1}{n_2} \quad (2.44a)$$

$$t_{ba} = (r_{ba} + 1) \frac{n_2}{n_1} = (1 - r_{ab}) \frac{n_2}{n_1} \quad (2.44b)$$

Multiplying both terms yields

$$t_{ab}t_{ba} = (r_{ab} + 1) \frac{n_1}{n_2} (1 - r_{ab}) \frac{n_2}{n_1} \quad (2.45b)$$

thus

$$t_{ab}t_{ba} = 1 - r_{ab}^2 \quad (2.46b)$$

To calculate the overall reflected field, coefficients r_{12} , r_{23} , t_{12} , and the thickness of medium 2, d , should be known. Assume that the incident electric field amplitude at the boundary is I (i.e., $E_{0i} = I$), reflected and transmitted waves from medium 1 to medium 2 will be

$$I_{12,t} = I t_{12} \quad (2.47a)$$

$$I_{r,1} = I r_{12} \quad (2.47b)$$

$I_{r,1}$ is the first reflection as some portion of the wave is directly reflected from the first boundary. For the second reflection, field intensity after traveling in medium 2 to its boundary with medium 3

$$I_{23,i} = I t_{12} \exp(j k_{2x} d) \quad (2.48)$$

where d is the thickness, and k_{2x} is the x component of the propagation vector in medium 2. The component reflected from boundary 23

$$I_{23,r} = I r_{23} t_{12} \exp(-j k_{2x} d) \quad (2.49)$$

The reflected wave will travel in medium 2 backward before being transmitted to medium 1. Since the distance is the same, phase delay will be doubled

$$I_{21,i} = I r_{23} t_{12} \exp(-2j k_{2x} d) \quad (2.50)$$

Note that since the k is a complex number, this equation includes attenuation in the material too. At the next step, a portion of the wave will be transmitted back to medium 1. However, some of it will stay in medium 2 and bounce again. The result of the first reflection

$$I_{r,2} = I t_{21} r_{23} t_{12} \exp(-2j k_{2x} d) \quad (2.51)$$

$I_{r,2}$ represents the second reflection. From a similar approach, the third reflection will be

$$\begin{aligned} I_{r,3} &= I t_{21} r_{23} r_{21} r_{23} t_{12} \exp(-4j k_{2x} d) \\ &= I r_{21} r_{23}^2 t_{12} t_{21} \exp(-4j k_{2x} d) \end{aligned} \quad (2.52)$$

The fourth reflection

$$\begin{aligned} I_{r,4} &= I t_{21} r_{23} r_{21} r_{23} r_{21} r_{23} t_{12} \exp(-6j k_{2x} d) \\ &= I r_{21}^2 r_{23}^3 t_{12} t_{21} \exp(-6j k_{2x} d) \end{aligned} \quad (2.53)$$

As it is clear, there is a repeating pattern; thus, n^{th} reflection

$$I_{r,n} = I t_{12} t_{21} r_{21}^{n-1} r_{23}^n \exp(-2nj k_{2x} d) \quad (2.54)$$

Finally, the total reflected wave can be written as

$$\begin{aligned}
I_{r,total} &= \sum_{n=1}^{\infty} I_{r,n}(n) = I_{r,1} + \sum_{n=2}^{\infty} I_{r,n}(n) \\
&= I_{r,1} + \sum_{n=1}^{\infty} (I t_{12} t_{21} r_{21}^{n-1} r_{23}^n (\exp(-2j k_{2x} d))^n)
\end{aligned} \tag{2.55}$$

as the first reflection does not repeat the pattern. The reflection coefficient is calculated by dividing Equation 2.47 with I , and reorganizing it as follows:

$$\begin{aligned}
r_{123} &= r_{12} + t_{12} t_{21} r_{21} \exp(-2j k_{2x} d) \sum_{n=0}^{\infty} (r_{21}^n r_{23}^n (\exp(-2j k_{2x} d))^n)
\end{aligned} \tag{2.56}$$

The first term of the right-hand side of the equation represents the first reflection; further adjustments are made to obtain geometric series in proper form, which will lead to

$$r_{123} = r_{12} + \frac{t_{12} t_{21} r_{23} \exp(-2j k_{2x} d)}{1 - r_{23} r_{21} \exp(-2j k_{2x} d)} \tag{2.49}$$

Detailed explanation and formulation for the sum of geometric series given in Appendix A. Using Equation 2.46b

$$r_{123} = r_{12} + \frac{(1 - r_{12}^2) r_{23} \exp(-2j k_{2x} d)}{1 + r_{23} r_{12} \exp(-2j k_{2x} d)} \tag{2.57}$$

Including r_{12} into numerator by multiplying with denominator yields

$$r_{123} = \frac{r_{12}(1 + r_{12} r_{23} \exp(-2j k_{2x} d)) + (1 - r_{12}^2) r_{23} \exp(-2j k_{2x} d)}{1 + r_{12} r_{23} \exp(-2j k_{2x} d)} \tag{2.58}$$

Rearranging Equation 2.50 gives the reflectivity

$$r_{123} = \frac{r_{12} + r_{23} \exp(-2jk_{2x} d)}{1 + r_{12}r_{23} \exp(-2jk_{2x} d)} \quad (2.59)$$

and the reflectance is

$$R_{123} = |r_{123}|^2 \quad (2.60)$$

2.1.2 The Reflectivity of N-layer Systems

The reflectivity of any multilayered system can be calculated using three-layer reflectance. Simply, every system can be reduced to a three-layer system if solved step by step. For a four-layer system, the boundaries are 12, 23, and 34. Reflection coefficients can be calculated using the same method in the previous section. Thus, for a four-layer system, the propagation constants in each medium are

$$k_{1x}^2 = \epsilon_1 k_0^2 - (k_0 n_1 \sin \theta_1)^2 \quad (2.61a)$$

$$k_{2x}^2 = \epsilon_2 k_0^2 - (k_0 n_2 \sin \theta_2)^2 \quad (2.61b)$$

$$k_{3x}^2 = \epsilon_3 k_0^2 - (k_0 n_3 \sin \theta_3)^2 \quad (2.61c)$$

$$k_{4x}^2 = \epsilon_4 k_0^2 - (k_0 n_4 \sin \theta_4)^2 \quad (2.61d)$$

and the reflection coefficients are written as (using Equation 2.36)

$$r_{12} = \frac{k_{2x}\epsilon_1 - k_{1x}\epsilon_2}{k_{2x}\epsilon_1 + k_{1x}\epsilon_2} \quad (2.62a)$$

$$r_{23} = \frac{k_{3x}\epsilon_2 - k_{2x}\epsilon_3}{k_{3x}\epsilon_2 + k_{2x}\epsilon_3} \quad (2.62b)$$

$$r_{34} = \frac{k_{4x}\epsilon_3 - k_{3x}\epsilon_4}{k_{4x}\epsilon_3 + k_{3x}\epsilon_4} \quad (2.62c)$$

The reflectance of this system can be calculated step by step, similar to a three-layer system. Though, four-layered structures can be considered as three layered-systems where the two bottom layers have the reflectivity of r_{234} , which is derived in the previous section. Using Equation 2.59

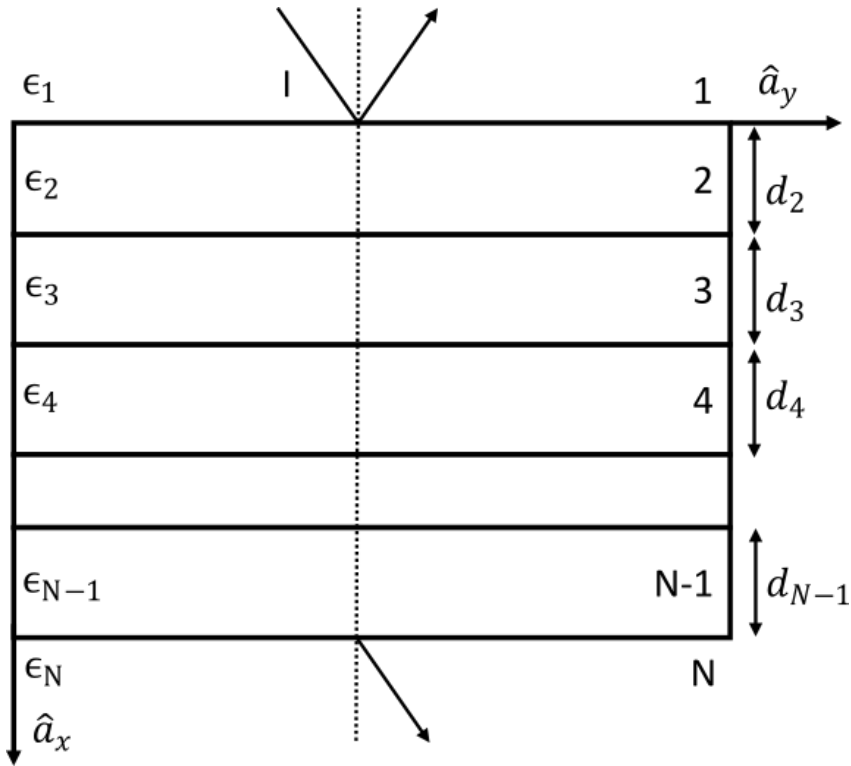


Figure 2.3: Geometry for N-layer reflectivity problem. The wave is sent from medium 1, with no reflections within medium N (thickness of the first and last medium are assumed to be infinite).

$$r_{234} = \frac{r_{23} + r_{34} \exp(2jk_{3x} d_3)}{1 + r_{23}r_{34} \exp(2jk_{3x} d_3)} \quad (2.63)$$

where d_3 is the thickness of layer 3 since the wave propagates in medium 3 for this case to reduce this system to three-layers, reflectance can be derived similarly with

the three-layer case. The first reflection and transmission will be the same as in the previous section. Thus

$$I_{12,t} = I t_{12} \quad (2.64a)$$

$$I_{r,1} = I r_{12} \quad (2.64b)$$

As it is in the 3-layer case, the wave will now propagate in medium 2 through medium 3, where the reflection coefficient between medium 2 and medium 3 is r_{23} . After reaching the boundary, the wave will be reflected to boundary 12, the transmitted portion that gives the second reflection is

$$I_{r,2} = I t_{21} r_{234} t_{12} \exp(-2j k_{2x} d_2) \quad (2.65)$$

$I_{r,2}$ represents the second reflection. From a similar approach, the third reflection will be

$$\begin{aligned} I_{r,3} &= I t_{21} r_{234} r_{21} r_{234} t_{12} \exp(-4j k_{2x} d_2) \\ &= I r_{21} r_{234}^2 t_{12} t_{21} \exp(-4j k_{2x} d_2) \end{aligned} \quad (2.66)$$

The fourth reflection

$$\begin{aligned} I_{r,4} &= I t_{21} r_{234} r_{21} r_{234} r_{21} r_{234} t_{12} \exp(-6j k_{2x} d_2) \\ &= I r_{21}^2 r_{234}^3 t_{12} t_{21} \exp(-6j k_{2x} d_2) \end{aligned} \quad (2.67)$$

And the n^{th} reflection

$$I_{r,n} = I t_{12} t_{21} r_{21}^{n-1} r_{234}^n \exp(-2nj k_{2x} d_2) \quad (2.68)$$

As seen through Equation 2.68, reflections of the four-layer system are the same as the three-layer system; the only difference is having r_{234} instead of r_{23} . Thus, for the four-layer system, reflectivity is

$$r_{1234} = \frac{r_{12} + r_{234} \exp(-2jk_{2x} d_2)}{1 + r_{12}r_{234} \exp(-2jk_{2x} d_2)} \quad (2.69)$$

And the reflectance is

$$R_{1234} = |r_{1234}|^2 \quad (2.70)$$

Hence, the reflectance of any system with any number of layers can be calculated by reducing them step by step, starting from the bottom three layers, and recursively using previously calculated reflectivity. Thus, N-layer reflectivity can be calculated as

$$r_{123456\dots N} = \frac{r_{12} + r_{234\dots N} \exp(2jk_{2x} d_2)}{1 + r_{12}r_{234\dots N} \exp(2jk_{2x} d_2)} \quad (2.71)$$

Since the systems used in further chapters contain three and four layers, only Equations 2.53 and 2.63 will be used. N-layer reflectance can be calculated with the transfer-matrix method more conveniently since its cascaded matrix multiplication property allows faster calculations. Since N-layer general calculations are not required for the scope of the thesis, the transfer-matrix method will not be discussed here [121].

2.2 Dispersion Relation of Surface Plasmons

Dispersion relation of surface plasmons can be calculated using Maxwell Equations [119], [120], [122]. For any two-layer, metal-dielectric system sketched in Figure

2.1 (we do not consider coupling prism in this calculations, as it only serves as a ‘coupler’), the curl equation for H-field is

$$\nabla \times \vec{H} = j\omega\epsilon\vec{E} \quad (2.72)$$

where the H-field only has a z-component. Substituting field expressions given in Equation 2.8 into Equation 2.72, it can be written as

$$\hat{a}_x \frac{\partial H_z}{\partial y} - \hat{a}_y \frac{\partial H_z}{\partial x} = j\omega\epsilon(\hat{a}_x E_x + \hat{a}_y E_y) \quad (2.73)$$

Using vector equality and substituting partial derivatives yields

$$k_y H_z = \omega\epsilon E_x \quad (2.74a)$$

$$k_x H_z = -\omega\epsilon E_y \quad (2.74b)$$

Equation 2.74a derived from the equality of x-components while Equation 2.74b derived from y-components. Rewriting Equation 2.74a,b for medium 1 and medium 2

$$k_{1y} H_{1z} = \omega\epsilon_1 E_{1x} \quad (2.75a)$$

$$k_{2y} H_{2z} = \omega\epsilon_2 E_{2x} \quad (2.75b)$$

$$k_{1x} H_{1z} = -\omega\epsilon_1 E_{1y} \quad (2.75c)$$

$$k_{2x} H_{2z} = -\omega\epsilon_2 E_{2y} \quad (2.75d)$$

Boundary conditions for the tangential component of total E-field were given in Equation 2.10, rewriting boundary conditions for continuity of tangential components of total H- and E-fields

$$H_{1,tangential} = H_{2,tangential} \quad (2.76a)$$

$$E_{1,tangential} = E_{2,tangential} \quad (2.76b)$$

$$\epsilon_1 E_{1,normal} = \epsilon_2 E_{2,normal} \quad (2.76c)$$

Tangential component E-field is in y-direction while the tangential component of H-field is in the z-direction. Thus

$$E_{1y} = E_{2y} \quad (2.77a)$$

$$H_{1z} = H_{2z} \quad (2.77b)$$

$$\epsilon_1 E_{1x} = \epsilon_2 E_{2x} \quad (2.77c)$$

Using Equations 2.77a,b with Equations 2.75c ,d

$$\frac{k_{2x}}{\epsilon_2} H_{2z} = \frac{k_{1x}}{\epsilon_1} H_{1z} \quad (2.78)$$

Substituting continuity of H-field from Equation 2.77b to Equation 2.78

$$\frac{k_{2x}}{\epsilon_2} - \frac{k_{1x}}{\epsilon_1} = 0 \rightarrow \frac{k_{2x}}{\epsilon_2} = \frac{k_{1x}}{\epsilon_1} \quad (2.79)$$

Similarly, using Equations 2.77b,c with Equations 2.75a, b

$$k_{1y} H_{1z} = k_{2y} H_{2z} \rightarrow k_{1y} = k_{2y} \quad (2.80)$$

Equation 2.79 is the condition for the existence of SPs and valid for any boundary [118]. This condition can be used to obtain dispersion relation for SPs in a metal/dielectric boundary. Using Equation 2.29 with Equation 2.31 for medium 1 and medium 2 yields

$$k_y^2 + k_{1x}^2 = \epsilon_1 k_0^2 \quad (2.81a)$$

$$k_y^2 + k_{2x}^2 = \epsilon_2 k_0^2 \quad (2.81b)$$

Modifying equations to obtain k_{1x} and k_{2x}

$$k_{1x}^2 = \epsilon_1 k_0^2 - k_y^2 \quad (2.82a)$$

$$k_{2x}^2 = \epsilon_2 k_0^2 - k_y^2 \quad (2.82b)$$

Substituting k_{1x} and k_{2x} from Equation 2.82a,b into the square of Equation 2.79

$$\frac{\epsilon_2 k_0^2 - k_y^2}{\epsilon_2^2} - \frac{\epsilon_1 k_0^2 - k_y^2}{\epsilon_1^2} = 0 \quad (2.83)$$

Rearranging Equation 2.83 to obtain an equation for k_y

$$k_y = k_{y,sp} = k_0 \sqrt{\frac{\epsilon_1 \epsilon_2}{\epsilon_1 + \epsilon_2}} \quad (2.84)$$

Equation 2.84 gives the dispersion relation for a metal/dielectric boundary. The propagation vector normal to the boundary can be obtained for media 1 and 2 separately [118].

$$k_{1x,sp} = \pm k_0 \sqrt{\frac{\epsilon_1^2}{\epsilon_1 + \epsilon_2}} \quad (2.85a)$$

$$k_{2x,sp} = \pm k_0 \sqrt{\frac{\epsilon_2^2}{\epsilon_1 + \epsilon_2}} \quad (2.85b)$$

Sign of k_x should be appropriately selected to ensure exponential decay of fields as they get farther away from the boundary, i.e., to confine the wave to the boundary. Equations 2.84 and 2.85, together with Equation 2.79, have implications on SPs' coupling conditions: SPWs are surface-bound modes; thus, signs of k_{1x} and k_{2x} must

be different. Hence, from Equation 2.79, we know that signs of ϵ_1 and ϵ_2 should be different. To have real k_y

$$\text{Re}\{\epsilon_1 + \epsilon_2\} < 0 \quad (2.86)$$

The aforementioned inverse-sign condition implies that one of the materials must have a permittivity with a negative real part; this can be achieved using metals or highly N-doped semiconductors. Metals are much more commonly preferred to fulfill this task. Assuming medium 2 is a metal, the permittivity of any metal can be written as

$$\epsilon_{r,m} = \epsilon_2' + j\epsilon_2'' \quad (2.87)$$

The real part of metal permittivity, ϵ_2' , is always negative below the plasma frequency, and the imaginary part of the metal permittivity is generally much smaller than its real part below plasma frequency, as to be discussed in Chapter 3. Assuming material 1 is the dielectric with positive and real permittivity, the condition given in Equation 2.86 now becomes

$$|\epsilon_2'| > \epsilon_1 \quad (2.88)$$

Satisfying this condition will create the fully-bound modes in the boundary by yielding a real k_y and imaginary k_x in both media. Equation 2.85 can be used to calculate the probe depth of SPs, while the imaginary part of Equation 2.84 gives the reach of surface plasmons through the boundary.

2.2.1 Coupling of Surface Plasmons

Surface Plasmons are initially observed in metallic diffraction gratings by American scientist Robert W. Wood in 1902 [14]. Ordinary metal surfaces do not support SPs

and to excite SPs, due to mismatch between free space wavenumber and SP wavevector given in Equation 2.84; the component of the propagation vector of the incident wave that is parallel to the boundary surface must be equal to the propagation vector of the SP waves. This requirement is called the coupling condition. The coupling condition varies with the surface topology and material types. Multilayer systems would require a different approach for coupling conditions. For a structure as shown in Figure 2.1, coupling condition in its most general form can be given as

$$k_{sp} = k_{y,inc} \quad (2.89)$$

The y-component of the incident propagation vector appears in the condition given above since the plane of incidence is the x - y plane and the boundary surfaces are placed at $x = \text{constant}$ planes (i.e., k_y should be considered in Equation 2.89) as defined in Figure 2.2. The main goal is to assure

$$k_{sp} < k_{inc} \quad (2.90)$$

to start with, then the condition in Equation 2.89 can be achieved, and a resonance spectrum can be generated either by tilting the incident wave (i.e., changing the angle of incidence) or by changing the frequency (or wavelength equivalently), as k_y is dependent on both of these parameters. Coupling methods are used to manipulate the tangential component of the incident propagation vector to match it with the propagation vector of the SP waves to satisfy Equation 2.89 since the amplitude of the wavevector of the incident wave is always smaller than that of the plasmons, as implied in Equation 2.84. The increase in wavevector required for matching is

$$\Delta k = k_{sp} - k_{inc,y} \quad (2.91)$$

2.2.1.1 Grating Couplers

Coupling with diffraction gratings is the reason behind Robert W. Wood's initial discovery in 1920. He was observed “diffraction anomalies on metallic diffraction gratings” due to the excitation of SPs [14]–[16]. The effect of gratings and any surface roughness can be modeled as a combination of multiple gratings. Grating couplers shift the momentum of the incident wave with a certain degree related to the grating period and couples the incident wave to surface plasmons in this way.

Grating couplers can be used as reflection and diffraction gratings in SPR configurations. A reflection grating coupler is placed below the sample in a reflection system. Thus the wave travels through to sample and is reflected from the grating. Such systems limit the size of the samples, and only optically transparent samples can be used. On the other hand, diffraction grating couplers are placed above the structure. Typically as a part of the metal of the structure. Such systems do not limit the sample size or require optically transparent samples.

Theoretical analysis for grating coupling systems requires rigorous coupled-wave analysis and is relatively more complicated to analyze than prism coupled systems. Besides, grating coupled systems generally exhibit less accuracy and introduce more limitations, as mentioned in [31], [106]. Thus, the use of grating couplers was not preferred in this thesis. Other coupling methods, such as fiber optical cables, are based on ATR mechanisms similar to coupling with prisms. Examples of coupling with fiber optical cables are widely mentioned in the literature [123]–[128].

2.2.1.2 Coupling Prisms

Coupling prisms are made of glasses with high-refractive-index values. In this coupling approach, incident light is first passed through the high-refractive-index prism to increase the momentum of the light before photons interact with plasmons.

Coupling prisms are first introduced by Otto [21], and Kretschmann and Raether [22] in different configurations, and independently. Otto suggested a configuration with an air gap between prism and metal. Using Figure 2.2 as a reference, in this configuration, layers 1, 2, and 3 correspond to the prism, the air gap, and the metal, respectively. In the Kretschmann and Raether (KR) configuration, on the other hand, the metal layer is placed directly below the prism. In this case, layers 1, 2, and 3 correspond to the prism, the metal layer, and the dielectric layer, respectively.

Otto configuration has some disadvantages when compared to KR configuration. It limits sample size, and reproducing the same air gap is difficult in practice. Coupling with prisms is called as Otto-Kretschmann Method, Otto-Kretschmann-Raether Method, or ATR method.

The SPR configurations in KR approach are generally created with a matching liquid or evaporating metal over prism instead of engraving metal, such as in the grating couplers. Mathematically, matching by prism can be explained as changing the refractive index of the incident wave, such as

$$k_{inc,y} = n_p k_{inc,0} \sin \theta_i \quad (2.92)$$

Where $k_{inc,0}$ is the free space wavenumber, and n_p is the refractive index of prism. As Equation 2.92 implies, any n_p larger than 1 will increase the incident k to match it with k_{sp} .

In the derivations presented in this chapter so far, a prism coupled sensor structure is assumed due to the relative simplicity of the analysis. Additionally, the SPR systems with prism couplers are reported to be more accurate in general [48].

2.2.2 Penetration Depth of Surface Plasmons

SP waves are evanescent in nature, propagating along the boundary surface between the metal and dielectric layers and extending into metal and dielectric. The extent of these surface waves is minimal, and most of the wave is concentrated in the dielectric layer. In typical configurations, SP waves can penetrate 20-50 nm into metal and 100-500 nm into the dielectric, and the tangential extent of the waves is around a few hundred micrometers [1], [129]. The extent of SP waves is an essential practical concern since the sensing occurs in the area where the SPR is active. The penetration depths within the metal and the dielectric are given in Equations 2.93a and 2.93b, respectively, where the x-components of the propagation vectors are given in Equation 2.85.

$$L_{sp,m} = \frac{1}{Re[k_{m,x}]} \quad (2.93a)$$

$$L_{sp,d} = \frac{1}{Re[k_{d,x}]} \quad (2.93b)$$

While the derivation of propagation vectors in the previous section is only valid for two-layered systems, Equation 2.93 can be used for all cases. Dielectrics used as sensing films have relatively low losses compared to metals and most substrates; penetration is generally not an issue in multilayered systems with more than one dielectrics. On the cases with more than one metal layer is used as in [130]–[132], then the penetration depth within the test sample must be computed step by step carefully.

Penetration depth is critical in biosensing applications. The extent of the SP waves must be large enough to probe a necessary depth to provide accurate measurements while using a chemical or biological substrate for concentration measurements. On the other hand, if the medium under test is a gaseous substrate, for instance, the extent of the SP waves is not critical.

2.3 The Requirement of P-Polarization in SPR Sensor Operation

Surface plasmons can only be excited by p-polarized waves; accordingly, solutions in previous sections were presented for the p-polarization case. This can be proven by calculating the propagation vector for an s-polarized incident wave. For an s-polarized TEM wave, using Figure 2.2 as a reference, the field components for a UPW wave are given as

$$\vec{H}_i(x, y) = \frac{E_{0i}}{\eta_1} (-\hat{a}_x \sin\theta_i + \hat{a}_y \cos\theta_i) e^{-jk_1(x \cos\theta_i + y \sin\theta_i)} \quad (2.94a)$$

$$\vec{E}_i(x, y) = E_{0i}(-\hat{a}_z) e^{-jk_1(x \cos\theta_i + y \sin\theta_i)} \quad (2.94b)$$

$$\vec{H}_r(x, y) = \frac{E_{0r}}{\eta_1} (\hat{a}_x \sin\theta_r + \hat{a}_y \cos\theta_r) e^{-jk_1(-x \cos\theta_r + y \sin\theta_r)} \quad (2.94c)$$

$$\vec{E}_r(x, y) = E_{0r}(\hat{a}_z) e^{-jk_1(-x \cos\theta_r + y \sin\theta_r)} \quad (2.94d)$$

$$\vec{H}_t(x, y) = \frac{E_{0t}}{\eta_2} (-\hat{a}_x \sin\theta_t + \hat{a}_y \cos\theta_t) e^{-jk_2(x \cos\theta_t + y \sin\theta_t)} \quad (2.94e)$$

$$\vec{E}_t(x, y) = E_{0t}(-\hat{a}_z) e^{-jk_2(x \cos\theta_t + y \sin\theta_t)} \quad (2.94f)$$

Starting with curl equation for E-field

$$\nabla \times \vec{E} = -j\omega\mu_0\vec{H} \quad (2.95)$$

since E-field only has a z-component

$$\hat{a}_x \frac{\partial E_z}{\partial y} - \hat{a}_y \frac{\partial E_z}{\partial x} = -j\omega\mu_0(\hat{a}_x H_x + \hat{a}_y H_y) \quad (2.96)$$

using vector equality and substituting partial derivatives yields

$$k_y E_z = \omega\mu_0 H_x \quad (2.97a)$$

$$k_x E_z = -\omega\mu_0 H_y \quad (2.97b)$$

rewriting Equations 2.97a,b for both media

$$k_{1y} E_{1z} = \omega\mu_0 H_{1x} \quad (2.98a)$$

$$k_{2y} E_{2z} = \omega\mu_0 H_{2x} \quad (2.98b)$$

$$k_{1x} E_{1z} = -\omega\mu_0 H_{1y} \quad (2.98c)$$

$$k_{2x} E_{2z} = -\omega\mu_0 H_{2y} \quad (2.98d)$$

using Boundary Conditions from Equation 2.76

$$E_{1z} = E_{2z} \quad (2.99a)$$

$$H_{1y} = H_{2y} \quad (2.99b)$$

$$H_{1x} = H_{2x} \quad (2.99c)$$

from Equation 2.76 and 2.99

$$k_{1y} E_{1z} = k_{2y} E_{2z} \rightarrow k_{1y} = k_{2y} \quad (2.98a)$$

$$k_{1x} E_{1z} = k_{2x} E_{2z} \rightarrow k_{1x} = k_{2x} \quad (2.98b)$$

using Equations 2.81 and 2.98a

$$\epsilon_1 k_0^2 - k_y^2 = k_{1x}^2 \quad (2.99a)$$

$$\epsilon_2 k_0^2 - k_y^2 = k_{2x}^2 \quad (2.99b)$$

since $k_{1x} = k_{2x}$ from Equation 2.98b

$$k_{1x}^2 = k_{2x}^2 \rightarrow \epsilon_1 k_0^2 = \epsilon_2 k_0^2 \quad (2.100)$$

which has no solution unless $k_0^2 = 0$ or $\epsilon_1 = \epsilon_2$ and leads to inconsistency as both materials are assumed to be different. Thus, Boundary Conditions have no solution for s-polarized waves, and eventually, s-polarized (or TE) waves cannot excite SPWs. This phenomenon can be explained verbally as in the following: excitation of SPWs requires the presence of perpendicular E-field component concerning the boundary surface, while the evanescent wave propagates parallel to the surface, charge oscillations are perpendicular to the surface, which can be provided by a TM-polarized wave only.

2.4 The Requirement of Wavevector Increment

The relation between SP wavevector and incident free-space wavevector was derived in previous parts of this chapter. To excite an SP wave, the following condition must be satisfied

$$Re\{k_{sp}\} = k_{y,inc} \quad (2.101)$$

Verbally, the incident wavevector component parallel to the boundary (y-directed in our problem topology) must match the real part of the SP wavevector. Using the assumption $|\epsilon_2''| \ll |\epsilon_2'|$ which most metals (particularly the metals providing meaningful SPR spectra such as gold and silver) satisfy in optical frequencies, the real part of Equation 2.84 can be approximated as

$$Re\{k_{sp}\} \approx k_0 \sqrt{\frac{\epsilon_2' \epsilon_1}{\epsilon_2' + \epsilon_1}} \quad (2.102)$$

Derivation of real and imaginary parts of k_{sp} given in [113], [129]. Equation 2.102 has an important implication: free space wavenumber of the incident wave is always smaller than the real part of the wavenumber of SP waves as both ϵ_1' and ϵ_2' is larger than 1. The values of the real part of the metal and dielectric permittivity will be

discussed in Chapter 3. Thus, the excitation of SP waves is not possible when the incident light is sent from the air is not possible. This condition was implied by Equation 2.80, too. Thus, to excite surface plasmons, the wavenumber of the incident wave should be increased by sending it through a high refractive index medium such as a prism.

2.5 The Sensitivity of SPR Sensors

The literature on the sensitivity of SPR sensors is very comprehensive [106], [133]–[137]. The sensitivity of SPR sensors is defined in refractive index units (RIU). RIU is defined as the smallest measurable refractive index change. The maximum sensitivity of SPR sensors theoretically proven to be around 10^{-7} RIU by Piliarik et. al.[106]. The authors derived a general, theoretical formulation for the sensitivity of SPR sensors

$$\sigma_{RI} = \frac{K_r}{\sqrt{N}} \frac{(\gamma_i/\gamma_r + 1)^3}{(\gamma_i/\gamma_r)^2} \frac{\epsilon_m'' n^3}{2(\epsilon_m')^2} \frac{\sigma_{I(max)}}{I_0} \quad (2.103)$$

Equation 2.103 defines the sensitivity of SPR sensors in RIU. The equation can be written in a more compact form, such as

$$\sigma_{RI} = ABCD \quad (2.104)$$

The first term of Equation 2.104 is $A = \frac{K_r}{\sqrt{N}}$ where K_r represents the noise distribution factor that depends on the type of sensor, N is the total number of light intensities included in the calculation (i.e., the number of repeated measurements, both temporal and spatial, $N=N_t N_s$); thus, it defines the noise in the system. The second term is $B = \frac{(\gamma_i/\gamma_r+1)^3}{(\gamma_i/\gamma_r)^2}$ symbolizes the attenuation of SPs caused by radiation and absorption. The third term is $C = \frac{\epsilon_m'' n^3}{2(\epsilon_m')^2}$ defined by the real and imaginary parts of metal's

permittivity. Finally in $D = \frac{\sigma_{I(max)}}{I_0}$ where I_0 is the intensity of one wavelength component corresponding to one spectrometer pixel, while $\sigma_{I(max)}$ is the intensity of noise of the highest measured light intensity, this equation ultimately defines the resolution of SPR sensors, final result obtained by the authors given in Figure 2.4.

The equation is derived for the three-layered system, such as the one defined in Figure 2.2. However, it can be easily adapted to a multilayer system by modifying the multiplier B parameters according to the propagation vectors of any multilayered system.

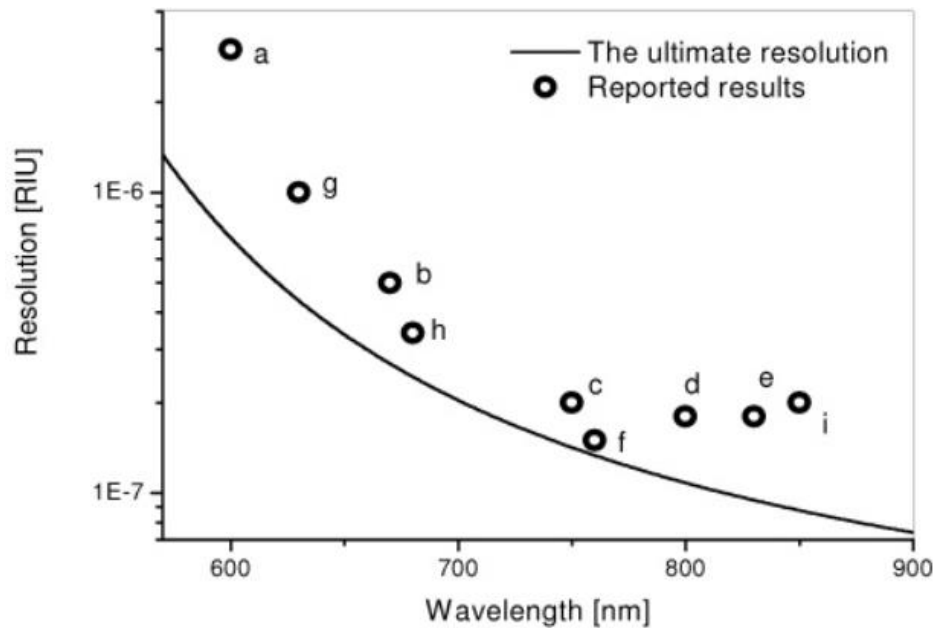


Figure 2.4: The equation gives a theoretical limit for the resolution of an SPR sensor as reported in [106]. The results indicated by small circles are reported in a) [138], b) [139] c) [56], d) [140], e) [137], f) Biacore 3000 (GE Healthcare, USA), g) [92], h) [141], i)[142]. Figure is taken from the original article.

CHAPTER 3

MATERIAL MODELING FOR SPR ANALYSIS

The most straightforward SPR sensor consists of three different material layers; the metal, the coupling prism, and the substrate that serves as the test medium in most applications. Prisms are high refractive index glass structures used to couple incident light to the SP wave, which is excited in the metal-substrate boundary by matching incident light's momentum to the SP's momentum. The resonance case occurs only when the momentum or propagation vector of the SP wave and that of the incident light are matched. The propagation vector of the SP wave is dependent on the refractive index values (or permittivities, equivalently) of the substrate and the metal. Thus, variations in these parameters can dramatically shift the position of the resonant minimum of the reflectance curve.

3.1 Outline of Material Modeling for SPR Simulations

The high sensitivity of the SPR sensors is provided by the strong dependence of SPR matching conditions to the electrical parameters of materials on both sides of the boundary surface. Variation in the concentration of a specific substance in the bulk medium (substrate, a solution to be tested in such a case), for instance, would change its refractive index leading to a shift in the surface plasmon resonance curve's minimum. However, the change in material concentration is not the only reason for variations in the refractive index. Wavelength scanning-based sensors operate over a frequency band so that permittivity values for all components of the sensor would fluctuate more or less as described by the Lorentz-Drude Model. Angular scanning approach or the intensity measurements are almost immune to material dispersion, i.e., permittivity variation due to frequency. As another critical concern, the temperature change can also affect the permittivity of materials and requires a careful

calibration of the SPR sensors to account for random fluctuations in ambient temperature. On the other hand, this phenomenon also paves the way for the design of SPR based temperature sensors as reported in the literature [66], [127] using a detailed permittivity model to take temperature effects into account.

Materials commonly used in SPR sensor fabrication include almost nondispersive glass such as BK7 and BAF10 for the prism, very good conductors such as gold (Au) or silver (Ag) for the metal layer, and a large variety of dielectric materials used as the sensing films and/or as the test medium (the bulk layer or the substrate as also called) that may be in solid, liquid or gaseous phase. Generally, sensor chips are designed with solid materials, while the test medium is either gaseous or liquid. Depending upon the sensing application, the test medium may be affected by material dispersion. Additional dielectric layers may also be used in SPR sensor structures to shift or sharpen the resonance dips to improve the sensor performance. Such sensing films (or sensing layers as also called) are selected according to the application's specific needs. Dielectric layers may be either dispersive or non-dispersive; they may require dispersion modeling, in general. On the other hand, metals are strongly affected by the material dispersion that has an important contribution to the sensitivity of SPR sensors.

In the subsections to follow, modeling material dispersion based on the well-known Lorentz-Drude models is discussed in the framework of SPR sensor analysis. Empirical results deduced from experimental data are also mentioned when available.

3.2 Lorentz-Drude Model for Permittivity of Metals

An atom consists of a large and heavy nucleus, and the electrons are orbiting around it. This structure is analogous to harmonic spring-mass oscillator systems where the mass is connected to a hardpoint. The mass of the nucleus is very high compared to

the mass of an electron; thus, the nucleus takes the role of infinite-mass hardpoint, and the electrons are masses of the spring-mass system.

In the early 1900s, classical physicist H. Lorentz tried to describe light-matter interaction in coherence with Maxwell Equations, and he developed the Lorentz Model using the analogy mentioned before. Lorentz used a series of differential equations originally written for spring-mass systems to build his system. He adapted the harmonic oscillator system to the electron-nucleus complex and defined a frequency-dependent function for the permittivity of materials. Permittivity, denoted by ϵ , is the measure of the polarizability of materials [143], and its unit is F/m . Lorentz Model uses the aforementioned analogy to derive the electric susceptibility, χ_e , initially, then defines the permittivity using electric susceptibility.

In metals where electrons are freely moving, Lorentz Model can be modified to a version with no restoring force (i.e., no spring), and it is called as Drude Model, or the generalization of the Lorentz model called as Lorentz-Drude Model. Thus, permittivity variations of materials (including metals) to frequency changes can be estimated theoretically with the Lorentz-Drude Model. Based on the classical theory, the Lorentz-Drude Model is adopted by quantum physics and still in use in many areas today.

According to the Lorentz-Drude Model, relative complex permittivity is defined as [46], [144]–[146]

$$\epsilon_r(\omega) = \epsilon'(\omega) + j\epsilon''(\omega) \quad (3.1)$$

The + sign of ϵ'' is selected due to time convention ($e^{j\omega t}$) used in Chapter 2. As mentioned before, Lorentz initially derived a formula for electric susceptibility, χ_e , from analogy with spring-mass system

$$\chi(\omega) = \left(\frac{Ne^2}{m_e \epsilon_0} \right) \frac{1}{\omega_0^2 - \omega^2 + j\Gamma_0 \omega} \quad (3.2)$$

where

$$\omega_p^2 = \frac{Ne^2}{e_0 m_e} \quad (3.3a)$$

$$m_e = 9.11 * 10^{-31} \text{ kg} \quad (3.3b)$$

$$e = 1.602 * 10^{-19} \text{ C} \quad (3.3c)$$

$$\epsilon_0 = 8.854187817 * 10^{-12} \text{ F/m} \quad (3.3c)$$

ω_p is the plasma frequency; m_e , and e , are the electron mass (effective mass, in some cases) and the magnitude of the electron charge, and ϵ_0 is the free permittivity of vacuum; these parameters do not depend on material properties. N is the number of electrons per unit volume and a material parameter, plasma frequency can be calculated for any material with known N . Γ_0 is the damping factor, and ω_0 is the natural resonance frequency, and all these parameters are material properties. Then, the relative permittivity function is expressed as follows in terms of electric susceptibility

$$\epsilon_r(\omega) = 1 + \chi(\omega) = 1 + \frac{\omega_p^2}{\omega_0^2 - \omega^2 + j\Gamma_0 \omega} \quad (3.4)$$

Extreme values of permittivity, the static permittivity, ϵ_s , as frequency approaches to zero and the high-frequency permittivity, ϵ_∞ , as frequency approaches to infinity can be found as

$$\epsilon_s = \epsilon(\omega \rightarrow 0) = 1 + \frac{\omega_p^2}{\omega_0^2} \quad (3.5a)$$

$$\epsilon_\infty = \epsilon(\omega \rightarrow \infty) = 1 \quad (3.5b)$$

thus, Equation 3.4 becomes

$$\epsilon_r(\omega) = \epsilon_\infty + \frac{(\epsilon_s - \epsilon_\infty)\omega_0^2}{\omega_0^2 - \omega^2 + j\Gamma_0\omega} \quad (3.6)$$

For a more realistic model, multiple oscillators can be modeled by modifying Equation 3.6 as

$$\epsilon_r(\omega) = \epsilon_\infty + \sum_{i=1}^{N_\epsilon} \frac{f_i \omega_{0i}^2}{\omega_{0i}^2 - \omega^2 + j\Gamma_i\omega} \quad (3.7)$$

Equation 3.7 gives the most general form of the model, where f_i is the oscillator strength, ω_{0i} is the natural frequency, Γ_i is the damping factor for the i^{th} Lorentz oscillator. All parameters in Equation 3.7 except ω , the angular frequency, are material parameters. The Lorentz-Drude Model will be used to model metal behavior in the sections to follow. The use of Gold (Au), Silver (Ag), Aluminium (Al), and Copper (Cu) are common in SPR studies, as reported in the literature. Therefore, these metals will be used in our SPR sensor simulations.

Equation 3.7 can be simplified for metals. As mentioned earlier, there are no bound electrons in a metal, and consequently, there is no restoring spring force in the model, which means

$$\omega_0 = 0 \quad (3.8)$$

Thus, the Lorentz-Drude Model for Metals will reduce to

$$\epsilon_{r,m}(\omega) = 1 - \frac{\omega_p^2}{\omega^2 - j\Gamma_0\omega} \quad (3.9)$$

Multiplying the numerator and denominator with $\omega^2 + j\Gamma_0\omega$ to calculate the real and imaginary parts

$$\epsilon_{r,m}(\omega) = 1 - \frac{\omega_p^2(\omega^2 + j\Gamma_0\omega)}{(\omega^2 + j\Gamma_0\omega)(\omega^2 - j\Gamma_0\omega)} \quad (3.10)$$

Reorganizing Equation 3.10

$$\epsilon_{r,m}(\omega) = 1 - \frac{\omega_p^2\omega^2 - j\omega_p^2\Gamma_0\omega}{\omega^4 + (\Gamma_0\omega)^2} \quad (3.11)$$

Separating real and imaginary parts

$$\epsilon_{r,m}'(\omega) = 1 - \frac{\omega_p^2\omega^2}{\omega^4 + (\Gamma_0\omega)^2} = 1 - \frac{\omega_p^2}{\omega^2 + \Gamma_0^2} \quad (3.12a)$$

$$\epsilon_{r,m}''(\omega) = -\frac{\omega_p^2\Gamma_0\omega}{\omega^4 + (\Gamma_0\omega)^2} = -\frac{\omega_p^2\Gamma_0}{\omega^3 + \Gamma_0^2\omega} \quad (3.12b)$$

From Equation 3.12a, it can be observed that the real part of the metal permittivity is negative when $\omega^2 + \Gamma_0^2 < \omega_p^2$. For small damping case, i.e., $\Gamma_0 \ll \omega$

$$\epsilon_{r,m}'(\omega) = 1 - \frac{\omega_p^2}{\omega^2} \quad (3.13)$$

Therefore, for $\omega < \omega_p$, the real part of the metal's permittivity becomes negative. Evaluating Equations 3.12 and 3.13, the Lorentz-Dude parameters Γ_0 and ω_p (normalized by 2π) are derived for some commonly used metals by Ordal et al., [46] as shown in Table 3.1, similar results obtained by others are available in the literature [147]–[149].

Table 3.1: Lorentz-Drude Parameters of Selected Metals

Metal	$\Gamma_0/2\pi$ (THz)	$\omega_p/2\pi$ (THz)
Au	6.45	2182
Ag	4.35	2179
Al	19.78	3622
Cu	2.2	2619

Equations 3.12a and 3.13, together with Table 3.1, prove that metal permittivity is negative sufficiently below the plasma frequency, which is satisfied in the visible range. The complex-valued refractive index of a material can also be derived using Equation 2.7, as

$$n = n' + j n'' = \sqrt{\epsilon_r} \quad (3.14)$$

3.2.1 Complex Permittivity and Refractive Index Functions of Selected Metals

Permittivity and refractive index models for metals given in Table 3.1 are created using Equations 3.12a and 3.14 and plotted in Matlab to be presented in this section. Among the others, gold is the most prevalent metal in SPR applications for its robustness against degradation, low loss, and ease of manufacturing. Gold can withstand most acids, and it is inert against biochemical materials commonly measured with SPR sensors, making it a good choice for SPR applications. Silver follows gold as the second most preferred metal. Silver is a better conductor, and its loss is lower than gold, but it is not as inert as gold. Copper and aluminium are the other metals to be modeled in this section.

As previously discussed, parameters obtained by Ordal et al. [46] and supported with practical measurements are used to obtain frequency-dependent permittivity and refractive index functions of gold. Real and imaginary parts of the complex-valued

permittivity function and the corresponding refractive index function for gold are plotted in Figure 3.1a and 3.1b, respectively, over the wavelength range from 200 nm to 1000 nm. As seen in Figure 3.1, the real part of gold permittivity is always negative for this range, and it is also larger than the imaginary part, particularly for wavelengths larger than 600 nm, satisfying the conditions on permittivity discussed in Chapter 2 in section 2.2.

Silver is a better metal in terms of performance, as mentioned above. The magnitude of the real part of its permittivity is relatively larger, and the imaginary part is smaller than that of gold, making it an even better fit for the discussion of Section 2.2. This would imply that silver might have a better sensor resolution than gold under similar design parameters. However, silver is not as durable as gold for most applications. Despite that, silver may be preferred over gold in some SPR applications due to its lower cost and better SPR curve performance as compared to gold. The permittivity function of silver is computed using the parameters given in Table 3.1 and in the articles [46], [149]. Real and imaginary parts of the resulting complex-valued permittivity function and the corresponding refractive index function are plotted in Figure 3.2a and 3.2.b, respectively, over the wavelength range from 200 nm to 1000 nm.

Aluminium is not as popular as gold and silver in SPR sensor design. Still, there is some new research showing that the use of aluminium would provide a better resonance response, particularly in UV [45], [150]–[152], and it can also be used to create multiple resonances [152], [153]. However, the use of aluminium in the design of chemical and biological SPR sensors is quite limited as it is not as inert as gold and silver. Complex permittivity and refractive index functions of aluminium are computed using the parameters reported in [46] and given in Table 3.1. Real and imaginary parts of the permittivity function and the corresponding refractive index function for aluminium are plotted in Figure 3.3a and 3.3.b, respectively, over the wavelength range from 200 nm to 1000 nm.

Aluminium has a much higher plasma frequency than gold and silver, as shown in Table 3.1, and features a higher loss, as seen in Figure 3.3, with a peak around 800 nm, which further limit the usefulness of aluminium for visible or near-IR SPR operation; however, it can be used effectively in UV.

The last metal to be considered is copper that has a higher conductivity than gold, silver, and aluminium. It is not as popular as gold or silver since it is highly prone to chemical reactions and natural degradation, similar to aluminium; however, copper's refractive index profile is similar to those of gold and silver, as shown in Figure 3.4. Thus, copper would be considered as an excellent alternative to gold and silver for specific applications where chemical interactions are not critical. Some studies in the literature have investigated the performance of copper in SPR design [153], [154]. Complex permittivity and refractive index functions of copper are computed using the parameters reported in [46] and given in Table 3.1. The permittivity function's real and imaginary parts and the corresponding refractive index function for copper are plotted in Figure 3.4a and Figure 3.4b, respectively, over the wavelength range from 200 nm to 1000 nm.

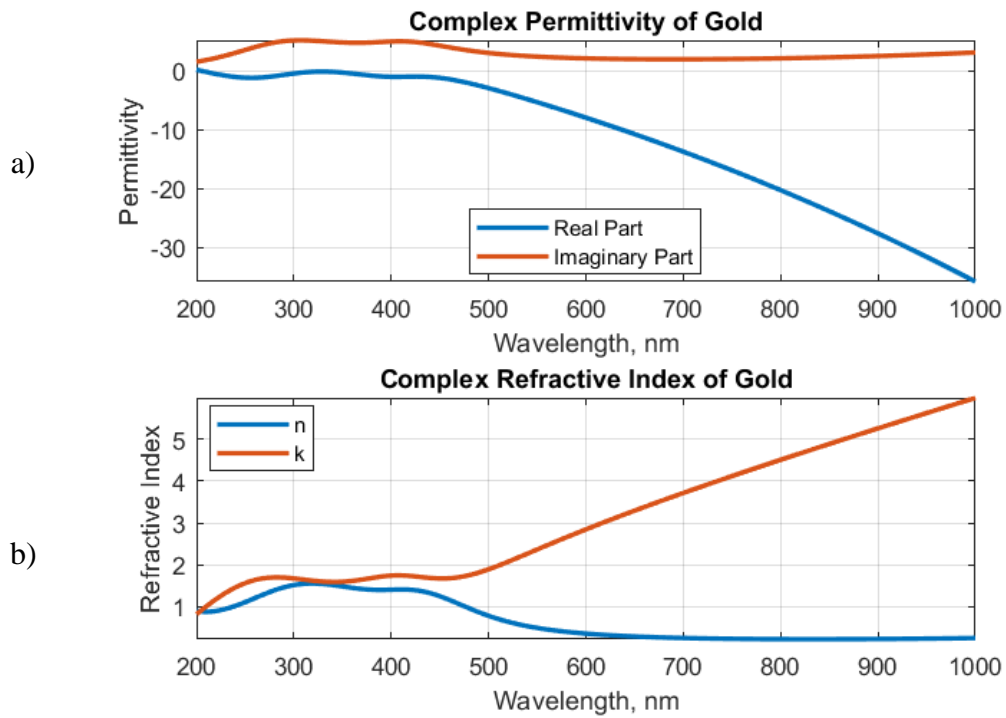


Figure 3.1: a) Complex permittivity, and b) complex refractive index of gold.

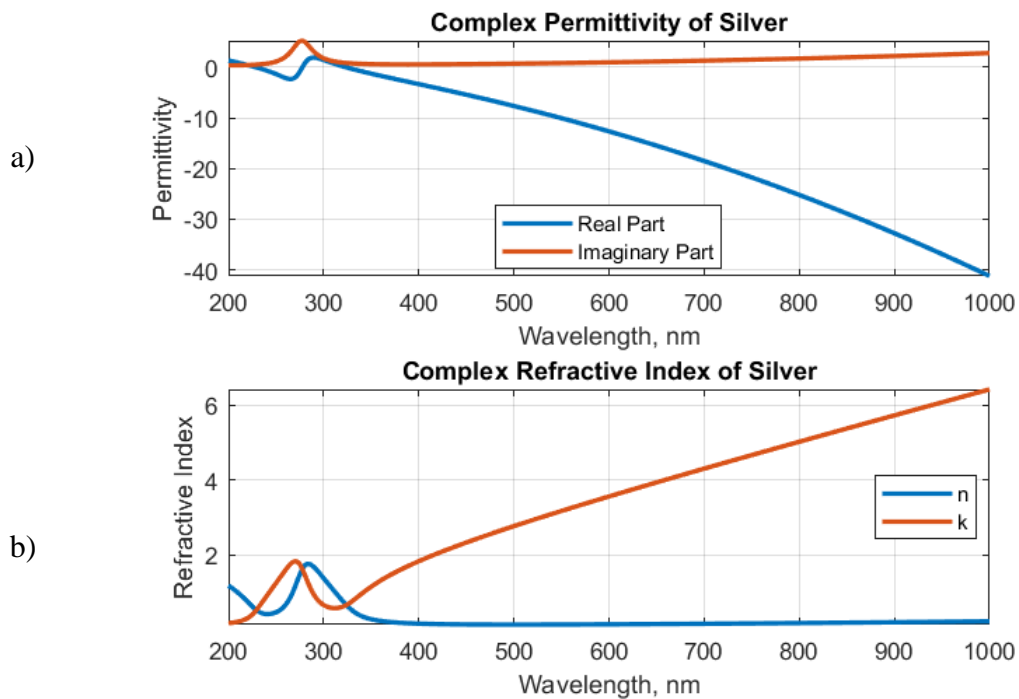


Figure 3.2: a) Complex permittivity, and b) complex refractive index of silver.

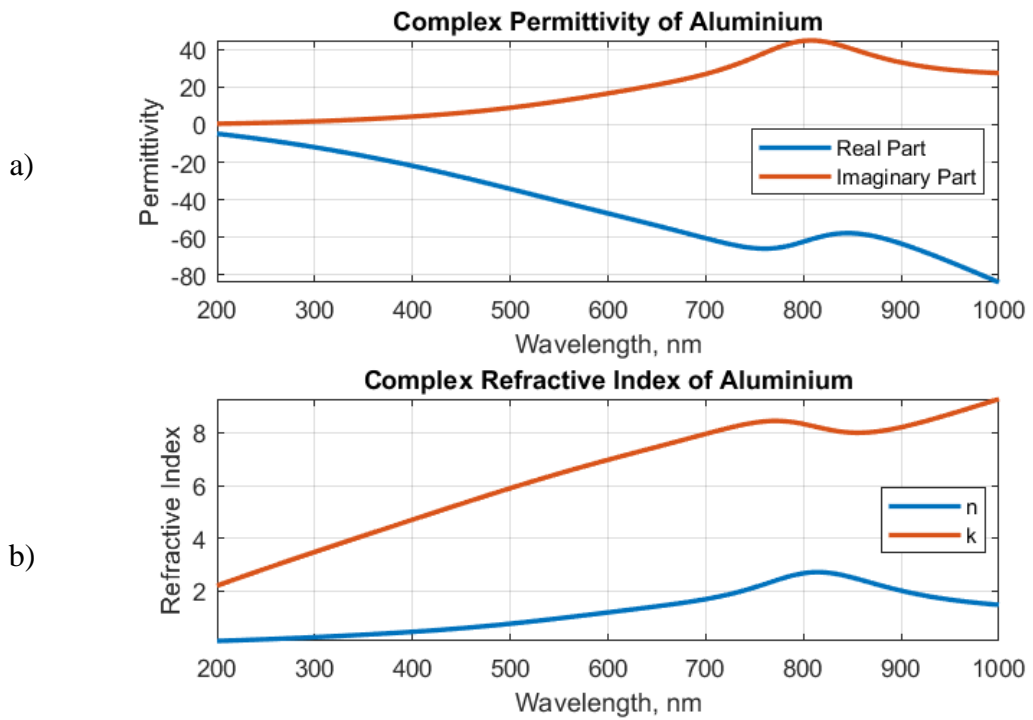


Figure 3.3: a) Complex permittivity, and b) complex refractive index of aluminium.

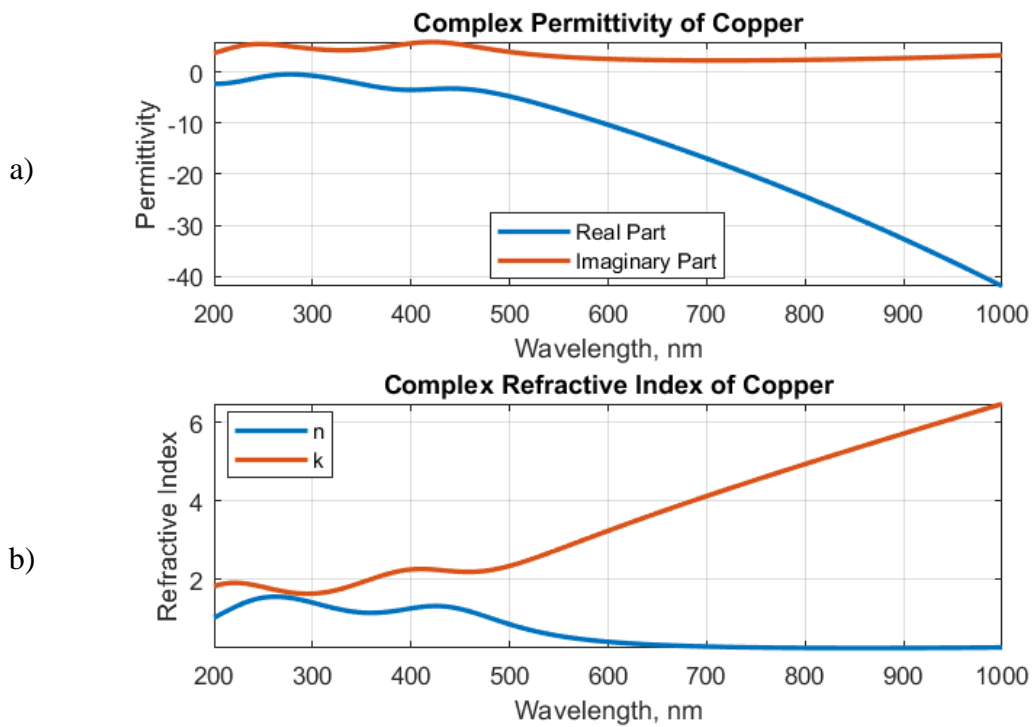


Figure 3.4: a) Complex permittivity, and b) complex refractive index of copper.

3.2.2 Concluding Remarks: Metal Selection for SPR Sensors

Metals used in SPR sensors are expected to satisfy some requirements: A metal, to have a convenient surface plasmon response, must have a low-loss spectrum in the desired operation range, which is generally visible or near-IR for SPR applications. Noble metals such as gold and silver or very good conductors like copper and aluminium are good choices for SPR simulations and generate a convenient response in the aforementioned ranges.

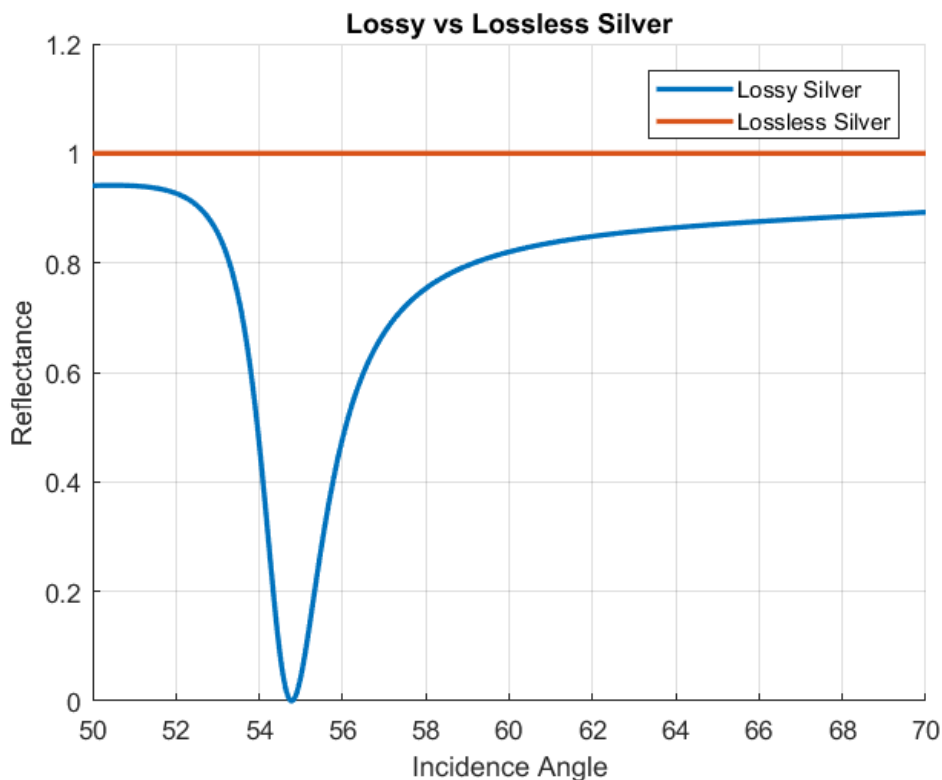


Figure 3.5: Simulated reflectance curves for an SPR sensor with lossless and lossy silver layers. The structure consists of BK7 type prism glass, silver, BAF10, and pure water ($n=1.33$, lossless) operated at 632nm. Lossless silver does not generate any resonance, while a well-developed SPR curve is observed for lossy silver.

The power losses due to the metal sections of the SPR sensor, although they are very low, should not be neglected in simulations. Surface plasmon resonance (SPR)

behavior is mainly a result of absorption. In other words, theoretically speaking, perfect conductors cannot lead to SPR minima. A lossless metal will reflect all the incident wave, does not allow any penetration; thus, the SPs cannot be excited at all. Results of a simulation are presented in Figure 3.5 to demonstrate this critical fact where an SPR sensor structure is simulated with BK7 prism, silver, and pure water (as the dielectric substrate medium) first using a permittivity function for lossy silver, then by completely neglecting metal losses.

The thickness of the metal layer in an SPR sensor is generally around 20-100 nm. The thickness of the metal should be selected to avoid problems regarding the penetration depth, and it depends on the frequency of operation. The typical thickness values indicated above are found suitable in near-IR and visible bands. Thus, metals used in SPR sensors should be easy to manufacture as planar layers within such thickness ranges.

Finally, the permittivity of metals has implications on the excitation frequency range of SPs. Equation 2.92 implies that the prism refractive index must be large enough to match k_y and free space wavenumber. In low frequencies, metals become almost-perfect conductors and $|\epsilon_m|$ becomes too large, making it unrealistic to match the real part of k_y given in Equation 2.102 with any prism. Conclusively, SPs can be excited where $|\epsilon_m|$ is small enough to satisfy matching conditions, and this can be achieved in visible and near-IR for most metals, including metals used here Au, Ag, Cu, Al, and some others such as Cr and Pt. The effects of metal selection on the performance of the SPR spectrum will be investigated in detail in Chapter 4.

3.3 Modeling of Coupling Prisms

Coupling prisms are used to match the momentum of incident light to that of surface plasmons. The use of coupling prisms and grating couplers are two common methods for light coupling in SPR sensors. The coupling condition was discussed in Section

2.2.1. Prisms satisfy the coupling condition due to their high refractive index values, while gratings make coupling possible by the diffraction of the incident wave.

The use of prisms is the most common coupling method in SPR sensors due to ease of manufacturing and higher sensitivity; on the other hand, grating couplers generally provide lower sensitivity, but they offer better miniaturization and integration [48].

Popular optical glasses such as Al_2O_3 (sapphire), BAF10, and BK7 are widely used as coupling prisms for SPR systems. They may also be used to model sensing films, as discussed in this section and in the following chapters. All three glasses are transparent in the visible spectrum, having very small extinction coefficients. For the angular scanning approach and in narrow-band tests, the permittivity of the glass can be safely assumed to be nondispersive. In the simulations, the glass prism losses are neglected, as the losses caused by the propagation of the light within the glass prism can be calibrated easily by using test measurements and have no important effect on the SPR spectrum. Besides, the extinction coefficients of optical glasses used, BAF10 and BK7, are very low, on the order of 10^{-8} and 10^{-9} , respectively. The sapphire is often assumed to have zero loss in the visible spectrum where $\omega < \omega_p$ for the common metals used in SPR sensor design.

BK7, BAF10, and Al_2O_3 will be used as coupling prisms and sensing films in the chapters to follow. Measurement data for the refractive index of BK7 glass are taken from the datasheet given in [49]. The real part of the refractive index, n , is plotted in Figure 3.6a over the bandwidth from 400 nm to 1000 nm range, showing a relatively small variation. Data on the imaginary part of the refractive index (the extinction coefficient) is available, on the other hand, at a small number of sample wavelengths as shown in Figure 3.6b over the band from 400 nm to 700 nm having very small values on the order of 10^{-8} . BAF10 is another commonly used optical glass with low loss and low dispersion. Measurement data for BAF10 optical glass are obtained from the Schott datasheet for optical glasses [49]. The refractive index

and extinction coefficient values (i.e., the real and imaginary parts of the complex-valued refractive index) are plotted in Figures 3.7a and 3.7b, respectively.

Sapphire is an optical glass widely used in various applications, including SPR sensing (as a coupling prism) due to its availability and low cost. Measurement data for the real part of the refractive index for sapphire are taken from [155] and plotted in Figure 3.8. Any plot for sapphire's extinction coefficient is not given as it takes negligibly small values, hence assumed zero.

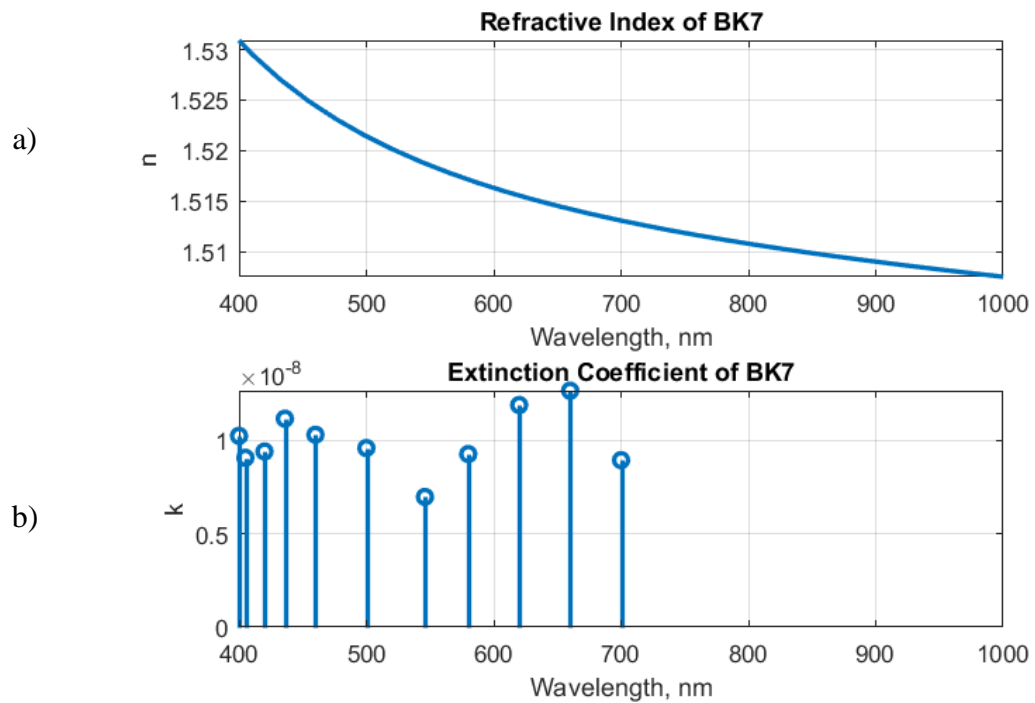


Figure 3.6: Complex Refractive Index of BK7, low values of k , and small variation of n can be observed.

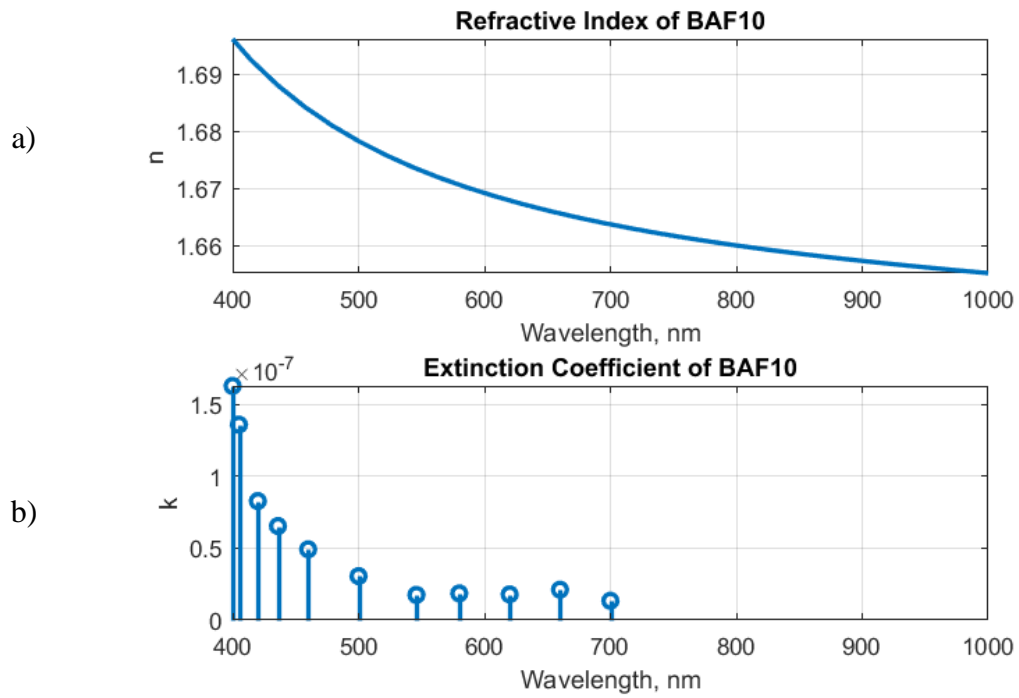


Figure 3.7: Refractive Index and Extinction Coefficient of BAF10 Optical Glass.

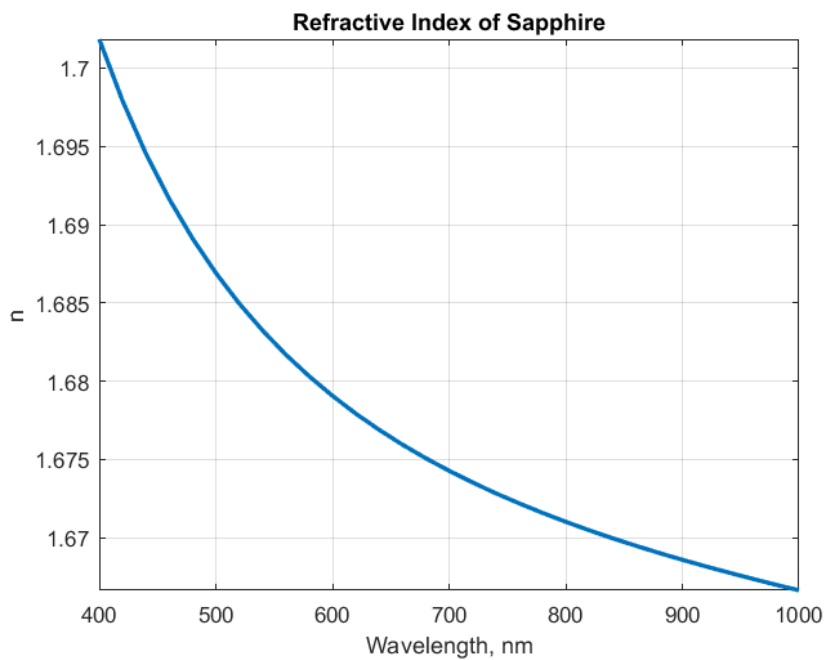


Figure 3.8: Real part of the refractive index of sapphire. The extinction coefficient for sapphire is negligibly small, assumed zero.

3.4 Modeling of the Test Material

Modeling the test material below the thin metal layer is usually more complicated. In practical applications, sensors are generally designed using a particular reference material such as water with well-known optical parameters, or the material placeholder is left initially empty, filled with air, to make it possible to collect the reference data. Then, the measurements are repeated with the material to be tested in place, and the results are calibrated using the previously recorded reference data to reconstruct the permittivity profile. In some applications, particularly in biosensing, the test material is usually found in liquid form, a solution that contains some molecules to be detected. The test material corresponds to the bottom layer (i.e., layer 3 in Figure 2.2) for a standard SPR setup. To detect the presence of an antigen in a blood sample, for instance, a layer composed of the corresponding antibody molecules can be formed at the bottom surface of the metal layer. Due to the bonding of antigen and antibody molecules, the thickness and the refractive index of this sensing layer change modifying the resonance curve characteristics of the SPR sensor. More details on such cases will be given in the chapters to follow. This section focuses on possible modeling methods for theoretical analysis.

Water is a commonly used liquid substrate for many applications. It can be used both for referencing tests and also in actual measurements. Many organisms reproduce in water. Change in water permittivity may take place in response to the presence of microorganisms or because of changes in temperature, salinity, or frequency. Such changes in the permittivity of a water-based solution can be modeled with empirical equations. In some applications (such as water quality measurements), the change in water permittivity due to the presence of microorganisms or some other harmful substances is negligible if their concentration is very low and does not change the bulk refractive index. Detection of such molecules or microorganisms is made possible by SPR sensors using specialized bonding layers; this is the primary approach in biosensor applications.

The bottom of the metal layer (or the bottom surface of another suitable and very thin layer of dielectric material put under the metal layer for binding purposes) is coated with a particular bonding material in biochemical applications to attract microorganisms in water, for instance. Such bonding layers (also called sensing layers) interact with target molecules and form a new composite layer, or a completely new layer of target molecules is assumed to be formed below the sensing layer. In both modeling approaches, suitable change in permittivity is described empirically.

3.4.1 Empirical Model for Water Permittivity

Various analytical and empirical models are available in the literature to estimate the permittivity of water. However, most of these models are useful for modeling either the permittivity of pure water or monitoring only one parameter, such as salinity or temperature of the water at a time. A smaller number of studies in literature, such as the one reported in [156], offers models for water permittivity with two or more parameters. For the performance tests to be discussed in chapters to follow, a seawater permittivity model developed by Quan and Fry [157] is used. According to this model, the refractive index of seawater under varying temperature (T), salinity (S), and wavelength (λ) parameters is formulated as

$$n(S, T, \lambda) = n_0 + (n_1 + n_2T + n_3T^2)S + n_4T^2 + \frac{n_5 + n_6S + n_7T}{\lambda} + \frac{n_8}{\lambda^2} + \frac{n_9}{\lambda^3} \quad (3.8)$$

where T is the temperature in Celcius, S is the salinity per mille, λ is the wavelength in nanometers, and n_i , $i = 0, 1, \dots, 9$ are empirically determined coefficients given as; $n_0 = 1.31405$, $n_1 = 1.779 \times 10^{-4}$, $n_2 = 1.05 \times 10^{-6}$, $n_3 = 1.6 \times 10^{-8}$, $n_4 = -2.02 \times 10^{-6}$, $n_5 = 15.868$, $n_6 = 0.001155$, $n_7 = -0.00423$, $n_8 = -4382$, $n_9 = 1.1455 \times 10^6$. The model is

designed to be valid for the temperature interval of $0^{\circ}\text{C} < T < 30^{\circ}\text{C}$, for the salinity interval of $\text{‰}0 < S < \text{‰}35$, and for the wavelength interval of $400\text{nm} < \lambda < 700\text{nm}$; however, it is found to be effective up to 1000 nm based on measurements.

This model is developed by modifying former empirical models with new measurement data. A model developed by Austin and Halikas [156], [158] is used as the starting point where Austin and Halikas do not provide a fully analytical model, but instead, they provide a set of measurement values and interpolations between the measured values, for the variations of wavelength, temperature, salinity, and the atmospheric pressure of seawater. Some examples of two-dimensional colormaps for the seawater refractive index are given in Figures 3.9, 3.10, and 3.11 for fixed salinity, fixed temperature, and fixed wavelength cases, respectively.

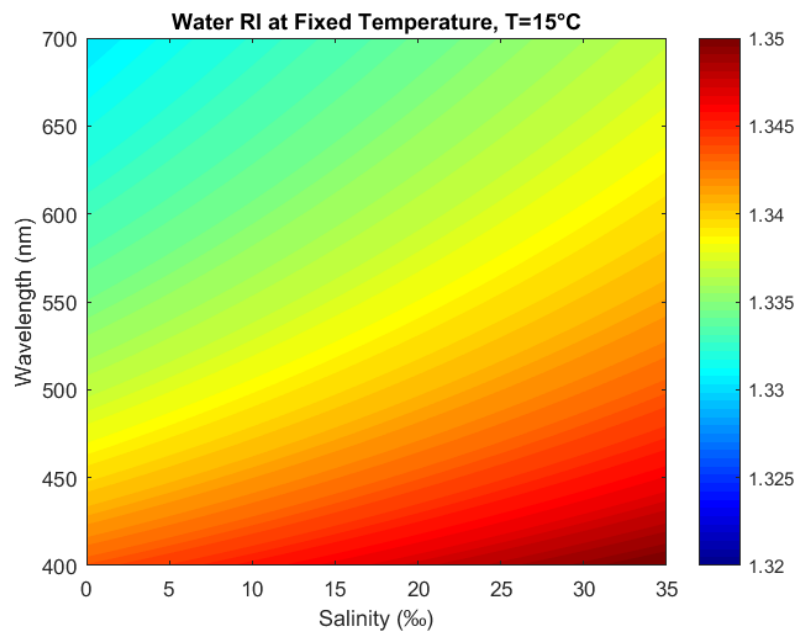


Figure 3.9: Refractive index of water calculated by Equation 3.8 at a fixed temperature of $T = 25^{\circ}\text{C}$, over the ranges $\text{‰}0 < S < 35\text{‰}$, and $400\text{nm} < \lambda < 700\text{nm}$.

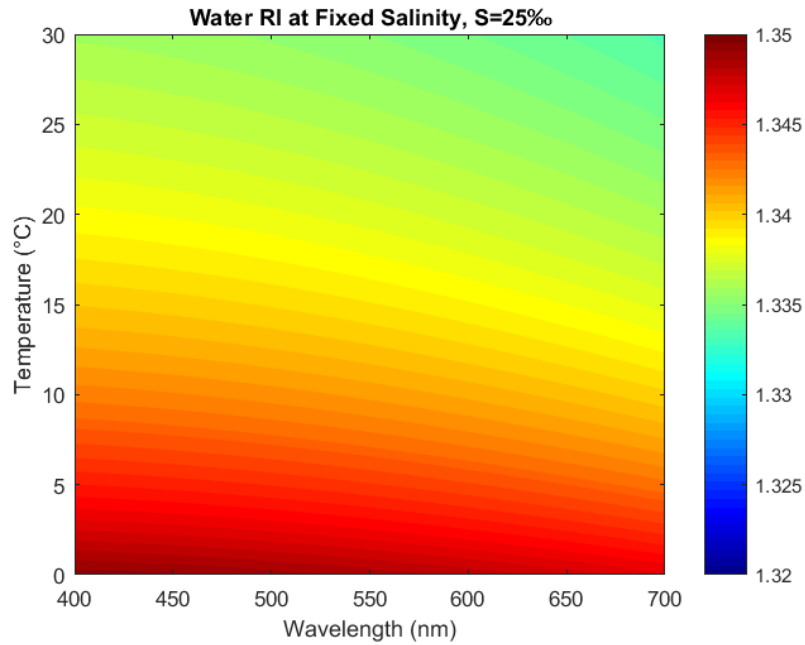


Figure 3.10: Refractive index of water calculated by Equation 3.8 at a fixed salinity level of $S = 25\text{‰}$ over the ranges $0^{\circ}\text{C} < T < 30^{\circ}\text{C}$, and $400\text{nm} < \lambda < 700\text{nm}$.

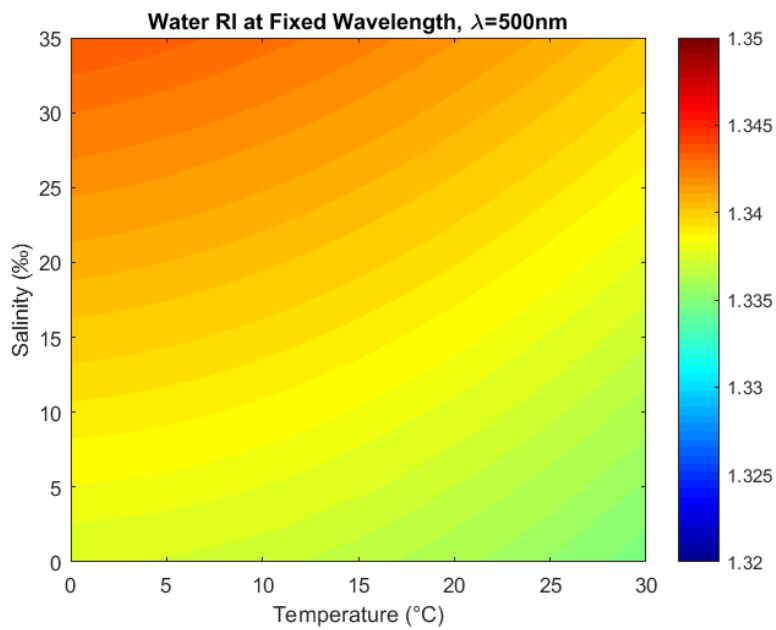


Figure 3.11: Refractive index of water calculated by Equation 3.8 at a fixed wavelength of $\lambda = 500\text{nm}$ over the ranges $0^{\circ}\text{C} < T < 30^{\circ}\text{C}$, and $0\text{‰} < S < 35\text{‰}$.

There are some other models in literature estimating the refractive index of water for wider ranges [59], [159], [160], or for more parameters and different conditions [159]–[163]. However, this model is preferred for its accuracy and for the fact that it provides a convenient polynomial form for estimations.

The imaginary part of the refractive index of seawater, i.e., the extinction coefficient, is neglected in the same way as we did for the coupling prism glasses. Absorption of water is very low in visible frequencies, particularly in the mid-region of the visible spectrum, where the extinction coefficient of water is smaller than 10^{-8} . Some studies in literature measuring the absorption spectrum of saline water reported negligibly small values confirming the assumption made [164], [165].

3.4.2 Biological Test Material Modeling

Empirical formulas or large-scale analytical models are not available for most biomolecules of concern. Although some models for electromagnetic properties of various tissue or molecules are available in the literature, most of those models are not detailed enough to be employed for SPR analysis. Measurements and models given for optical parameters of biomolecules in [166] are found useful to be used in this thesis.

To begin with, the primary purpose of biosensing is to detect the existence of a particular molecule in a complex substrate, such as detecting a particular pathogen in tap water. Measuring the electromagnetic parameters such as the refractive index or permittivity may not be conclusive for detection, especially when the concentration of target molecules in the test solution is too low to create a meaningful change in the refractive index of the substrate solution. Therefore, the formation of a special sensing layer becomes necessary in SPR sensor design to attract the target molecules in the solution. For this purpose, the sensor surface is covered with a bonding layer material comprised of some suitable biomolecules, in general. Most

of the time, this sensing layer is not a perfectly-planar layer but has surface roughness. When the bonding of target molecules to this sensing layer is completed, either a new layer of target molecules is formed below the bonding layer; or the bonding layer and the attracted molecules are unified to form a new composite layer. The new layers formed with attached molecules generally exhibit irregularities also as the target molecules have various shapes, and attachment with the bonding layer is irregular in most applications.

The irregularities generally are unavoidable, and various correction methods and experimental approaches are employed for improved estimations. Test measurements are usually repeated for different concentrations of target molecules to determine the variation of the refractive index as a function of concentration to establish a useful empirical model.

The subsections to follow will outline the basics of two different SPR sensor studies reported in the literature for bio-molecule measurements and the sensing layer models used.

3.4.2.1 Model 1: Unified Layer

The first model is taken from Akimoto et al., [167], where the researchers designed an SPR sensor based on the wavelength interrogation method. They also performed sensor analysis at various incidence/reflection angles to optimize the sensitivity of the sensor with respect to the observation angle. The sensor is designed to detect bovine serum albumin (BSA) proteins (the target molecules) in a test solution of phosphate-buffered saline (PBS) that also contains Tween 20 molecules as a detergent to wash the molecules nonspecifically binding to the sensor surface (i.e., other molecules except BSA, bonding due to physical, not chemical, bonds). A special bonding layer is designed to attach the BSA proteins to the sensor surface. The bonding layer-BSA protein complex is investigated as a single unified layer after

bonding. The increase in layer thickness and the change in refractive index are studied for varying concentration levels. The main reason to include this model in this thesis is that a comprehensive analysis of the bonding-protein layer's refractive index is provided, and detailed explanations for the fabrication process and the experimental procedures are given in [167].

The sensor is fabricated using a 54 nm thick metal layer and a BK7 type coupling prism. The metal layer consists of a chromium layer with 2 nm thickness, which performs as a chemical matching layer, followed by a gold layer with 52 nm thickness. However, as the chromium layer is extremely thin, it has been reported that it does not affect the resonance behavior, as researchers observed. Then, the metal layer is assumed to be a 54 nm thick single gold layer without any loss of accuracy. The third layer is the newly formed protein bonding layer, followed by the fourth layer, which is the liquid substrate comprised of the test solution. A wavelength scanning method is applied with two different incidence angles, 68° , and 76° .

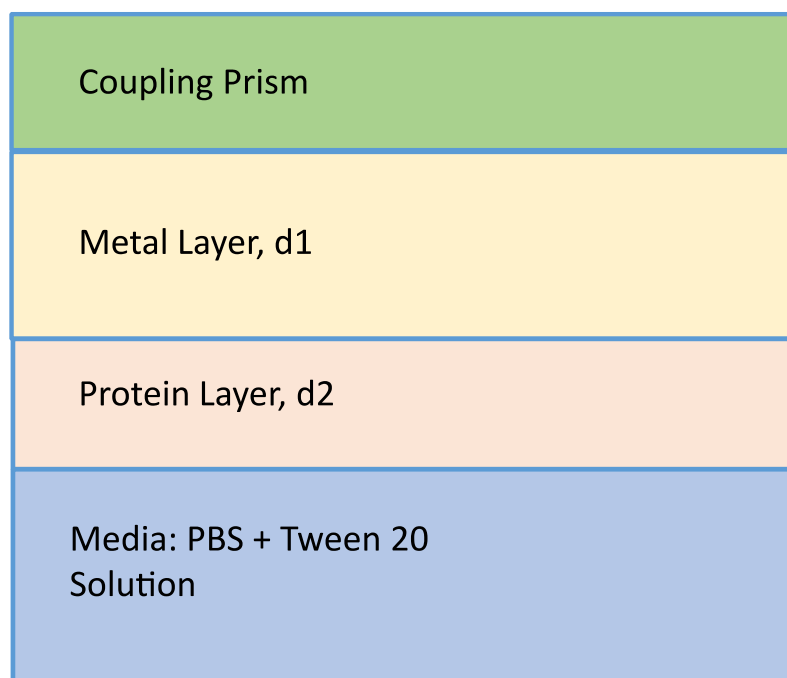


Figure 3.12: Four-layer system produced after binding proteins to the sensing layer.

A multistep bonding and cleaning procedure is applied to the sensor surface to attach only the target molecules. In the final state, the structure given in Figure 3.12 is formed. The refractive index of PBS + Tween 20 solution is measured as 1.334 at 589 nm and as 1.330 at 700 nm. The dispersion of the refractive index of the media is then assumed to be 0.004 RIU for a change of 100 nm linearly.

Two different models are used to define the properties of the protein layer. In the first model, the thickness of the protein layer is assumed to have a constant value, independent of concentration, and only the refractive index changes are taken into account. The second model assumes a constant refractive index and a varying layer thickness. The first model was found to be more accurate when compared with the results reported in the literature. The results for the change in refractive index in response to the changes in concentration are given in Figure 3.13.

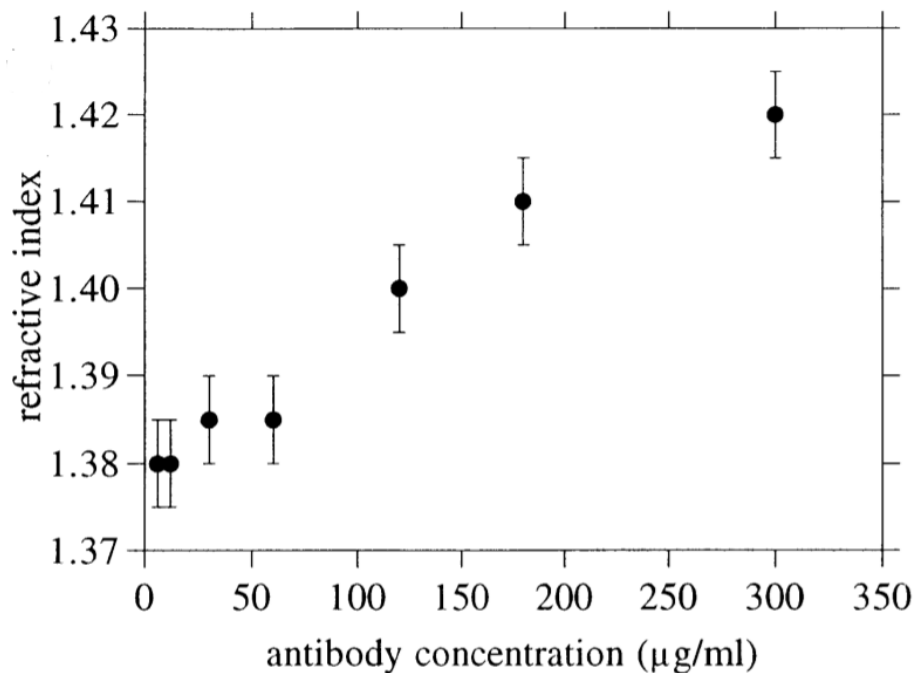


Figure 3.13: Change of refractive index with the antibody concentration of the test solution. The thickness of the protein layer is assumed to be constant at 14 nm for all concentrations. The figure is taken from the original article [167].

3.4.2.2 Model 2: New Layer Under Bonding Layer

The article by Chen et al. [168] provides the basics for the second model, where it is assumed that a new layer is formed as a result of the binding of target molecules to a sensing layer in a five-layer SPR system. The sensor is designed to analyze the effects of antibody orientations on the sensor surface after bonding of protein G molecules and fabricated with a microscopic glass with $n=1.5151$ as coupling prism, attached to a gold layer of 49 nm thickness. The Prolinker immobilizer is used to immobilize proteins on the sensor surface. The thickness of the Prolinker is 1.19 nm, while its complex refractive index is characterized by $n=1.350$ and $k=0.2$. Antibodies are attached to the Prolinker, forming a layer with a thickness of 13.8nm and a complex refractive index of $n=1.383$ and $k=0.0095$.

The SPR sensor structure defined in this article is preferred due to its similarity with the previous model (same measurand), which makes comparisons of two models easier and meaningful. The final 5-layer SPR structure (after immobilization) is given in Figure 3.14. For this SPR sensor, the measurements are performed at 675 nm with angular scanning. PBS is used as the liquid test media containing antibodies, as in the previous case.

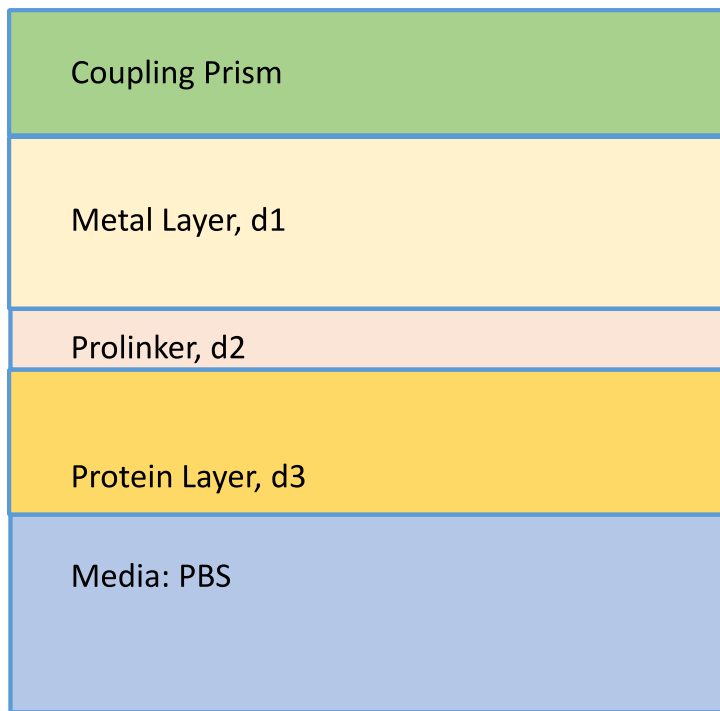


Figure 3.14: 5-layer system with a new layer formed below the Prolinker sensing layer.

CHAPTER 4

EFFECTS OF METAL SELECTION ON SENSOR PERFORMANCE

The selection of metal type is critical for SPR applications. Only a few different metals can create surface plasmon (SP) waves in a useful frequency range. Gold and silver are the most widely used metals in literature. In this chapter, the performances of four selected metals, gold (Au), silver (Ag), copper (Cu), and aluminium (Al), are investigated in a given SPR configuration. The optical parameters of these metals are already presented in Chapter 3.

The conditions to excite an SP wave at a boundary in a multilayered structure are discussed in Chapter 2. As Equation 2.86 implies, the real part of the permittivity of one of the materials must be negative. Its magnitude must be larger than the real part of the permittivity of the dielectric material on the other side of the boundary. Since the real parts of the permittivities of natural dielectrics are positive, this condition can be satisfied by metals below the plasma frequency. In SPR applications, only a few metals have suitable permittivity values to satisfy this condition in the visible or IR spectrum. In addition to the constraints on the real parts of permittivity, loss properties of metals are also essential to estimate the proper thickness of the metal layer: low-loss metals are preferred in SPR sensor design to improve the sensor performance as their resonance lines are sharper and to simplify the fabrication process. Also, metals in SPR design must be chemically stable as the SPR sensors are generally designed to be reusable.

Alternatives such as using bimetallic structures and impurities in different metallic bodies have also been investigated in literature in recent years [51], [79], [85], [131], [169]. Although such modifications increase the sensor's performance, they complicate the fabrication procedures. In this chapter, metals' performance will be

analyzed only for a conventional, multilayered system with uniform layers. CST Studio Suite and Matlab will be used in analytical and numerical SPR sensor simulations, respectively.

4.1 Analysis Method

The use of different types of metals in a given SPR topology are simulated using analytical formulations and numerical simulations. Derivations of formulas for the reflectance of multilayer structures are presented in detail in Chapter 2 and will be used here to obtain the reflectance of a multilayered system as a function of wavelength and reflection/incidence angle. 2D contour plots have been generated using the resulting reflectance function over the two-dimensional domain of wavelength and angle of reflection to visualize the overall variation of the reflectance pattern from the perspectives of both wavelength scanning and angular scanning simultaneously. These computations and 2D colormap plot generations are realized conveniently in the Matlab R2017a platform. The SPR sensor structures already analyzed by the analytical approach are also simulated numerically using the full-wave electromagnetic solver, CST Studio Suite 2018. The numerical simulations are not only useful to double-check the accuracy of analytical results, but they can also provide solutions for particular SPR topologies that are too complicated to be analyzed analytically.

The optical parameters of the common materials used in SPR design are already discussed in Chapter 3, which are used to model the frequency-dependent optical behaviors of the SPR materials in this chapter. Analytical calculations and numerical simulations of the SPR reflectance curves are obtained, and the results are plotted accordingly by both analysis approaches.

The analyses are conducted over the interval from 600 nm to 1000 nm in wavelength with 0.1 nm sampling steps, while the angular interval is sampled from 35° to 70° by 0.003° angular steps.

4.1.1 Materials and Dimensions of Structure

The basic SPR topology used in the simulations of this chapter is originally described in [66]. This structure has been modified using similar SPR design examples available in the literature [37], [50], [134], [170]–[174]. Sapphire (Al_2O_3) is used for the coupling prism for all cases, with parameters presented in Chapter 3. Losses of the Sapphire prism are neglected, as discussed earlier. Another glass, BAF10, is used as a sensing film. The thickness of the sensing film is assumed to be 100 nm, and the metal thickness is taken to be 50 nm in all cases, with only one exception: When Al is used in the metal layer, the thicknesses of the sensing film and the metal layer need to be reduced to 50 nm and 20 nm, respectively, to effectively excite the SPs.

Water is used as the main substrate in all simulations, and it is modeled with minimal dispersion since its refractive index is changing very slowly (almost constant) in the wavelength range of simulation [159], [160]. The previously derived water permittivity model was used to check results, and no significant differences were observed. Loss of water is also neglected, as explained in Chapter 3 since the substrate thickness is assumed to be infinite (i.e., no reflections come back to the structure from the water layer). Briefly, the sensor is designed with an Al_2O_3 prism, a metal layer described by the Lorentz-Drude model, the BAF10 sensing film, and a substrate layer of water, as shown in Figure 4.1.

4.1.2 Properties and Parameters of CST Studio Suite Simulations

After the analytical simulations, the same SPR sensor structures are also simulated numerically using the full-wave electromagnetic solver, the CST Studio Suite 2018.

CST outputs are found helpful not only to verify the accuracy of analytical results, which are based on some simplifying assumptions but also useful to simulate the sensor behavior, especially for non-standard sensor topologies with multi-sectional sensing layers for which the analytical approach would be too complicated.

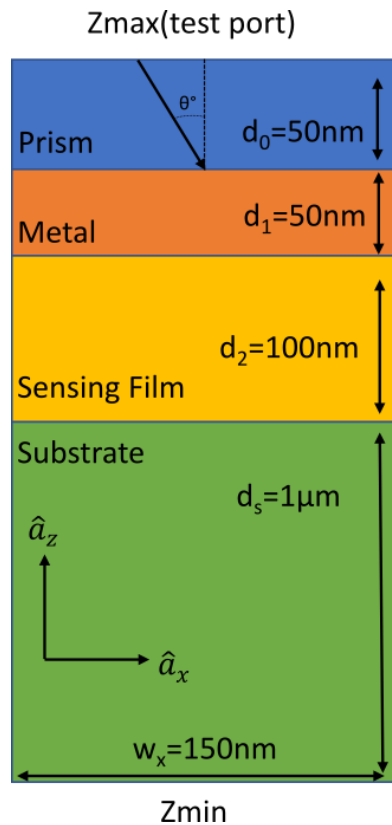


Figure 4.1: Semi-infinite, four-layer SPR sensor topology modeled in CST.

The Unit Cell (UC) module of the CST is used to simulate the multilayered sensor structure shown in Figure 4.1. The UC boundary conditions help to create a semi-infinite two-port system that is infinitely large in xy -plane (due to periodic repetitions of the unit cell) and finite along the z -direction between the test ports. The overall width along the z -direction is equal to 1200 nanometers that is the sum of the thicknesses of four consecutive sensor layers. A single cell is drawn in the workspace of CST Studio Suite, and the UC module mirrors the structure on the xy -plane, as described in Figure 4.2. Each of the red-bordered gray boxes corresponds to one unit

cell whose geometry is given in Figure 4.1. Note that the coordinate axes used here are a rotated version of what we used in Chapter 2 but the reflectivity function computed is independent of this rotation in the axes.

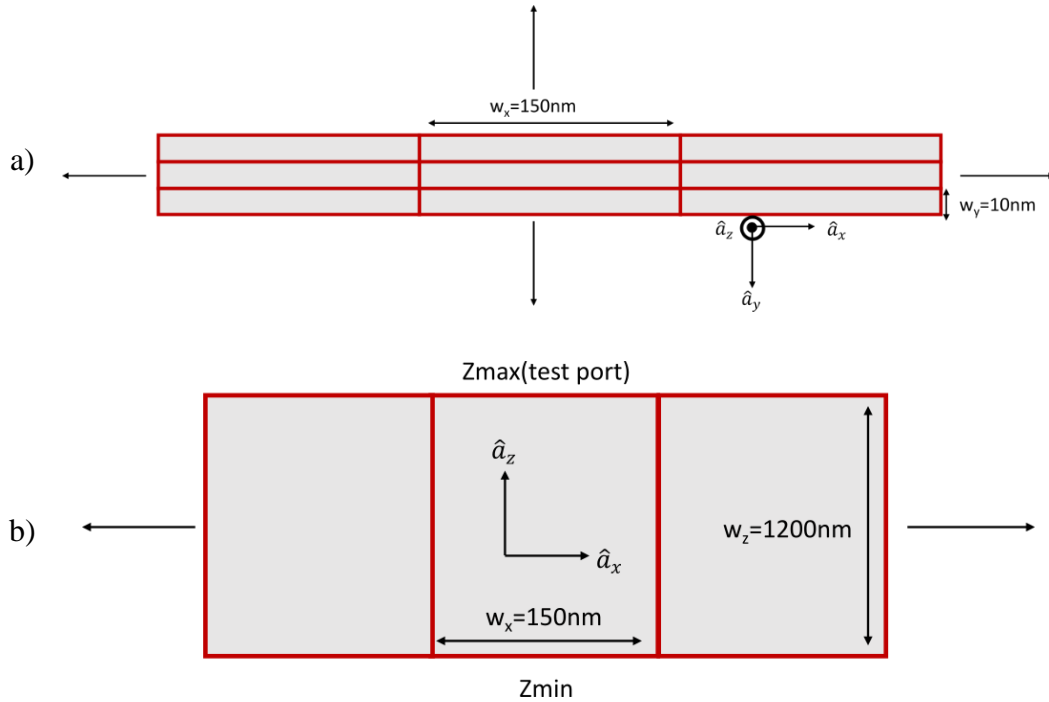


Figure 4.2: The periodic sensor structure simulated by the Unit Cell module of the CST Studio Suite, where each identical cell is described in Figure 4.1. The structure seen from a) the xy-plane, and from b) the xz-plane.

In CST simulations, two test ports are placed at the opposite ends of the exemplary cell along the z-axis. The sensor can be excited by plane waves with s-polarization or p-polarization separately (coded “1” and “2”), and with an angle of incidence on xz- and yz- planes (named θ and ϕ). In general, the scattering parameters (S-parameters) are generated at both ports. The reflectance spectrum is calculated by using the built-in macros of CST during post-processing. Finally, path loss and phase difference caused by the thickness of the prism are calibrated within the CST by eliminating their effect in the zmax port at which the overall reflection coefficient of the SPR sensor needs to be computed.

In CST, the SPR sensor structure is simulated over a desired frequency range at a selected angle of incidence (θ) that is set as a parameter, and a parameter scan in θ is performed with 0.1° angular steps. The frequency range for simulations is adjusted to scan the wavelength range from 600 nm to 1000 nm (with sampling steps of 0.04 nm) for the sensors with Au, Si, and Cu; and from 900 nm to 1600 nm (with the sampling step of 0.07 nm) with Al as to be discussed in the next subsection.

4.2 Results

Analytical and numerical simulations of the reference SPR sensor defined in the previous section are obtained with four different metals (Au, Ag, Cu, Al), which are modeled with Lorentz-Drude Model. Other parameters except the metal type are kept the same in all of the simulations. Surface Plasmon Reflectance Functions (SPRF) in each metal case are calculated and compared for metal performance. The SPRF plots are drawn as contour plots over the 2-dimensional wavelength and incidence angle domain to visualize the potential sensitivities of wavelength interrogation and angular interrogation methods. Analytical and numerical simulation results for the SPRF for the use of Au, Ag, Cu, and Al are given in Figures 4.3, 4.4, 4.5, and 4.6, respectively. Analytical simulation results are given in parts (a) of these figures, while the numerical CST simulation results are reported in parts (b).

Numerical simulation results given in Figures 4.3b, 4.4b, 4.5b, and 4.6b contain, in their lower left corners, very thin low-reflectance lines, which are possibly caused by some sort of modeling or simulation errors that have no physical importance. The rest of the numerical results shown in these figures are found in good agreement with the analytical SPRF plotted in Figures 4.3a, 4.4a, 4.5a, and 4.6a for the gold-based, silver-based, copper-based, and aluminium-based SPR sensors, respectively.

Resonant dips for these reflectance functions can be observed in the form of a deep “valley” in contour plots. For simplicity, these curves will be called resonant valleys from now on. A thinner resonant valley generally means a sharper resonant dip. At first glance, it can be observed that the shape of the resonant valleys of Au, Ag, and Cu resembles the $y = 1/x$ with ($x > 0$) equation; this reflectance variation gives a hint that these SPR sensors can be operated with both angular and wavelength scanning as all three metals have areas that they work effectively for both of these interrogation methods. The only visible difference is the slightly wider resonant valley of the Au-based sensor; this can be attributed to a slightly higher loss of Au as compared to Ag and Cu. All the results presented in Figures 4.3 through 4.6 are in agreement with the derivations/discussions of Chapter 3 and with the results reported in the SPR literature.

The reflectance curve of the SPR sensor with Al has a different behavior as compared to the use of other metals, featuring a highly flat valley indicating a lower sensitivity for wavelength scanning applications. While its resonant dip is exceptionally sharp, it is almost constant for all possible wavelength values in the design range, making it useless for wavelength scanning. Results of Al are given in 40° to 60° interval to make its sharp resonant valley visible.

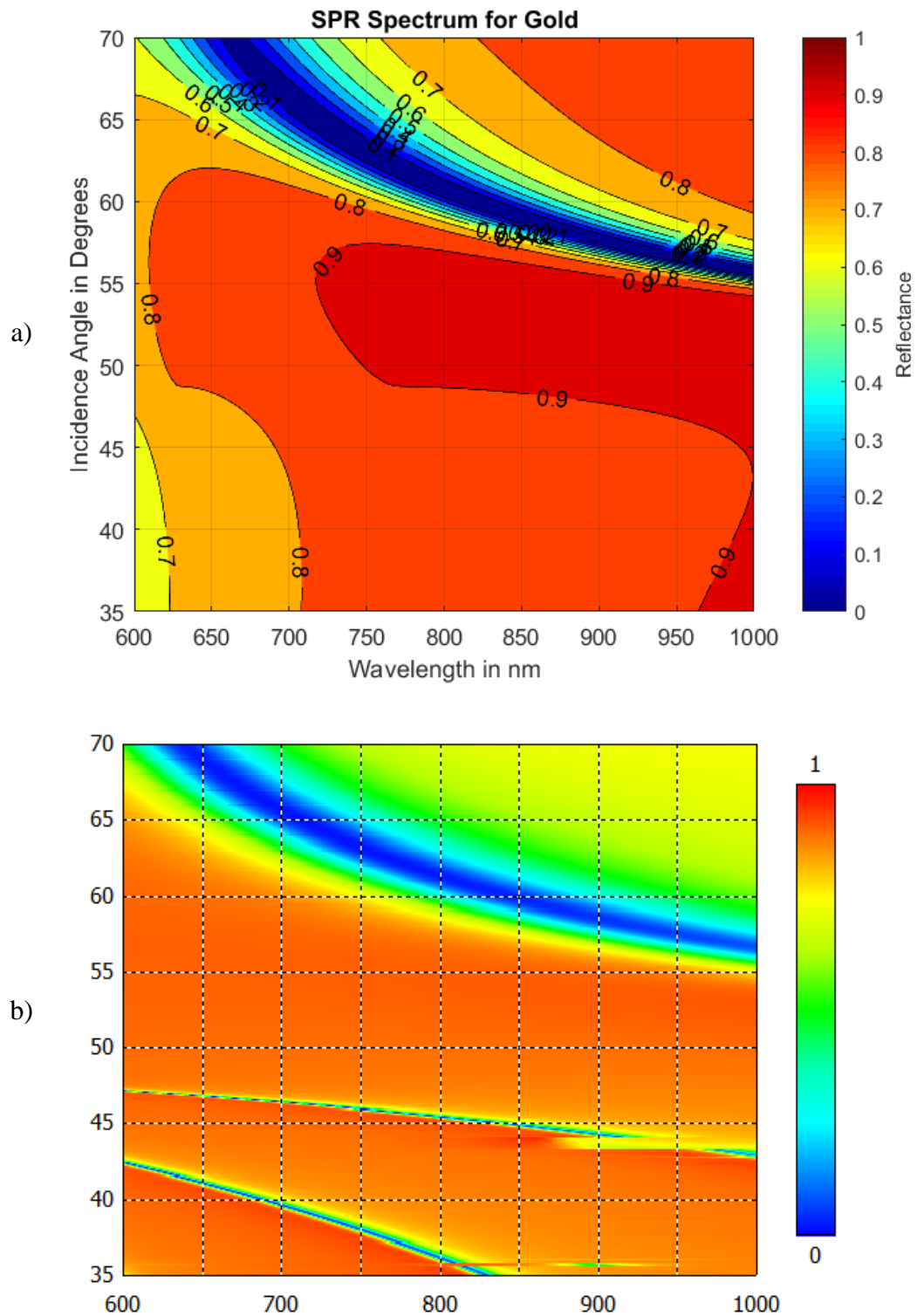


Figure 4.3: Simulation results for Au; a) Analytical simulation results with Matlab, b) Numerical simulation results with CST Studio Suite.

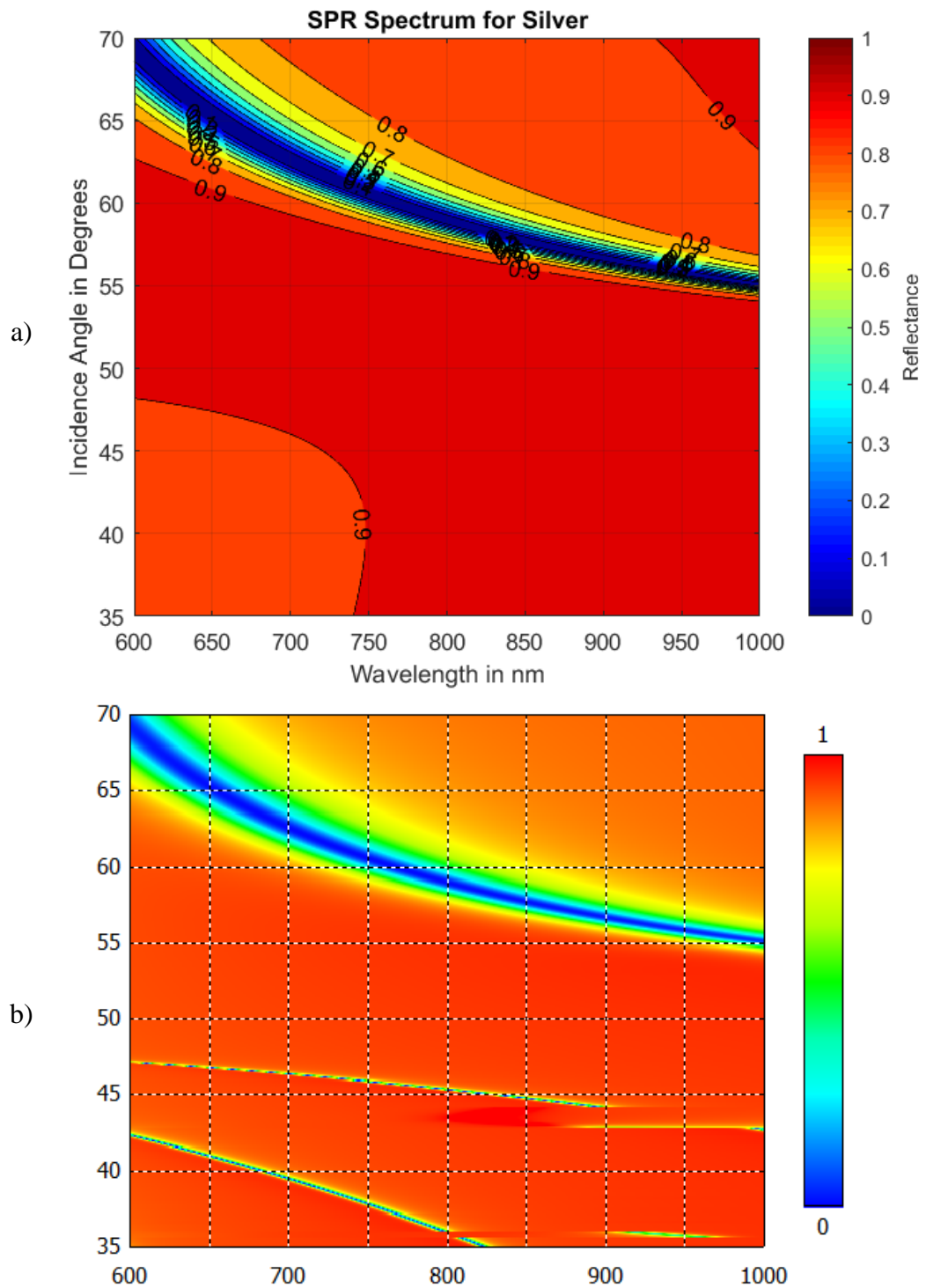


Figure 4.4: Simulation results for Ag; a) Analytical simulations results with Matlab, b) Numerical simulation results with CST Studio Suite.

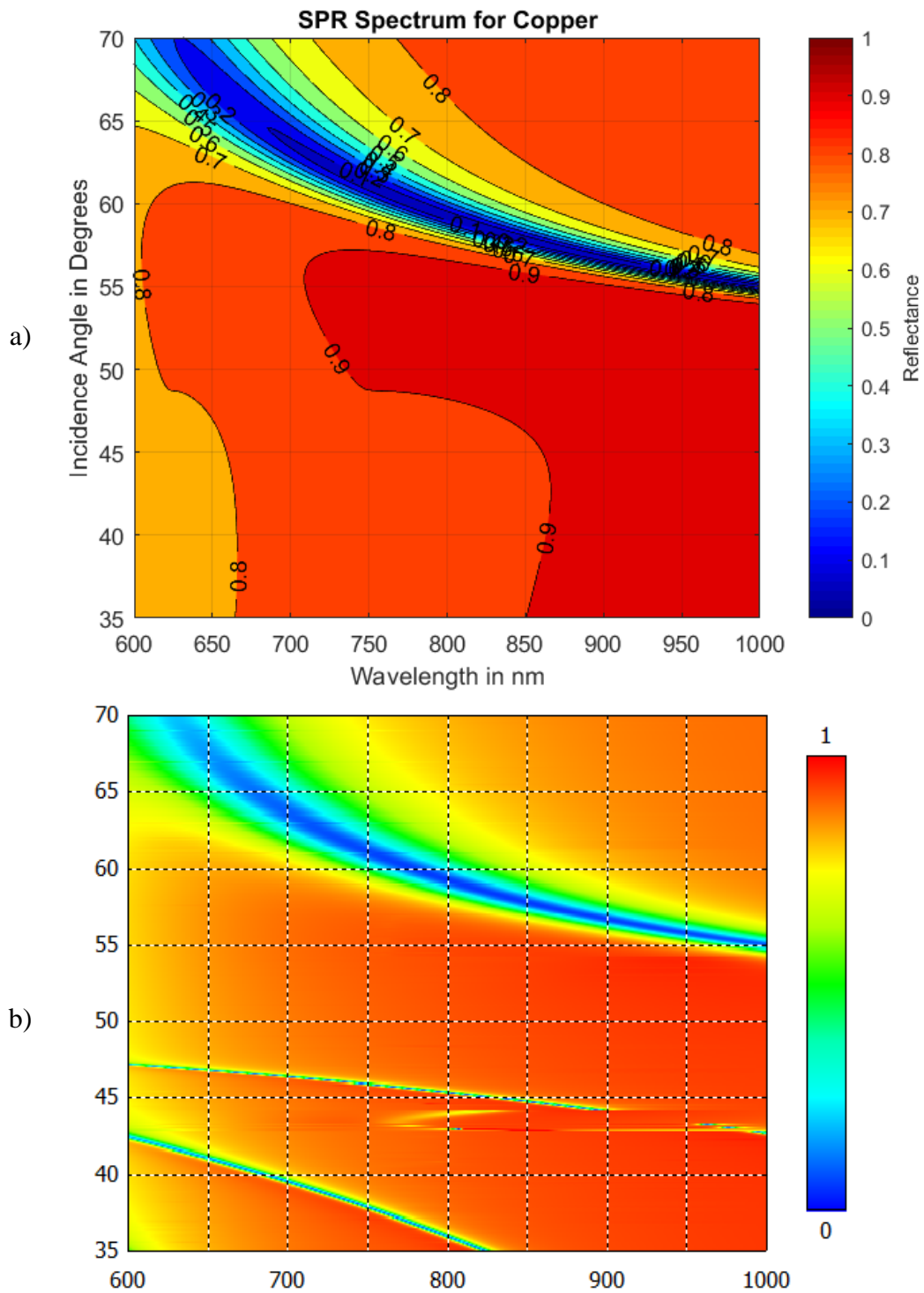


Figure 4.5: Simulation results for Cu; a) Analytical simulations results with Matlab, b) Numerical simulation results with CST Studio Suite

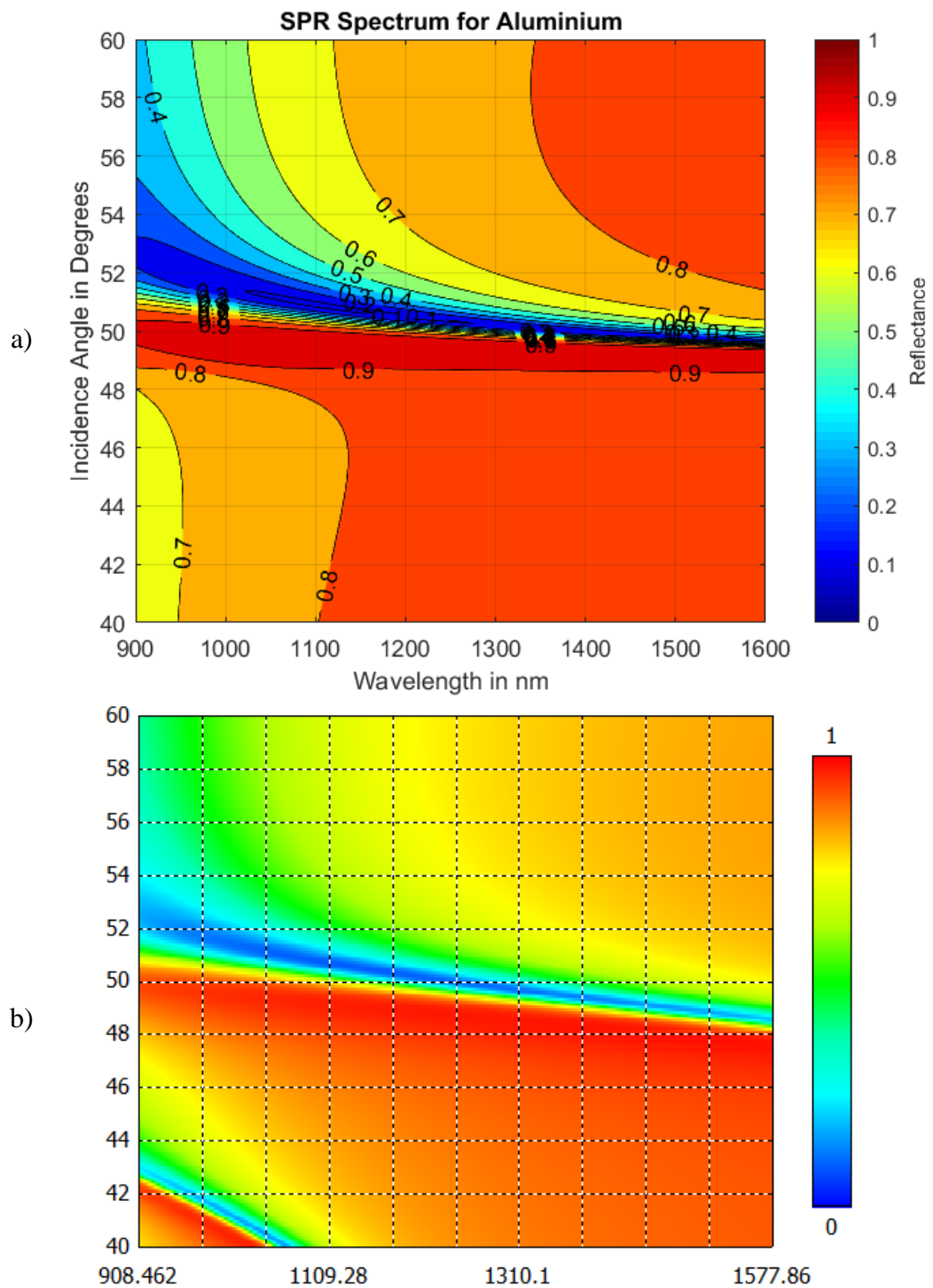


Figure 4.6: Simulation results for Al; a) Analytical simulations results with Matlab, b) Numerical simulation results with CST Studio Suite

In conclusion, the sharper reflectance resonant valleys of Ag-based and Cu-based SPR sensors, as compared to the Au-based SPR sensor, are expected from the permittivity profiles discussed in Chapter 3. The difference in the performance of Al is due to its high loss and different operational range; Al cannot be excited efficiently within the 600-1000 nm range, unlike the other three metals. As discussed previously, Al found to be more effective for the UV range in plasmonic applications; however, this chapter focuses on analyzing metal performance in visible or Near IR, and comparisons will be made for this range in the next section.

4.3 Conclusions on Metal Selection

Gold and silver are highly preferred metals in SPR sensor design, and the results are given in section 4.2 support this trend. Gold has the additional advantage of being a noble metal. Copper also has a similar performance with gold and silver, but it is much more prone to chemical reactions that reduce its usability in biochemical sensors. While aluminium provides a much sharper resonance curve along the angular axis, its flat shape shown in Figure 4.6 indicates a lower resolution with a wider resonance curve along the wavelength axis. In other words, Figure 4.6 tells us that the use of Al in an SPR sensor requires the use of an angular interrogation approach.

The performance of the SPR sensor with different metals can be quantitatively analyzed using Equation 2.103 to justify the preference of Gold and Silver in SPR literature. The sensitivity of an SPR sensor is estimated by using Equation 2.103 that is borrowed from [106]. As discussed in Chapter 2, the sensitivity formula has for multiplicative factor where the factor C is directly related to the permittivity function of the metal layer. Factor C is given as

$$C = \frac{\epsilon_m'' n^3}{2(\epsilon_m')^2} = \sigma_{RI,metal} \quad (4.1)$$

where ϵ'_m and ϵ''_m are real and imaginary parts of metal permittivity, while n is the refractive index of dielectric next to the metal layer such that the SPs are excited on this metal/dielectric interface. Keeping the dielectric medium the same (i.e., n is kept the same) under different choices for the metals, the resolution of the sensor $\sigma_{RI,metal}$ becomes proportional to the term

$$\frac{\epsilon''_m}{(\epsilon'_m)^2} \quad (4.2)$$

For a better sensor resolution, the metal used in SPR sensing applications must have a larger real part and/or a smaller loss, as also discussed during the derivations given in Section 2.2 of Chapter 2. Although the perfect (lossless) metal case seems to provide zero resolution (i.e., infinitely high sensitivity) according to Equation 2.103, it was already discussed in Chapter 3 that in the presence of a perfect conductor (theoretically), the surface plasmon waves can not be excited in the SPR sensor structure. Wavelength-dependent plots obtained by Equation 4.2 for the metals Au, Ag, Cu, and Al are given in Figure 4.7 with the accompanying discussions.

The optical properties of materials used in Figure 4.7 (and in the rest of the plots in this chapter) have been determined by using the Lorentz-Drude model, as explained in Chapter 3. Silver achieves the highest possible resolution within the four metals investigated, while gold and copper depict a similar performance where copper leads to a slightly better resolution.

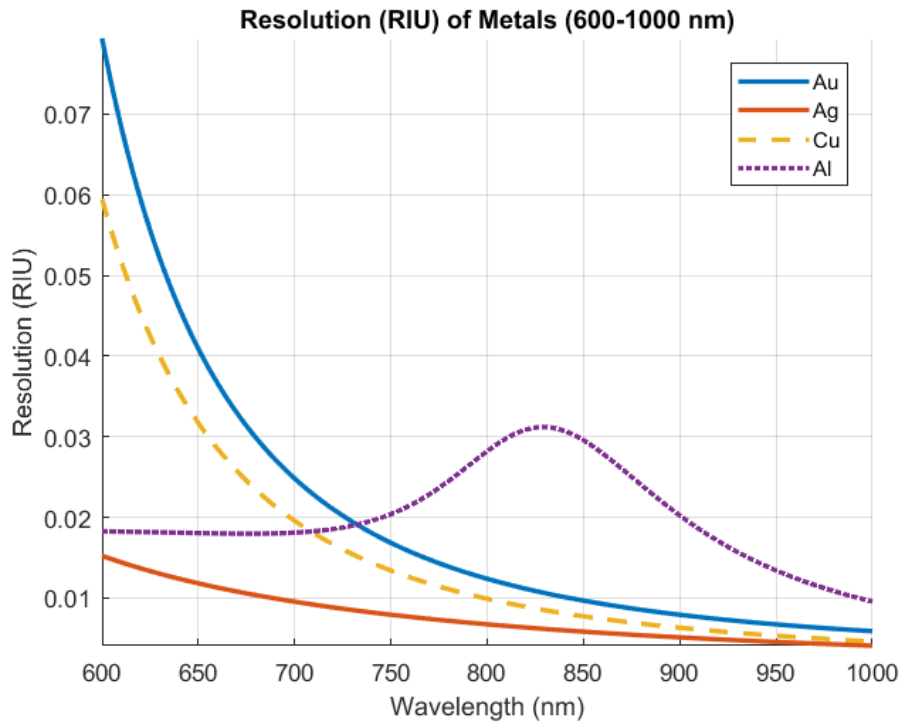


Figure 4.7: Resolution (in RIU) of selected metals ($\sigma_{RI,metal}$) for 600-1000 nm.

Aluminium has been observed to have a better performance in the visible range, as it has been partly discussed in the previous section. However, aluminium cannot generate SPs in the visible range with the same conditions as gold and silver due to its low skin depth. The skin depth curves of different metals considered in this thesis are shown in Figure 4.8. The actual region where aluminium performs better is the near-UV range, where its high skin depth compensates for its low layer thickness requirement.

The performance of the aluminium can be better investigated in the range from 900 nm to 1600 nm using the plots given in Figure 4.9. As seen in part b of this figure, the skin depth of Al is still very small, but as shown in Figure 4.9a, the resolution of the Al-based SPR sensor becomes better than the resolution of the Au-based sensor for wavelengths over 1200 nm roughly. Resolution performance of the Al-based sensor approaches to those of the Ag-based and Cu-based sensors around 1600 nm.

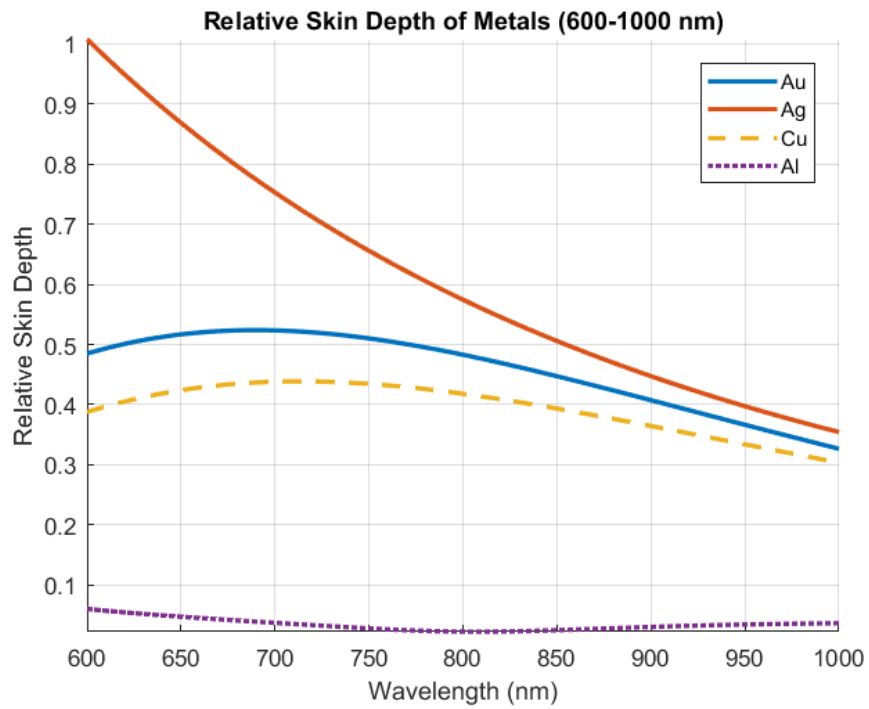


Figure 4.8: Skin depth of selected metals for 600-1000 nm range.

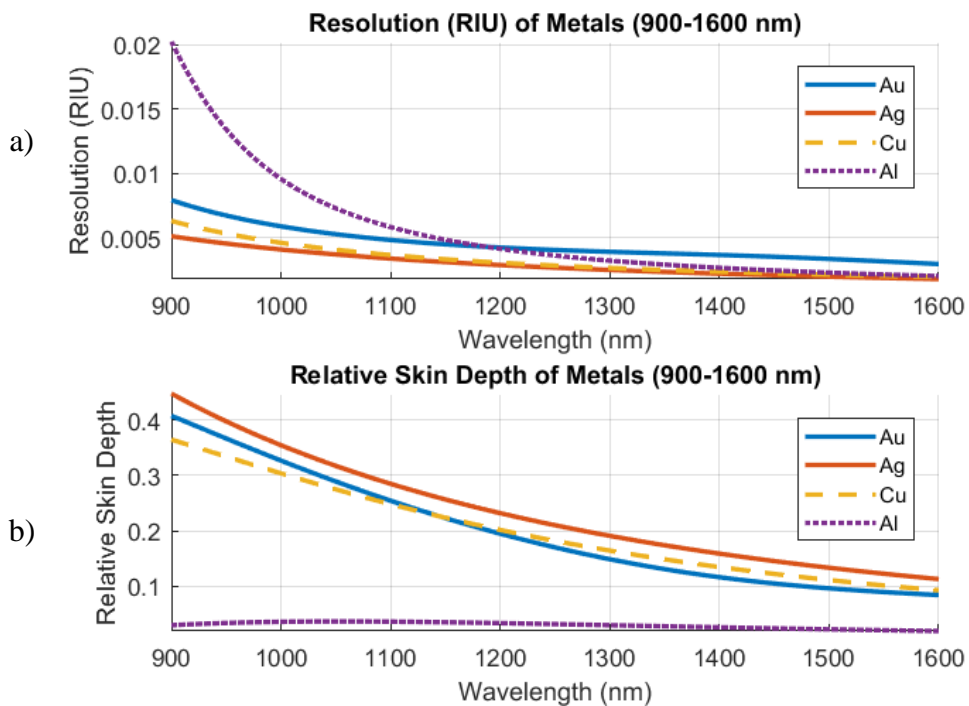


Figure 4.9: a) Resolution (RIU) of selected metals, and b) skin depth of selected metals, for 900-1600 nm range.

In conclusion, silver can be considered as the most suitable metal within the selected group of metals, as it is also reported in the literature. Silver depicts a very high all-range sensitivity and a moderate skin depth; thus, the silver layer is not required to be very thin and can be manufactured relatively easily. While gold and copper have similar performances, gold is used more commonly due to the presence of better-optimized fabrication processes and its robustness against degradation. Copper is a very active metal and can be quickly degraded, which makes it a less viable choice for reusable sensor applications. Therefore, silver and gold are relatively better choices as compared to copper and aluminium in SPR applications regarding sensitivity and robustness. So, their use can be further investigated in SPR applications aiming for multi-molecule detection.

CHAPTER 5

MULTI-SECTIONAL SPR SENSOR DESIGN

SPR sensors are designed to measure a single parameter, such as the presence of a specific molecule in a solution or, more specifically, its concentration. It is still an open area of research to design an SPR sensor that can be used to measure two or more different parameters simultaneously, if possible. This chapter investigates the feasibility of designing such multi-purpose SPR sensors by modifying the sensing layer. To achieve this goal, the dielectric sensing layer of the SPR sensor may be divided into two or more sensing layer patches. The resulting multi-sectional sensor structures can be analyzed by numerical CST simulations to see if this approach is useful to detect multiple analytes simultaneously.

A standard SPR sensor is composed of uniform thin layers made of glasses, metals, and various dielectrics, as discussed in previous chapters. In the multi-sectional SPR sensor topologies investigated in this chapter, the structure's glass prism and metal layers are kept the same, but the dielectric sensing layer (placed below the metal layer) is divided into two or more receptor patches made of different materials to attract different target molecules which may be present in the test medium in the bottom layer. The basic expectation from such a design is to observe different amounts of shifts in the minimum location of the sensor plasmon resonance curve under different sensing conditions regarding the test material's content. In a common biochemical sensor application, for instance, the bottom layer may be a liquid substrate (i.e., a test solution) that may be pure water, without containing any target molecules to be detected; or a single type of target molecules may exist in water to be attracted by one of the receptor patches; or there may be two different types of target molecules to be detected as they are attracted by two different receptor patches of the sensing layer, etc. If the amounts of the shift in the position (in reflection angle

or wavelength) of the resonance dip are sufficiently descriptive in each case, the solution's multi-variant content can be characterized.

5.1 Two-Sectional SPR Sensor Design: Basic Approach

Examples of SPR sensors with more than one resonance dips or examples of multi-channel SPR sensors designed to measure different test parameters at different channels can be found in the literature [95]–[98], [108], [109], [173], [175]. However, to the best of our knowledge, there is no SPR sensor reported that can simultaneously measure two different test parameters. In this chapter, a candidate sensor topology is proposed to investigate the feasibility of a multi-sectional SPR sensor whose sensing layer is composed of multiple patches. Other than the special structure of its sensing layer, the proposed SPR design borrows the common features of two different SPR sensors reported in the articles [167], [168]. These SPR sensors are already examined in Chapter 3, in sections 3.4.2.1 and 3.4.2.2, as examples of two different models regarding the sensing layer formation. The SPR sensors designed and tested in these two articles have common characteristics such as their basic topology, the operation bandwidth, and the similarity of the test solution used as the substrate layer. The electrical parameters of the structural and biological materials used in SPR design and testing are specified in sufficient detail in these two reference articles. Accordingly, a four-layer SPR sensor topology, similar to the one investigated in Chapter 4, is adopted to simulate the multi-sectional SPR sensor designs to be examined in this chapter. Instead of sampling the incidence/reflection angle over a wide angular range, the sensor analysis is carried on for two different reflection angles, 68° , and 76° , scanning a range of wavelengths from 500 nm to 800 nm with the same sampling steps used in Chapter 4.

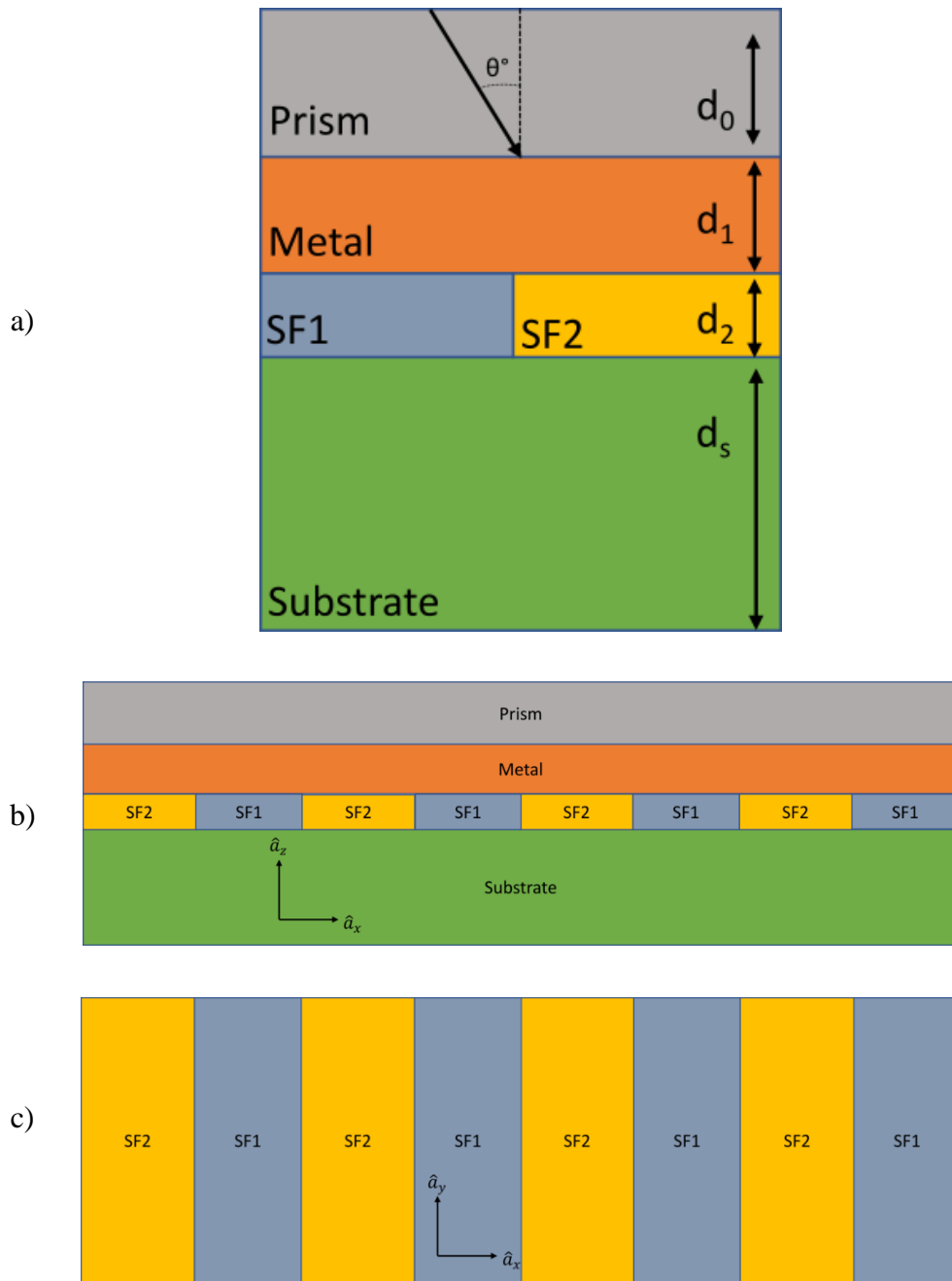


Figure 5.1: Four-layer SPR sensor structure with two-sectional SF, prior to molecular bonding: a) Single Cell topology on the xz -plane, b) Multiple-cells, seen from the xz -plane c) Striped pattern of sensing films, seen from the xy -plane (the SF layer is preceded by the prism and metal layers, and followed by the test substrate).

Prior to the design of two-sectional SPR sensors, as to be presented in Sections 5.2 and 5.3, two conventional 4-layer SPR sensors are simulated (each with a single uniform sensing layer) to detect the presence of a single target molecule for each of the test materials used in the reference articles [167] and [168]. Here, the purpose is to verify the agreement of our CST simulation results with the experimental results provided in [167], [168].

Next, a double-sectional SPR sensor is simulated by altering the sensing layer such that it is divided into two equal-sized patches of sensing films (SF1 and SF2) composed of different receptor materials (with different biochemical and electrical characteristics) as shown in Figure 5.1a to attract and bind different antibodies contained in the test solution. Values of the thickness parameters are not given in this figure as they vary from one case of simulation to another, but they will be specified in related subsections. The sensing films SF1 and SF2 and the rest of the SPR sensing cells are implemented in CST using the Unit Cell (UC) module. As the UC module repeats the basic cell structure periodically, long stripes of SF1 and SF2 are formed on the xy-plane. A cut from the xz-plane, on the other hand, shows a checkered pattern for the sensing film layer where SF1 and SF2 sections are repeated periodically. The three-dimensional geometrical description of this resulting structure is given in Figures 5.1a, 5.1b, and 5.1c.

5.2 Case 1: SPR Sensor to Detect BSA Protein

The basic topology of the two-sectional SPR sensor designed in this section is borrowed from the sensor design presented in [167]. The original sensor in this article is designed to detect bovine serum albumin (BSA) proteins (the target molecules) in a test solution of phosphate-buffered saline (PBS) that also contains Tween 20 molecules as detergent. A special bonding layer is designed to attach the BSA proteins to the sensor surface. The sensor structure's geometry is previously

given in Chapter 3, in Figure 3.11. The model used for the protein layer and the parameters of the substrate containing target proteins are already discussed in Chapter 3 in Section 3.4.2.1. The SPR sensor is designed using a 54 nm-thick gold layer and a nondispersive coupling prism glass made of BK7. The resulting sensor's reflectance curves are simulated prior to bonding and after bonding, first by using analytical calculations in MATLAB. Then, the same sensor is numerically simulated using CST. Results are given comparatively in Figures 5.2 and 5.3.

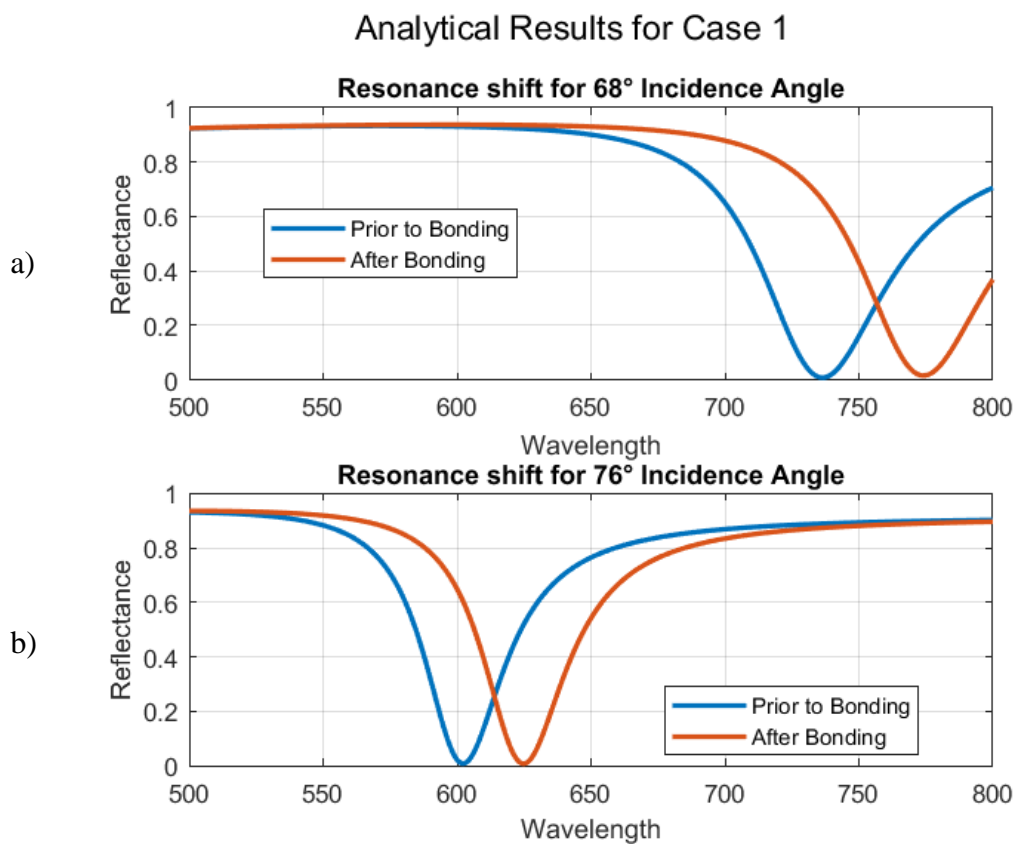


Figure 5.2: Analytical results for Case 1 computed by Matlab programming (refractive index data are provided by [167]) before and after the binding of BSA molecules for the incidence angle of a) 68° b) 76°.

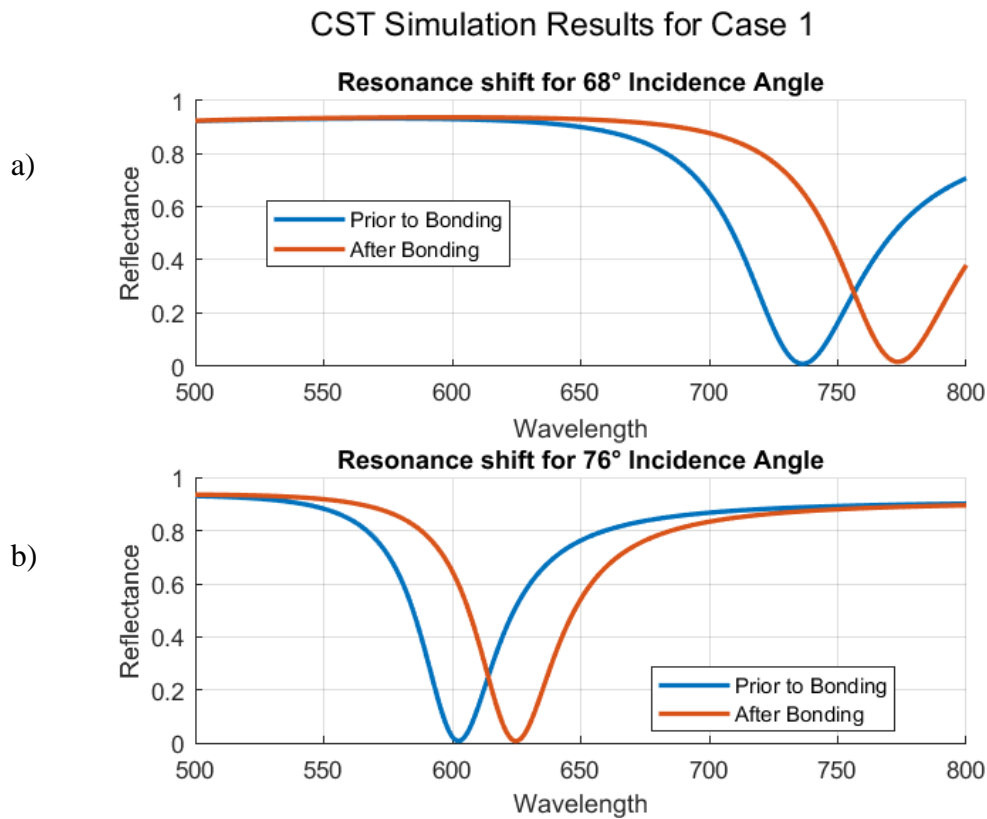


Figure 5.3. Results of numerical simulations for Case 1 obtained by CST Studio Suite (refractive index data are provided by [167]) before and after the binding of BSA molecules for the incidence angle of a) 68° b) 76°.

5.3 Case 2: SPR Sensor to Detect Protein G

The original SPR sensor design reported in [168] aims to analyze the effects of antibody orientations on sensor surface after bonding of protein G molecules (within the solution of PBS) and fabricated with a microscopic glass with $n=1.5151$ as coupling prism, attached to a gold layer of 49 nm thickness. A prolinker is used to immobilize G proteins on the sensor surface. The thickness of the Prolinker is 1.19 nm, while its complex refractive index is characterized by $n=1.350$ and $k=0.2$. Antibodies are attached to the Prolinker, forming a separate layer with a thickness of 13.8 nm and a complex refractive index of $n=1.383$ and $k=0.0095$. This sensor

design is excited by a mechanically rotated 675 nm laser using the angular scanning (or angular interrogation) method.

The bonding layer model and the target protein of the original sensor in [168] are borrowed to be used in the sensor structure implemented in Case 1 that is comprised of a BK7 prism layer and a 54 nm thick gold layer. In addition to changing the metal thickness and the type of the prism material, tests were also run with the wavelength scanning approach to make Case 1 and Case 2 results comparable. For the resulting SPR sensor, the reflectance curves obtained by the analytical approach/MATLAB calculations and by numerical CST simulations are presented in Figures 5.4 and 5.5, respectively.

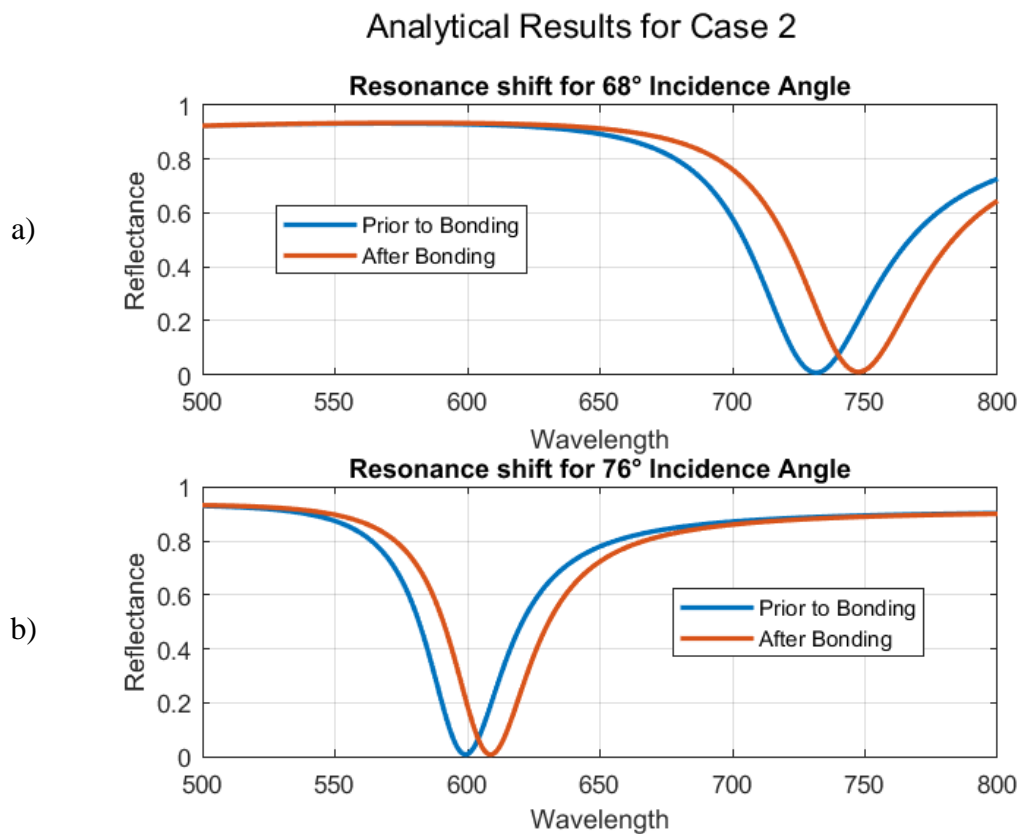


Figure 5.4: Analytical results obtained for Case 2 by Matlab programming (refractive index data are provided by [168]) before and after the binding of protein G molecules for the incidence angle of a) 68° b) 76°.

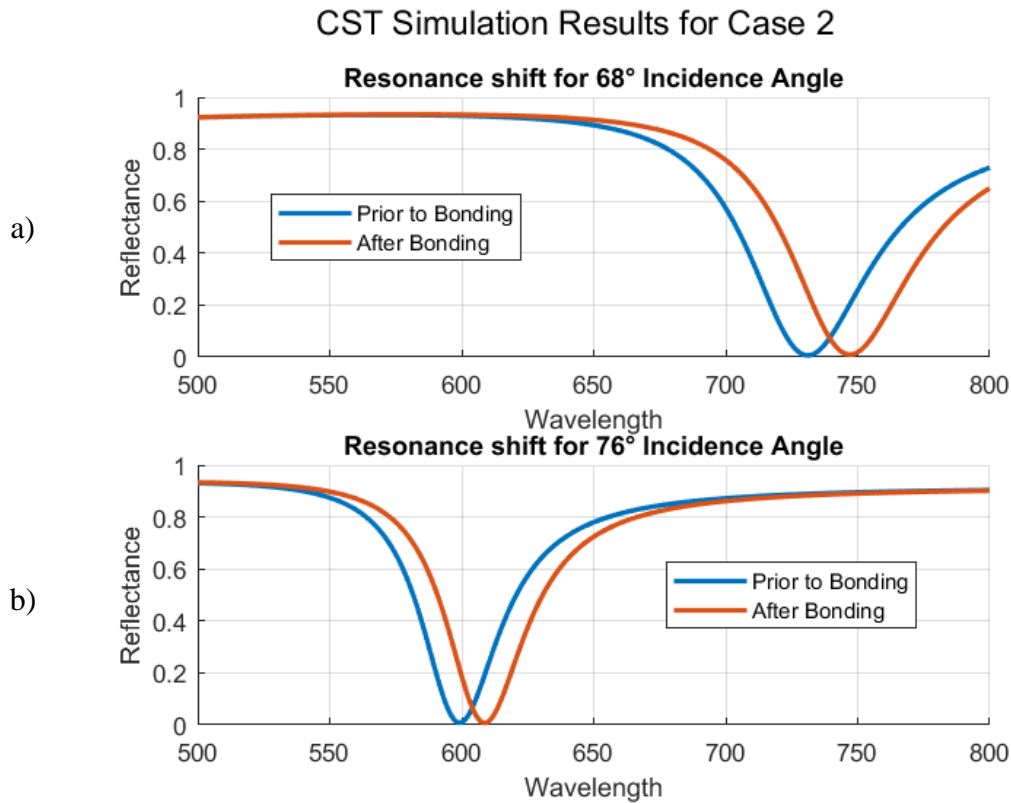


Figure 5.5: Results of numerical simulations for Case 2 by CST Studio Suite (refractive index data are provided by [168]) before and after the binding of protein G molecules for the incidence angle of a) 68° b) 76°.

5.4 SPR Sensor with Striped (Double-patch) Sensing Film Design

In case of two or more molecules are present in a solution (such as blood, tap water, etc.) that acts as the bulk substrate layer of a multilayered SPR sensor, one of the methods would be used is to design a different bonding layer for each target molecule to attract them to different parts of the sensing layer. Since the analytical solution approach employed in Chapter 2 does not work in a straightforward manner for this case, numerical simulations need to be used to analyze such multi-sectional sensor structures, in general.

In this section, the basic SPR sensor design used in Cases 1 and 2 of Sections 5.2 and 5.3, respectively, will be simulated for various double-sectional SPR sensor cases. In the first group of simulations, the aim is to detect the presence of two different types of target molecules, BSA and G protein molecules, contained in the PBS solution simultaneously. Secondly, a hypothetical case will be simulated where the sensing layer formed by one of the target molecules is assumed to have higher losses as compared to the other target molecule.

5.4.1 Two-sectional Sensing Film with Two Lossless Target Molecules

In this section, the presence of two different target molecules (BSA and G protein molecules) will be assumed in the solution of PBS. As shown in Figure 5.1, the sensor topology is formed by a prism made of BK7 glass, a 54nm-thick gold layer, a double-patch sensing layer, and a liquid substrate that is comprised of PBS+Tween 20 substrate solution containing BSA and G protein molecules. Data for the thickness and the refractive index of the sensing layers before and after molecular bonding are borrowed from [167], [168], as mentioned previously. The sensor with double-patch sensing film is simulated for four different cases: The first simulation is performed when there is no molecular bonding, i.e., the pure substrate solution exists together with the basic sensing layers, the metal layer, and the prism are present. The second and third simulations are run with each of the proteins bonded alone to their sensing films, and the fourth simulation is performed when both molecules are bonded to their relative sensing layers.

The bulk medium is assumed to be very thick, having a large volume so that the presence of protein G and BSA proteins are negligible in changing the refractive index of the bulk medium. This assumption guarantees that bulk medium would behave the same whether or not any of (or both of) the proteins are present in the bulk medium.

Tests are performed at two different incidence/reflection angles, and the resulting SPRFs (Surface Plasmon Reflectance Functions) are plotted in Figure 5.6 parametrically. At the incidence angle of 76° , a sharper resonance is observed, while the SPRFs simulated at 68° show more significant wavelength shifts in response to different molecular binding scenarios. The zoomed version of Figure 5.6 is given in Figure 5.7 to observe the resonance minimum shifts more clearly.

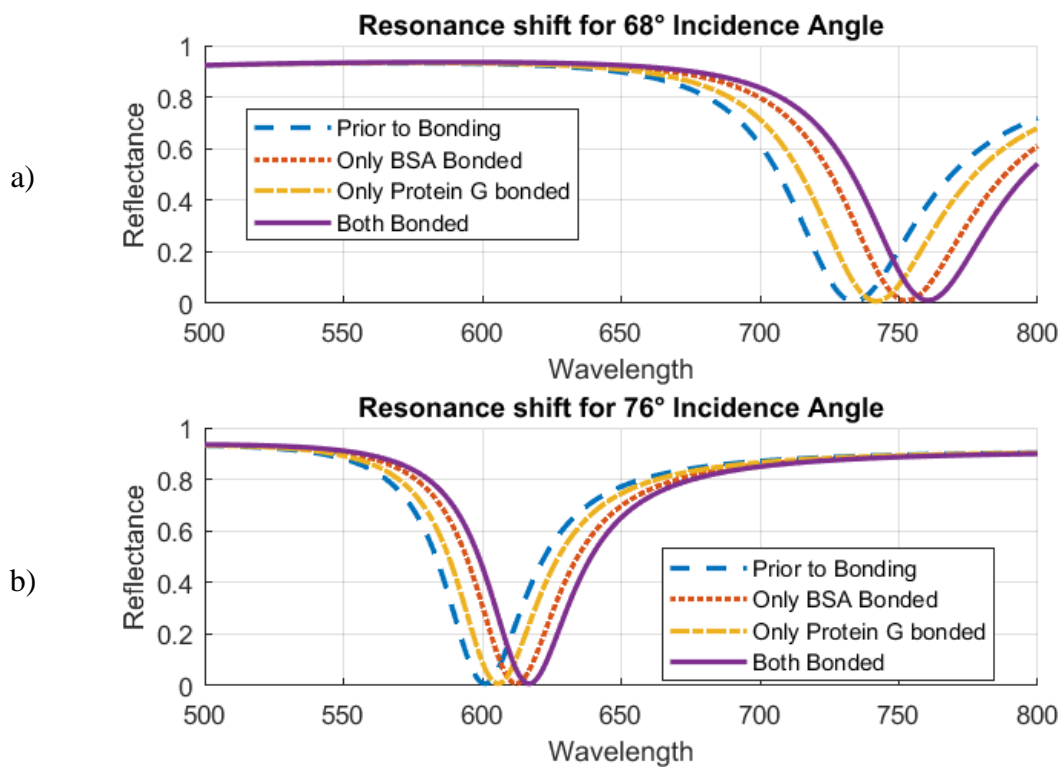


Figure 5.6: Results of numerical simulations for SPRFs by CST Studio Suite (refractive index data are provided by [167], [168]) for four different combinations of molecular bonding regarding the BSA and G proteins at the incidence angle of a) 68° and b) 76° .

Resonant dip position prior to bonding is similar to single-target molecule simulation results already discussed in Sections 5.2 and 5.3, and there is only a small difference as the thickness of the sensing layer is very small. Positions of resonant dips are shown in Table 5.1 with resonant dip shifts, and it shows that the resonance dip shift

in the case where both of the proteins are immobilized on their relative bonding layers is approximately equal to the sum of the shifts of resonance positions when materials are separately bonded.

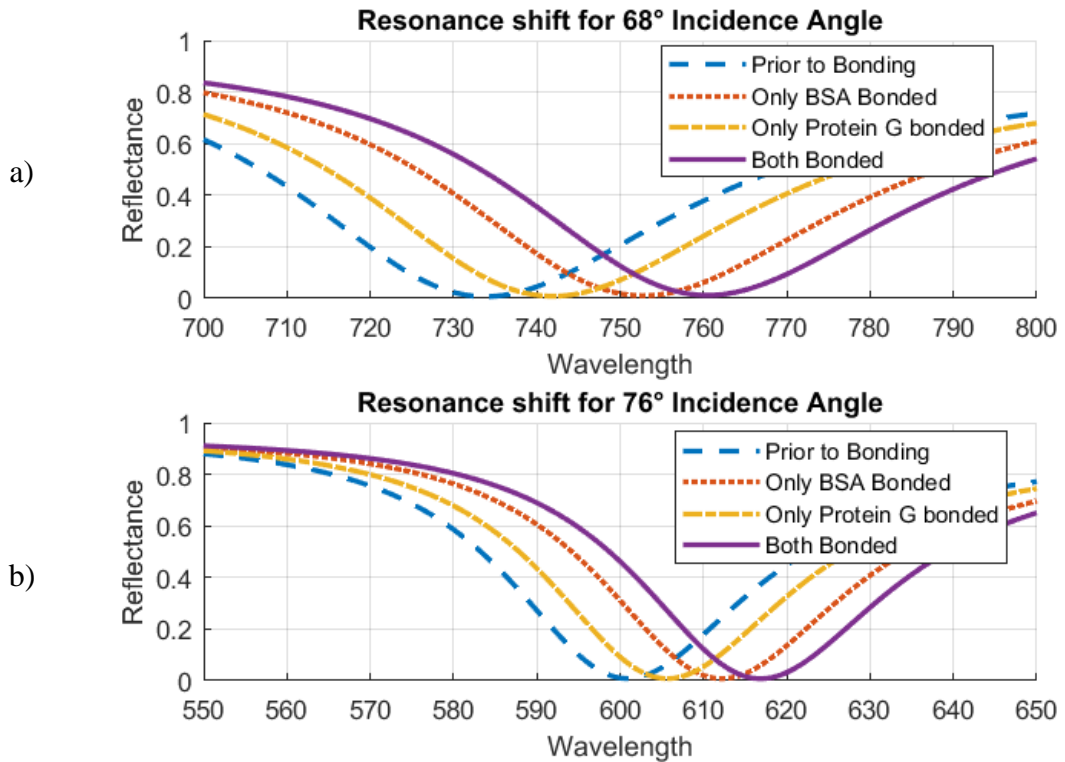


Figure 5.7: Results of numerical simulations by CST Studio Suite (the zoomed-in version of the plots shown in Figure 5.6).

As seen in Figure 5.7a, for the incidence angle of 68°, the sum of the resonance shifts is equal to 26.399 nm when proteins are coupled separately. On the other hand, the resonant shift when both of the proteins are coupled at the same time is 26.367 nm for the 68°. In Figure 5.7b, for the incidence angle of 76°, these values become 15.754 nm and 15.846 nm, respectively. Another similar linear scaling is observed in frequency shifts when the simulation results of Sections 5.2 and 5.3 are compared to those presented in Figure 5.7. The frequency shift observed for the double-SF structure with a single target molecule bonding is about half of the

frequency shift observed for a single-SF structure after molecular bonding (for the same target molecule).

These tests are performed for very high concentrations of target molecules in the PBS solution. Experimental results shown in [167] reveals that an increase in concentration leads to an increase in the refractive index change and also an increase in the wavelength shift observed for the dip position of the SPRF. In other words, wavelength shifts are larger when more proteins bond to the sensing film(s). Results from [168], shown in Figure 5.10, also support these observations. These results can be generalized since the shift of resonance dip in wavelength is always towards the right (i.e., to larger wavelengths). As the refractive index of any of the bottom two layers (sensing layer and the sample, and newly-formed molecular layers) increases until a threshold is reached where the SPs fails to penetrate through the layer, the resulting sensor structures can be considered as one-less layered (i.e., a 4-layer system becomes a 3-layer system) system and can be analyzed accordingly.

Table 5.1: Resonant wavelength positions and shifts (in nm), for BSA/Protein G bonding, at 68° and 76° incidence angles

Bonding	68°(<i>shift</i>)	76°(<i>shift</i>)	Single 68°	Single 76°
None			736337 ^a	602319 ^a
(Empty)	733.945	600.962	731128 ^b	602299 ^b
Only BSA	752.587 (18.642)	612.276 (11.314)	773.544 (37.167)	624.902 (22.583)
Only Protein G	741.702 (7.757)	605.602 (4.640)	747.105 (15.977)	608.643 (6.344)
Both	760.312 (26.367)	616.808 (15.846)	-	-

^a: data for BSA sensing; ^b: data for protein G sensing, for their relative single-SF simulations. Data given in parentheses are the resonance position shifts(in nm) after molecular bonding is complete.

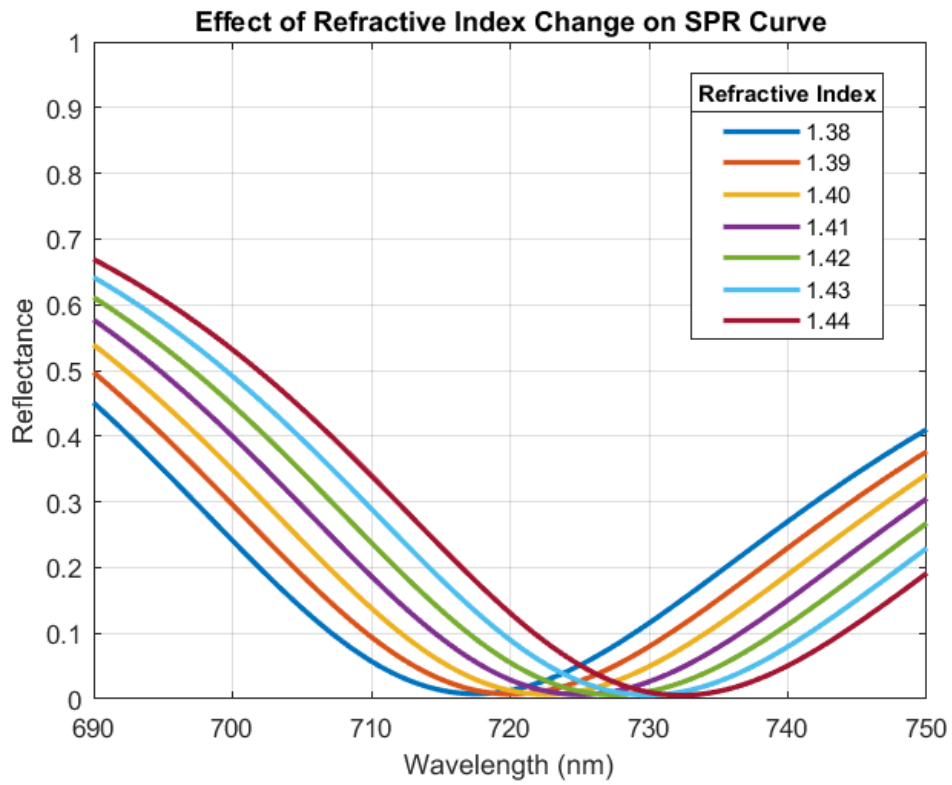


Figure 5.8: Effects of the increasing refractive index on the SPRF curve (computed using the sensor topology given in [167]) for the incidence angle of 68° .

Thus, the phenomenon of ‘always-right-shift’ limits the usability of multi-sectional sensing films in SPR sensors with wavelength interrogation.

Similar results are expected in the case of angular scanning measurements, where the shift in the resonant dip would occur towards the higher incidence angles, as it can be deduced from Equation 2.92.

Such a sensor structure requires an extra labeling step to end up with accurate sensing in the presence of two different target molecules simultaneously. An SPR sensor measuring only angular shifts or only wavelength shifts in the reflectance curve’s minimum will not be able to monitor two different targets at the same time without extreme and unrealistic limitations such as assuring target molecules are present only

at certain concentration values, or the molecules do not coexist together. Even in that case, it might be practically impossible to understand which molecule is present since the resonant dip shift does not tell anything about it. Thickness-based measurements yield the same results as the results of Case 2 imply in Table 5.1; an increase of the thickness (as the protein G layer is modeled as a whole new layer) also shifts the spectrum in a similar way.

5.4.2 Two-sectional Sensing Film with One Lossless / One Lossy Target Molecules

Based on the results of the previous section, it is concluded that in SPR sensing, one more variable is required to sense the presence of two different target materials simultaneously. A possibility is to design the SPR sensor to sense two different materials with different levels of material losses.

Losses in any of the sensor layers (excluding the metal layer, which is more complicated as discussed in Chapter 3, in Section 3.2) changes the SPR spectrum in two ways: increases the minimum level of resonant dip (i.e., shifts the resonant dip upwards), and increases the FWHM (full width at half maximum) or reduces the Q factor of SPR spectrum. This effect is caused in general by lossy materials, as demonstrated in Figure 5.9, where the measurement layer introduced a loss, and the loss is increased step by step to show the resulting effect on the SPRF curve; the spectrum moves up, widens, and moves towards larger wavelengths with an increasing extinction coefficient. Thus, the lossy materials have a different effect on the SPRF as compared to lossless materials. In other words, the loss phenomenon might be used to sense two different materials with different loss levels at the same time. It can be seen that the SPRF minimum not only moves up with a widening resonance curve, but the resonance dip also moves towards larger wavelengths as the refractive index increases. However, measuring the shift in the resonance dip due to the bonding of the lossy material molecules alone may be used as a reference. Then

subtracting this reference shift from the total resonance shift that occurs in the presence of both types of bonding to find out the shift caused by the lossless material by itself.

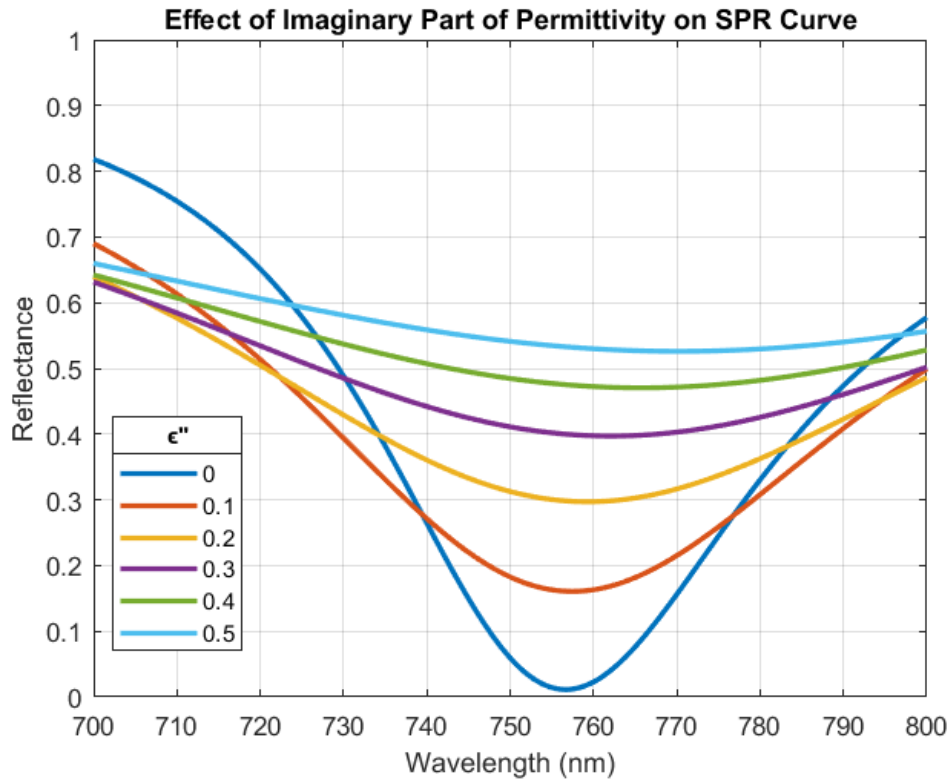


Figure 5.9: Variation of the SPRF curve (from [167]) in response to the change in the imaginary part of the permittivity of the test medium.

To test this hypothesis, a loss is introduced to the previously discussed protein G model by adding $\epsilon'' = 0.3$ to its permittivity. This hypothetical material is then simulated with the same SPR sensor topology defined earlier at the same operation angle and wavelength (i.e., the protein G simulation is just repeated) to see its resonant behavior in a single-SF case and compare it with two-SF simulations. Results of the single-SF simulations of lossy material are given in Figure 10. Single material simulation results are in agreement with the previous idea on the effect of lossy materials on the SPRF curves, as bonding of lossy molecules shifted the

resonant dip upwards, increased FWHM, and shifted the spectrum towards larger wavelengths take place.

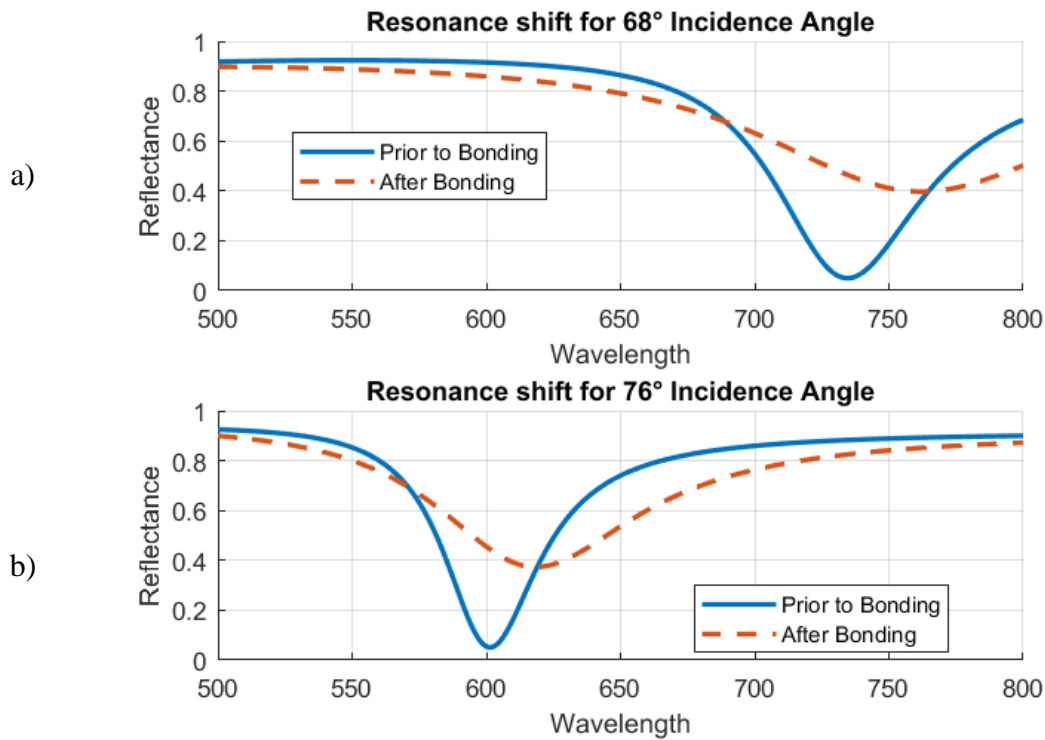


Figure 5.10: Results of the numerical simulations for the SPRF by CST Studio Suite for the hypothetical lossy material, prior to and after the molecular bonding for the incidence angle of a) 68° and b) 76°.

After single target molecule tests, simulations in Section 5.4.1 are repeated with BSA protein and a lossy material (replacing the protein G) while keeping the sensor topology and all other simulation parameters the same. Resonant dip shifts when the BSA protein molecules are bonded only as simulated earlier. It is also important to note that lossless materials only shift the resonance dip position along the wavelength axis. As expected, bonding of the lossy material shifts the resonant dip in both intensity and wavelength. FWHM of the resonance curve increases too. These assessments can be observed in the zoomed-in version of Figure 11, in Figure 12, and the values of resonant dip positions are given in Table 5.2.

Secondly, it is observed that the collective shift in the double-bonding case is the average of the shift occurring in individual bonding cases, and the one-material shift in the double-sensing-layer case is half of the single-sensing-layer case. Besides, the 68° angle of incidence is more strongly affected by the presence and bonding of the lossy material as its shifts to higher minimum values are evident in Figure 5.11

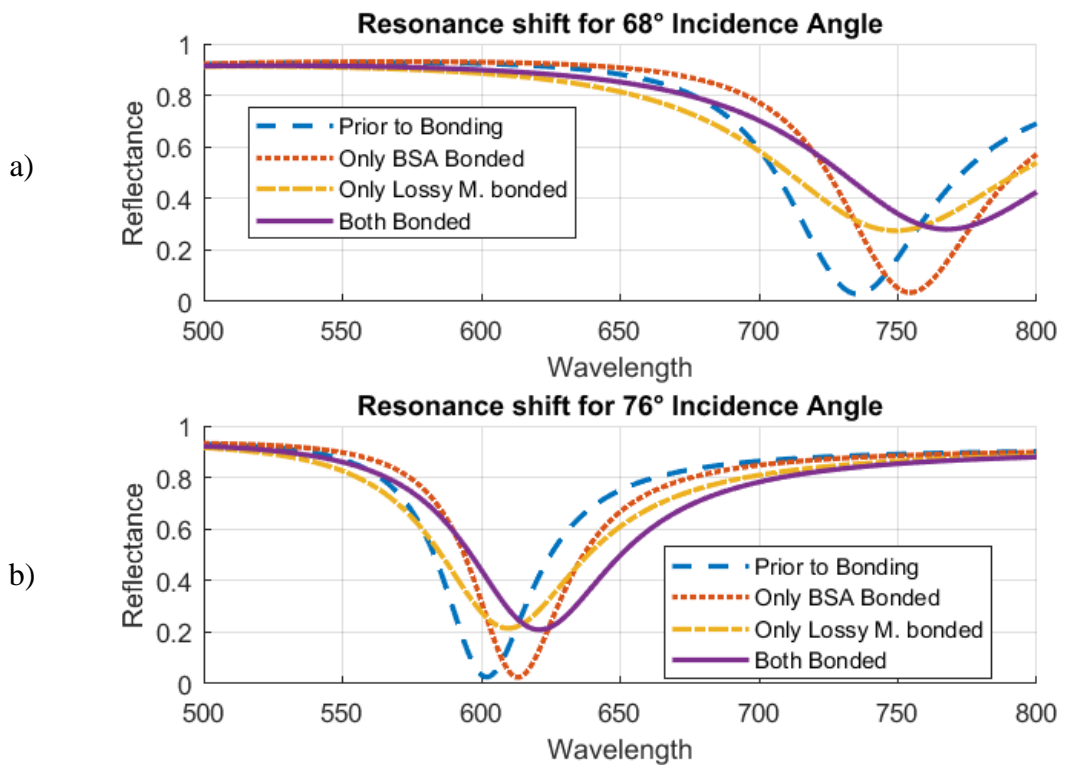


Figure 5.11: Results of numerical simulations for the SPRF curves by CST Studio Suite, before and after the bonding of BSA and lossy molecule in four different bonding scenarios for the incidence angle of a) 68° and b) 76° .

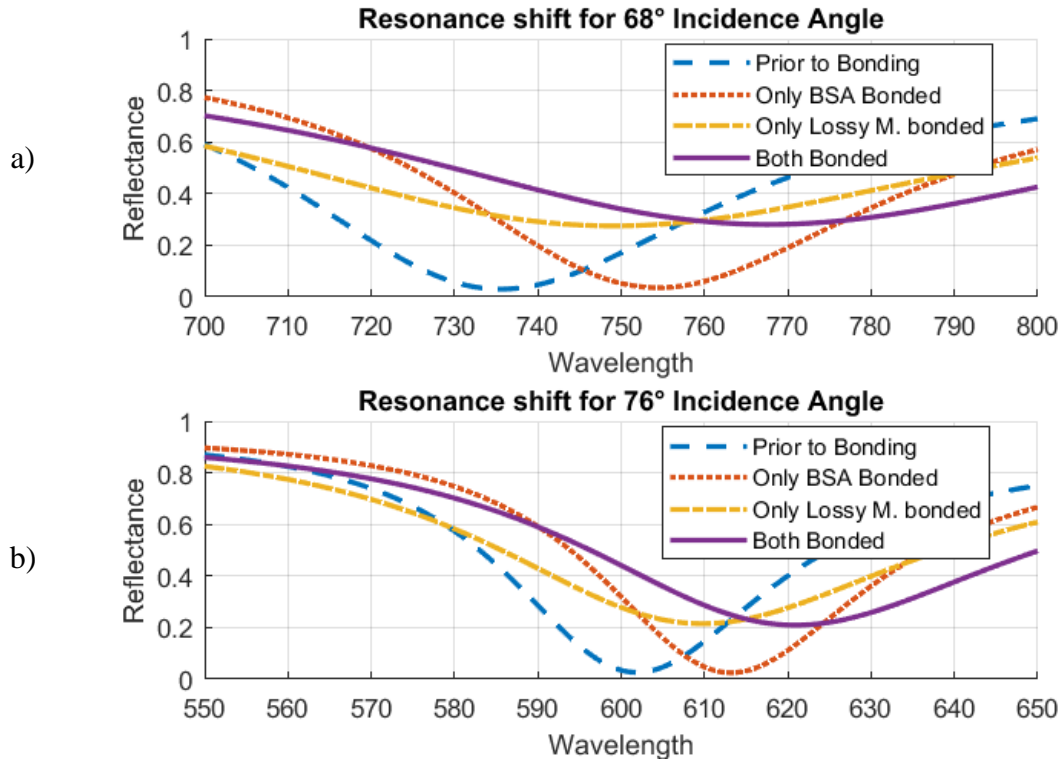


Figure 5.12: The zoomed-in version of Figure 5.11.

Table 5.2: Resonant wavelength positions and shift amounts for BSA/Lossy molecule bonding

Bonding	68°(shift)	76°(shift)	Single 68°	Single 76°
None			736377 ^a	602319 ^a
(Empty)	735.565	601.775	734754 ^b	601504 ^b
Only BSA	754.290 (18.725)	613.121 (11.346)	773.544 (37.167)	624.902 (22.583)
Only Lossy	749.204 (13.639)	609.756 (7.981)	762.050 (27.296)	618.454 (16.950)
Both Layers	767.754 (32.189)	620.829 (19.054)	-	-

^a: data for BSA; ^b: data for lossy molecule, for their relative single-SF simulations.

Values in parentheses are the resonance position shift after bonding.

The values of resonance curve minima are given in Table 5.3 for further assessments. It can be observed that lossless layers (i.e., BSA and the molecular layer formed after bonding) have minimal effect on resonant dip value. Thus, the upward-shift in resonance dip is mostly caused by the presence of lossy material and can be used for deciding the presence and concentration of the lossy material molecules in the liquid substrate.

Table 5.3: Minimum Value of Resonant Dip and Shifts from the Empty Case

Bonding	$68^\circ(\text{shift})$	$76^\circ(\text{shift})$	Single 68°	Single 76°
None (Empty)	0.0297	0.0262	0.0008	0.0008
			0.00498	0.0676
Only BSA	0.0353	0.0272	0.0015	0.0077
	(0.0056)	(0.0010)	(0.0007)	(0.0069)
Only Lossy	0.2749	0.2150	0.3971	0.3734
	(0.2452)	(0.1888)	(0.3473)	(0.3058)
Both Layers	0.2804	0.2094	-	-
	(0.2507)	(0.1832)		

^a: data for BSA; ^b: data for lossy molecule, for their relative single-SF simulations. Values in parentheses are the resonance minimum shift after bonding

As a further investigation, the effects of variation in the imaginary part of the permittivity, ϵ'' , on the minimum value of the SPR sensor's resonant curve at the dip position are simulated for three different molecular bonding scenarios as shown in Figure 5.13. Simulation results for varying ϵ'' values proved that the upward-shift of minimum value could only be related to losses. Simulation results when only lossy-material is coupled, and both materials are coupled (middle and bottom figures) are almost identical to each other. Thus, a preset created with controlled experiments (i.e., specific amounts of bonding) can be used to detect two materials using both data. Figure 5.13 proves relatively larger sensitivity at 68° incidence angle tests, as

it reaches higher minimum values in high losses while the initial tests with lower losses are similar for each incidence angle.

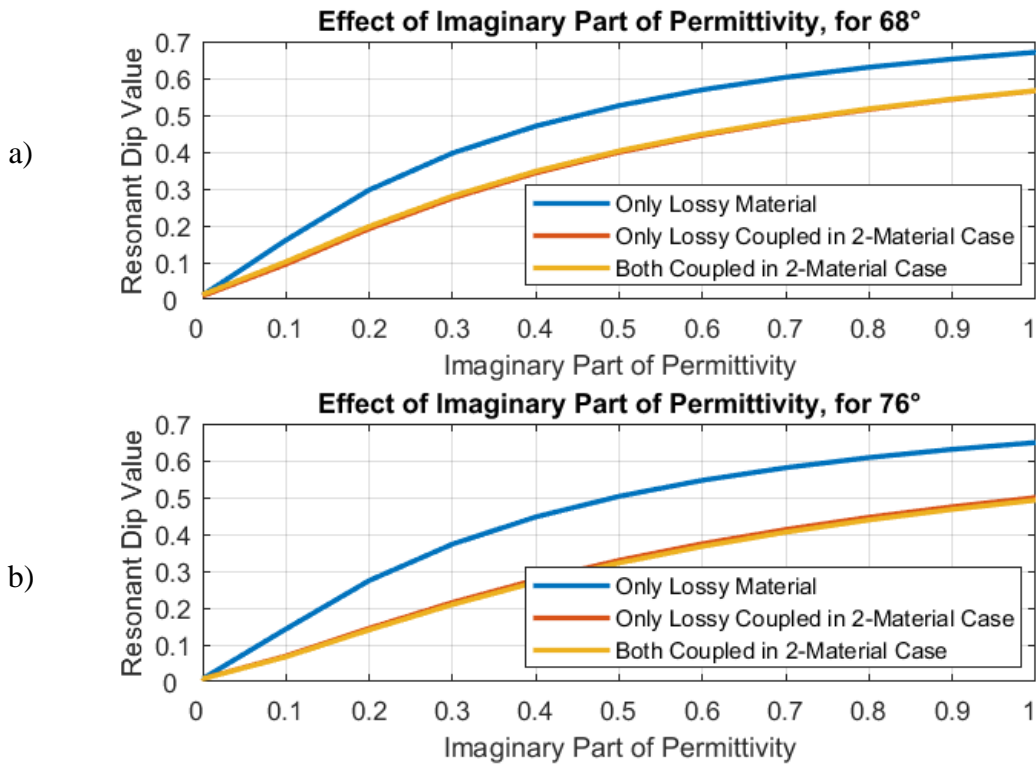


Figure 5.13: Change of the minimum value of resonance dip versus the change in the imaginary part of the complex permittivity. Curves for only lossy material coupled and both BSA/Lossy coupled in two-material cases are overlapping; it proves the effect on minimum resonant dip value comes only from lossy material.

The final step for the lossy material is testing the effect of changing the sensing layer thickness; this would provide a more realistic analysis, as an increase in material concentration may lead to increases in layer thickness. Simulations are performed with the previously used $\epsilon'' = 0.3$ assumption, and layer thickness is increased from 1 to 16 nm to test if the upward-shift can be related to changing thickness as it is in the previous case; simulation results are given in Figure 5.14.

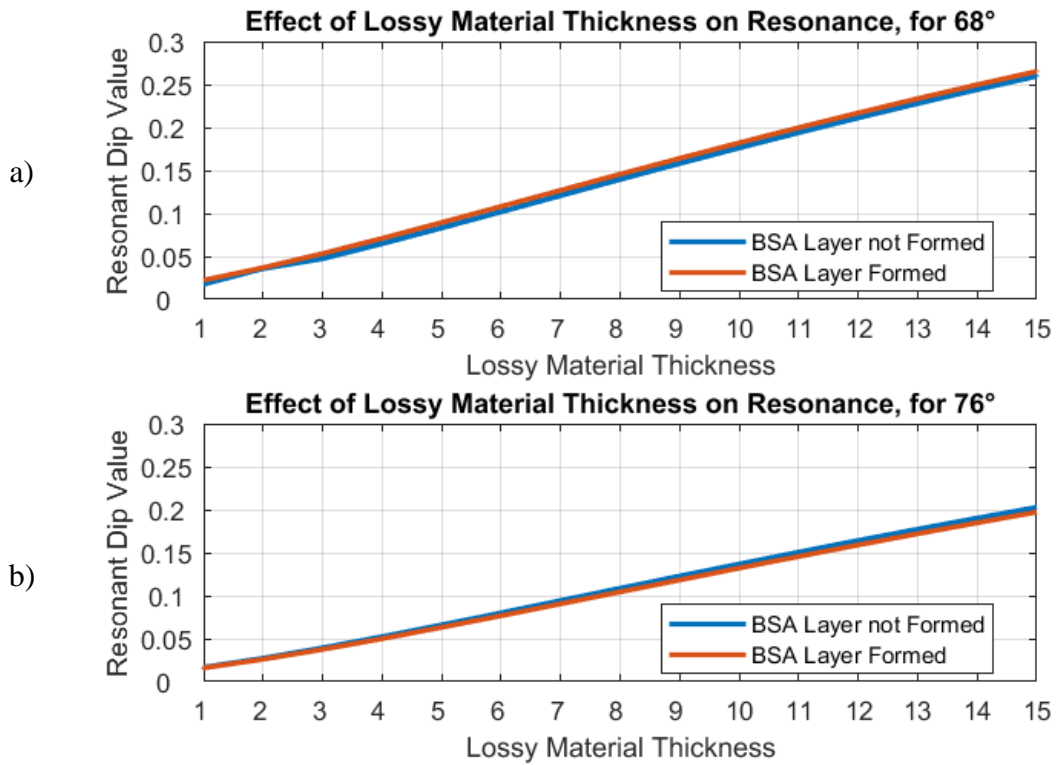


Figure 5.14: Change in resonance minimum value with varying thickness values and for 68° and 76° incidence angle cases where $\epsilon''=0.3$ is kept constant.

Figure 5.14 shows that the presence of an additional lossless layer does not significantly affect the minimum level since both results are virtually identical. Thus, using controlled preliminary tests, one can decide the amount or existence of coupled materials using the minimum level and resonance shift since the shift in resonance dip position can be estimated using the approach mentioned above.

Simulations in Sections 5.3 and 5.4 have shown that SPR structures with a two-sectional sensing film design can nominally support the simultaneous detection of two materials in a particular solution.

SPR sensors in biosensing require sensing-layers to attract and immobilize target biomolecules virtually in all applications. Otherwise, detecting molecules within a complex substrate solution, such as blood, would be impossible since sensors work

over the bulk refractive index. Multi-molecule detection is only possible if such sensing layers can be created, and different spectrum parameters (such as resonant dip, resonant minimum, FWHM, as discussed previously) affected differently by the presence of different molecules.

CHAPTER 6

CONCLUSION

The purpose of this thesis was to provide a comprehensive analysis of the basic SPR theory from an engineering electromagnetics perspective, to analyze the materials used in SPR applications, and to use their properties to investigate the feasibility of an SPR sensor with a multi-sectional sensing film to detect multiple molecules in a solution simultaneously.

Analysis of SPR sensors starting from the basic electromagnetic formulations was given in Chapter 2 by doing a comprehensive study of multilayered systems and surface waves in such systems; this analysis was necessary to understand the fundamentals of the SPR phenomenon and to compute the SPR reflectance curves as a function of wavelength and/or incidence angle. In Chapter 3, materials used in SPR sensors were discussed, and their permittivity functions were modeled for SPR analysis. The first two chapters form the backbone of the thesis as they provide the necessary theoretical background and information to analyze SPR topologies.

The effect of metals on the SPR spectrum was discussed in Chapter 4 with the help of the background presented in Chapter 3. Metals are the most important and interesting components in the SPR topology. Decreasing the loss of metals increases the resolution of SPR sensors. However, surface plasmon waves cannot be excited if a perfect electric conductor is used (theoretically) in the SPR sensor design, as the incident wave cannot penetrate into the perfect conductor layer. The most popular metals in SPR applications are gold, and silver which were analyzed together with two other metals (copper and aluminium) as they are used in various SPR topologies and other plasmonic applications, as reported in the literature. Analysis results for metals were in agreement with research results reported in the literature. Silver has

proven to be the most effective metal (out of four selected metals), with copper is being the second best, followed by gold. Aluminium was found to be ineffective due to its high loss for visible and near-IR simulations.

In Chapter 5, a basic SPR topology with a two-part sensing film in a striped fashion was analyzed for its feasibility to simultaneously detect multiple molecules. Analysis initially started with two proteins modeled as lossless materials (BSA and protein G), and their tests show that the bonding of any molecule with negligible loss to the bonding layers has similar effects on the spectrum. The tests were repeated by artificially introducing loss to protein G to create a lossy molecule. Analysis in Chapter 5 is concluded that conventional SPR topologies can only nominally support multiple molecule detection under certain conditions.

Although the SPR literature is very comprehensive, the area of multi-sensing has a minimal share. Sensing multiple elements in a complex substrate (such as human blood) would revolutionize the field and be very efficient in the healthcare industry. SPR sensors can operate with microscopic samples, rapidly giving results and detecting small molecules. For example, the coronavirus variant causing Sars-Cov2 has a diameter of 60 to 140 nm, thicker than most of the SPR sensor layers. Even the glycoproteins of the viral envelope of coronavirus have a size between 9 to 12 nm, which can easily be detected by SPR sensors, provided that proper bonding layers are available and realizable. Put aside a complex structure such as a virus, SPR sensors today can perform molecular level detection as a standard procedure.

6.1 Future Work

The thesis is concluded with a feasibility study on multi-sensing; though, no complete design has been suggested. Designing an SPR sensor with realistic materials and suitable sensing layers to detect the presence of multiple target

molecules in a given complex substrate could be a future work following this thesis. Different asymmetrical sensing film topologies may be investigated to find a better working solution. Also, a wider class of selected metals or alloys may be investigated in SPR design, including their temperature behaviors in the sensor analysis.

Finally, efficient measurement systems can be useful for rapid reaction in a health crisis, such as pandemics. SPR sensors may serve as rapid-test kits and could be employed in hospitals and even in field testing due to their high resolution and their promising capacity in molecular-level biochemical detection.

REFERENCES

- [1] J. Homola, S. S. Yee, and G. Gauglitz, “Surface plasmon resonance sensors: review,” *Sensors and Actuators, B: Chemical*, vol. 54, no. 1, pp. 3–15, Jan. 1999, doi: 10.1016/S0925-4005(98)00321-9.
- [2] P. Vadgama and P. W. Crump, “Biosensors: Recent trends a review,” *The Analyst*, vol. 117, no. 11, pp. 1657–1670, 1992, doi: 10.1039/an9921701657.
- [3] X. Zhang *et al.*, “Terahertz surface plasmonic waves: a review,” doi: 10.1117/1.AP.2.1.014001.
- [4] D. Pines and D. Bohm, “A collective description of electron interactions: II. Collective vs individual particle aspects of the interactions,” *Physical Review*, vol. 85, no. 2, pp. 338–353, 1952, doi: 10.1103/PhysRev.85.338.
- [5] K. A. Willets and R. P. van Duyne, “Localized surface plasmon resonance spectroscopy and sensing,” *Annual Review of Physical Chemistry*, vol. 58, pp. 267–297, 2007, doi: 10.1146/annurev.physchem.58.032806.104607.
- [6] A. D. Kersey *et al.*, “Fiber grating sensors,” *Journal of Lightwave Technology*, vol. 15, no. 8, pp. 1442–1462, Aug. 1997, doi: 10.1109/50.618377.
- [7] D. K. Gramotnev and S. I. Bozhevolnyi, “Plasmonics beyond the diffraction limit,” *Nature Photonics*, vol. 4, no. 2, pp. 83–91, Feb. 2010, doi: 10.1038/nphoton.2009.282.
- [8] J. A. Schuller, E. S. Barnard, W. Cai, Y. C. Jun, J. S. White, and M. L. Brongersma, “Plasmonics for extreme light concentration and manipulation,” *Nature Materials*, vol. 9, no. 3, Nature Publishing Group, pp. 193–204, 2010, doi: 10.1038/nmat2630.

- [9] E. Ozbay, “Plasmonics: Merging photonics and electronics at nanoscale dimensions,” *Science*, vol. 311, no. 5758. pp. 189–193, Jan. 13, 2006, doi: 10.1126/science.1114849.
- [10] S. Lal, S. Link, and N. J. Halas, “Nano-optics from sensing to waveguiding,” *Nature Photonics*, vol. 1, no. 11, pp. 641–648, Nov. 2007, doi: 10.1038/nphoton.2007.223.
- [11] L. Novotny and N. van Hulst, “Antennas for light,” *Nature Photonics*, vol. 5, no. 2, pp. 83–90, Feb. 2011, doi: 10.1038/nphoton.2010.237.
- [12] J. Hodgkinson and R. P. Tatam, “Optical gas sensing: A review,” *Measurement Science and Technology*, vol. 24, no. 1. Institute of Physics Publishing, p. 012004, Nov. 28, 2013, doi: 10.1088/0957-0233/24/1/012004.
- [13] E. Kretschmann, “Die bestimmung der oberflächenrauigkeit dünner schichten durch messung der winkelabhängigkeit der streustrahlung von oberflächenplasmaschwingungen,” *Optics Communications*, vol. 10, no. 4, pp. 353–356, Apr. 1974, doi: 10.1016/0030-4018(74)90362-9.
- [14] R. W. Wood, “On a remarkable case of uneven distribution of light in a diffraction grating spectrum,” *Proceedings of the Physical Society of London*, vol. 18, no. 1, pp. 269–275, Jun. 1901, doi: 10.1088/1478-7814/18/1/325.
- [15] R. W. Wood, “ XXVII. Diffraction gratings with controlled groove form and abnormal distribution of intensity ,” *The London, Edinburgh, and Dublin Philosophical Magazine and Journal of Science*, vol. 23, no. 134, pp. 310–317, Feb. 1912, doi: 10.1080/14786440208637224.
- [16] Lord Rayleigh, “ III. Note on the remarkable case of diffraction spectra described by Prof. Wood ,” *The London, Edinburgh, and Dublin Philosophical Magazine and Journal of Science*, vol. 14, no. 79, pp. 60–65, Jul. 1907, doi: 10.1080/14786440709463661.

- [17] U. Fano, "The Theory of Anomalous Diffraction Gratings and of Quasi-Stationary Waves on Metallic Surfaces (Sommerfeld's Waves)," *Journal of the Optical Society of America*, vol. 31, no. 3, p. 213, Mar. 1941, doi: 10.1364/josa.31.000213.
- [18] D. Bohm and D. Pines, "A collective description of electron interactions: III. Coulomb interactions in a degenerate electron gas," *Physical Review*, vol. 92, no. 3, pp. 609–625, Nov. 1953, doi: 10.1103/PhysRev.92.609.
- [19] H. Watanabe, "Experimental Evidence for the Collective Nature of the Characteristic Energy Loss of Electrons in Solids — Studies on the Dispersion Relation of Plasma Frequency —," *Journal of the Physical Society of Japan*, vol. 11, no. 2, pp. 112–119, Dec. 1956, doi: 10.1143/JPSJ.11.112.
- [20] L. B. Leder, H. Mendlowitz, and L. Marton, "Comparison of the characteristic energy losses of electrons with the fine structure of the x-ray absorption spectra," *Physical Review*, vol. 101, no. 5, pp. 1460–1467, Mar. 1956, doi: 10.1103/PhysRev.101.1460.
- [21] A. Otto, "Excitation of nonradiative surface plasma waves in silver by the method of frustrated total reflection," *Zeitschrift für Physik*, vol. 216, no. 4, pp. 398–410, Aug. 1968, doi: 10.1007/BF01391532.
- [22] E. Kretschmann and H. Raether, "Radiative Decay of Non Radiative Surface Plasmons Excited by Light," 1968. Accessed: Sep. 04, 2020. [Online].
- [23] B. Liedberg, C. Nylander, and I. Lundström, "Biosensing with surface plasmon resonance - how it all started," *Biosensors and Bioelectronics*, vol. 10, no. 8, 1995, doi: 10.1016/0956-5663(95)96965-2.
- [24] B. Liedberg, C. Nylander, and I. Lunström, "Surface plasmon resonance for gas detection and biosensing," *Sensors and Actuators*, vol. 4, no. C, pp. 299–304, Jan. 1983, doi: 10.1016/0250-6874(83)85036-7.

- [25] C. Nylander, B. Liedberg, and T. Lind, “Gas detection by means of surface plasmon resonance,” *Sensors and Actuators*, vol. 3, no. C, 1982, doi: 10.1016/0250-6874(82)80008-5.
- [26] *Handbook of Surface Plasmon Resonance*. Royal Society of Chemistry, 2017.
- [27] “Biacore - Biaffin GmbH & Co KG.” <https://www.biaffin.com/techniques/biacore> (accessed Sep. 04, 2020).
- [28] S. Löfås, M. Malmqvist, I. Rönnerberg, E. Stenberg, B. Liedberg, and I. Lundström, “Bioanalysis with surface plasmon resonance,” *Sensors and Actuators: B. Chemical*, vol. 5, no. 1–4, pp. 79–84, 1991, doi: 10.1016/0925-4005(91)80224-8.
- [29] W. Lukosz, “Principles and sensitivities of integrated optical and surface plasmon sensors for direct affinity sensing and immunosensing,” *Biosensors and Bioelectronics*, vol. 6, no. 3, pp. 215–225, 1991, doi: 10.1016/0956-5663(91)80006-J.
- [30] M. T. Flanagan and R. H. Pantell, “Surface plasmon resonance and immunosensors,” *Electronics Letters*, vol. 20, no. 23, pp. 968–970, Nov. 1984, doi: 10.1049/el:19840660.
- [31] R. P. H. Kooyman, H. Kolkman, J. van Gent, and J. Greve, “Surface plasmon resonance immunosensors: sensitivity considerations,” *Analytica Chimica Acta*, vol. 213, no. C, pp. 35–45, 1988, doi: 10.1016/S0003-2670(00)81337-9.
- [32] E. Kretschmann, “The angular dependence and the polarisation of light emitted by surface plasmons on metals due to roughness,” *Optics Communications*, vol. 5, no. 5, pp. 331–336, Aug. 1972, doi: 10.1016/0030-4018(72)90026-0.

- [33] R. H. Ritchie, E. T. Arakawa, J. J. Cowan, and R. N. Hamm, “Surface-plasmon resonance effect in grating diffraction,” *Physical Review Letters*, vol. 21, no. 22, pp. 1530–1533, 1968, doi: 10.1103/PhysRevLett.21.1530.
- [34] H. Raether, G. Hohler, and E. A. Niekisch, “Surface Plasmons on Smooth and Rough Surfaces and on Gratings,” *Springer Tracts in Modern Physics*, vol. 111. p. 136, 1988, doi: 10.1007/BFb0048317.
- [35] B. A. Prabowo, A. Purwidyantri, and K. C. Liu, “Surface plasmon resonance optical sensor: A review on light source technology,” *Biosensors*, vol. 8, no. 3. MDPI AG, 2018, doi: 10.3390/bios8030080.
- [36] J. Zhang *et al.*, “Lipopolysaccharides detection on a grating-coupled surface plasmon resonance smartphone biosensor,” *Biosensors and Bioelectronics*, vol. 99, pp. 312–317, Jan. 2018, doi: 10.1016/j.bios.2017.07.048.
- [37] P. He, W. Qiao, L. Liu, and S. Zhang, “A highly sensitive surface plasmon resonance sensor for the detection of DNA and cancer cells by a target-triggered multiple signal amplification strategy,” *Chemical Communications*, vol. 50, no. 73, pp. 10718–10721, Aug. 2014, doi: 10.1039/c4cc04776a.
- [38] N. J. de Mol and M. J. E. Fischer, *Surface Plasmon Resonance: Methods and Protocols*. 2010.
- [39] H. Raether, “Surface plasmons on smooth surfaces,” 1988, pp. 4–39.
- [40] J. Homola, “Electromagnetic Theory of Surface Plasmons,” in *Springer Ser Chem Sens Biosens*, vol. 4, Springer, Berlin, Heidelberg, 2006, pp. 3–44.
- [41] “Surface Plasmon Resonance Based Sensors (October 5, 2006 edition) | Open Library.” https://openlibrary.org/books/OL9869020M/Surface_Plasmon_Resonance_Based_Sensors (accessed Nov. 04, 2020).

- [42] I. Pockrand, "Surface plasma oscillations at silver surfaces with thin transparent and absorbing coatings," *Surface Science*, vol. 72, no. 3, pp. 577–588, Apr. 1978, doi: 10.1016/0039-6028(78)90371-0.
- [43] M. G. Moharam and T. K. Gaylord, "Coupled-wave analysis of reflection gratings," *Applied Optics*, vol. 20, no. 2, p. 240, Jan. 1981, doi: 10.1364/ao.20.000240.
- [44] M. G. Moharam and T. K. Gaylord, "Rigorous coupled-wave analysis of planar-grating diffraction," 1981. Accessed: Dec. 13, 2020. [Online].
- [45] M. I. Markovic and A. D. Rakic, "Determination of the reflection coefficients of laser light of wavelengths $\lambda \in (0.22 \mu\text{m}, 200 \mu\text{m})$ from the surface of aluminum using the Lorentz-Drude model," *Applied Optics*, vol. 29, no. 24, p. 3479, Aug. 1990, doi: 10.1364/ao.29.003479.
- [46] M. A. Ordal *et al.*, "Optical properties of the metals Al, Co, Cu, Au, Fe, Pb, Ni, Pd, Pt, Ag, Ti, and W in the infrared and far infrared," *Applied Optics*, vol. 22, no. 7, p. 1099, Apr. 1983, doi: 10.1364/ao.22.001099.
- [47] W. H. Weber and S. L. McCarthy, "Surface-plasmon resonance as a sensitive optical probe of metal-film properties," *Physical Review B*, vol. 12, no. 12, pp. 5643–5650, Dec. 1975, doi: 10.1103/PhysRevB.12.5643.
- [48] J. Homola, I. Koudela, and S. S. Yee, "Surface plasmon resonance sensors based on diffraction gratings and prism couplers: sensitivity comparison," *Sensors and Actuators, B: Chemical*, vol. 54, no. 1, pp. 16–24, Jan. 1999, doi: 10.1016/S0925-4005(98)00322-0.
- [49] Schott AG, "SCHOTT Optical Glass Database, May 2019." Schott, Mainz, May 2019, Accessed: Oct. 10, 2020. [Online]. Available: https://www.schott.com/d/advanced_optics/ac85c64c-60a0-4113-a9df-23ee1be20428/1.17/schott-optical-glass-collection-datasheets-english-may-2019.pdf.

- [50] B. van der Gaag *et al.*, “Biosensors and multiple mycotoxin analysis,” *Food Control*, vol. 14, no. 4, pp. 251–254, Jun. 2003, doi: 10.1016/S0956-7135(03)00008-2.
- [51] R. Jha and A. K. Sharma, “Chalcogenide glass prism based SPR sensor with Ag-Au bimetallic nanoparticle alloy in infrared wavelength region,” *Journal of Optics A: Pure and Applied Optics*, vol. 11, no. 4, p. 7, Jan. 2009, doi: 10.1088/1464-4258/11/4/045502.
- [52] R. C. Jorgenson and S. S. Yee, “A fiber-optic chemical sensor based on surface plasmon resonance,” *Sensors and Actuators: B. Chemical*, vol. 12, no. 3, 1993, doi: 10.1016/0925-4005(93)80021-3.
- [53] F. Höök, B. Kasemo, T. Nylander, C. Fant, K. Sott, and H. Elwing, “Variations in coupled water, viscoelastic properties, and film thickness of a Mefp-1 protein film during adsorption and cross-linking: A quartz crystal microbalance with dissipation monitoring, ellipsometry, and surface plasmon resonance study,” *Analytical Chemistry*, vol. 73, no. 24, pp. 5796–5804, Dec. 2001, doi: 10.1021/ac0106501.
- [54] P. Pfeifer, U. Aldinger, G. Schwotzer, S. Diekmann, and P. Steinrücke, “Real time sensing of specific molecular binding using surface plasmon resonance spectroscopy,” *Sensors and Actuators, B: Chemical*, vol. 54, no. 1, pp. 166–175, Jan. 1999, doi: 10.1016/S0925-4005(98)00334-7.
- [55] K. Matsubara, S. Kawata, and S. Minami, “Optical chemical sensor based on surface plasmon measurement,” *Applied Optics*, vol. 27, no. 6, p. 1160, Mar. 1988, doi: 10.1364/ao.27.001160.
- [56] M. Piliarik, L. Párová, and J. Homola, “High-throughput SPR sensor for food safety,” *Biosensors and Bioelectronics*, vol. 24, no. 5, pp. 1399–1404, Jan. 2009, doi: 10.1016/j.bios.2008.08.012.

- [57] L. M. Zhang and D. Uttamchandani, "Optical Chemical Sensing Employing Surface Plasmon Resonance," *Electronics Letters*, vol. 24, no. 23, pp. 1469–1470, 1988, doi: 10.1049/el:19881004.
- [58] M. Daimon and A. Masumura, "Measurement of the refractive index of distilled water from the near-infrared region to the ultraviolet region," *Applied Optics*, vol. 46, no. 18, pp. 3811–3820, Jun. 2007, doi: 10.1364/AO.46.003811.
- [59] R. Röttgers, D. McKee, and C. Utschig, "Temperature and salinity correction coefficients for light absorption by water in the visible to infrared spectral region," *Optics Express*, vol. 22, no. 21, p. 25093, Oct. 2014, doi: 10.1364/oe.22.025093.
- [60] H. J. Liebe, G. A. Hufford, and T. Manabe, "A model for the complex permittivity of water at frequencies below 1 THz," *International Journal of Infrared and Millimeter Waves*, vol. 12, no. 7, pp. 659–675, Jul. 1991, doi: 10.1007/BF01008897.
- [61] P. D. T. Huibers, "Models for the wavelength dependence of the index of refraction of water," *Applied Optics*, vol. 36, no. 16, p. 3785, Jun. 1997, doi: 10.1364/ao.36.003785.
- [62] A. B. Djurišić and B. v. Stanić, "Modeling the wavelength dependence of the index of refraction of water in the range 200 nm to 200 μm ," *Applied Optics*, vol. 37, no. 13, p. 2696, May 1998, doi: 10.1364/ao.37.002696.
- [63] U. Kaatze, "Complex Permittivity of Water as a Function of Frequency and Temperature," *Journal of Chemical and Engineering Data*, vol. 34, no. 4, pp. 371–374, Oct. 1989, doi: 10.1021/je00058a001.
- [64] J. Homola, "Present and future of surface plasmon resonance biosensors," *Analytical and Bioanalytical Chemistry*, vol. 377, no. 3. Springer, pp. 528–539, Oct. 19, 2003, doi: 10.1007/s00216-003-2101-0.

- [65] P. R. West, S. Ishii, G. v. Naik, N. K. Emani, V. M. Shalaev, and A. Boltasseva, "Searching for better plasmonic materials," *Laser and Photonics Reviews*, vol. 4, no. 6. pp. 795–808, Nov. 2010, doi: 10.1002/lpor.200900055.
- [66] S. K. Özdemir and G. Turhan-Sayan, "Temperature effects on surface plasmon resonance: Design considerations for an optical temperature sensor," in *Journal of Lightwave Technology*, Mar. 2003, vol. 21, no. 3, pp. 805–814, doi: 10.1109/JLT.2003.809552.
- [67] S. Chen, Y. Liu, Q. Liu, and W. Peng, "Temperature-compensating fiber-optic surface plasmon resonance biosensor," *IEEE Photonics Technology Letters*, vol. 28, no. 2, pp. 213–216, Jan. 2016, doi: 10.1109/LPT.2015.2492603.
- [68] K. Q. Lin *et al.*, "Temperature effects on prism-based surface plasmon resonance sensor," *Chinese Physics Letters*, vol. 24, no. 11, pp. 3081–3084, Nov. 2007, doi: 10.1088/0256-307X/24/11/018.
- [69] W. Knoll, "INTERFACES AND THIN FILMS AS SEEN BY BOUND ELECTROMAGNETIC WAVES," *Annual Review of Physical Chemistry*, vol. 49, no. 1, pp. 569–638, Oct. 1998, doi: 10.1146/annurev.physchem.49.1.569.
- [70] X. Fan, I. M. White, S. I. Shopova, H. Zhu, J. D. Suter, and Y. Sun, "Sensitive optical biosensors for unlabeled targets: A review," *Analytica Chimica Acta*, vol. 620, no. 1–2. Elsevier, pp. 8–26, Jul. 14, 2008, doi: 10.1016/j.aca.2008.05.022.
- [71] K. A. Peterlinz and R. Georgiadis, "In Situ Kinetics of Self-Assembly by Surface Plasmon Resonance Spectroscopy," 1996. Accessed: Dec. 14, 2020. [Online]. Available: <https://pubs.acs.org/sharingguidelines>.
- [72] D. Zacher, O. Shekhah, C. Wöll, and R. A. Fischer, "Thin films of metal–organic frameworks," *Chemical Society Reviews*, vol. 38, no. 5, pp. 1418–1429, Apr. 2009, doi: 10.1039/b805038b.

- [73] L. S. Jung, C. T. Campbell, T. M. Chinowsky, M. N. Mar, and S. S. Yee, “Quantitative interpretation of the response of surface plasmon resonance sensors to adsorbed films,” *Langmuir*, vol. 14, no. 19, pp. 5636–5648, Sep. 1998, doi: 10.1021/la971228b.
- [74] J. Homola, “Surface plasmon resonance sensors for detection of chemical and biological species,” *Chemical Reviews*, vol. 108, no. 2, pp. 462–493, Feb. 2008, doi: 10.1021/cr068107d.
- [75] E. Hutter and J. H. Fendler, “Exploitation of localized surface plasmon resonance,” *Advanced Materials*, vol. 16, no. 19, pp. 1685–1706, Oct. 2004, doi: 10.1002/adma.200400271.
- [76] N. Nath and A. Chilkoti, “A colorimetric gold nanoparticle sensor to interrogate biomolecular interactions in real time on a surface,” *Analytical Chemistry*, vol. 74, no. 3, pp. 504–509, Feb. 2002, doi: 10.1021/ac015657x.
- [77] O. Lazcka, F. J. del Campo, and F. X. Muñoz, “Pathogen detection: A perspective of traditional methods and biosensors,” *Biosensors and Bioelectronics*, vol. 22, no. 7, pp. 1205–1217, Feb. 15, 2007, doi: 10.1016/j.bios.2006.06.036.
- [78] R. Karlsson, A. Michaelsson, and L. Mattsson, “Kinetic analysis of monoclonal antibody-antigen interactions with a new biosensor based analytical system,” *Journal of Immunological Methods*, vol. 145, no. 1–2, pp. 229–240, Dec. 1991, doi: 10.1016/0022-1759(91)90331-9.
- [79] A. D. McFarland and R. P. van Duyne, “Single silver nanoparticles as real-time optical sensors with zeptomole sensitivity,” *Nano Letters*, vol. 3, no. 8, pp. 1057–1062, Aug. 2003, doi: 10.1021/nl034372s.
- [80] B. Liedberg, I. Lundström, and E. Stenberg, “Principles of biosensing with an extended coupling matrix and surface plasmon resonance,” *Sensors and Actuators: B. Chemical*, vol. 11, no. 1–3, 1993, doi: 10.1016/0925-4005(93)85239-7.

- [81] S. Zeng *et al.*, “Graphene-MoS₂ hybrid nanostructures enhanced surface plasmon resonance biosensors,” *Sensors and Actuators, B: Chemical*, vol. 207, no. PartA, pp. 801–810, Feb. 2015, doi: 10.1016/j.snb.2014.10.124.
- [82] C. E. H. Berger and J. Greve, “Differential SPR immunosensing,” *Sensors and Actuators, B: Chemical*, vol. 63, no. 1, pp. 103–108, Apr. 2000, doi: 10.1016/S0925-4005(00)00307-5.
- [83] A. Kuzyk *et al.*, “DNA-based self-assembly of chiral plasmonic nanostructures with tailored optical response,” *Nature*, vol. 483, no. 7389, 2012, doi: 10.1038/nature10889.
- [84] S. Zeng, D. Baillargeat, H. P. Ho, and K. T. Yong, “Nanomaterials enhanced surface plasmon resonance for biological and chemical sensing applications,” *Chemical Society Reviews*, vol. 43, no. 10. Royal Society of Chemistry, pp. 3426–3452, May 21, 2014, doi: 10.1039/c3cs60479a.
- [85] S. Zhang, K. Bao, N. J. Halas, H. Xu, and P. Nordlander, “Substrate-induced Fano resonances of a plasmonic nanocube: A route to increased-sensitivity localized surface plasmon resonance sensors revealed,” *Nano Letters*, vol. 11, no. 4, pp. 1657–1663, Apr. 2011, doi: 10.1021/nl200135r.
- [86] R. C. Jorgenson and S. S. Yee, “A fiber-optic chemical sensor based on surface plasmon resonance,” *Sensors and Actuators: B. Chemical*, vol. 12, no. 3, pp. 213–220, Apr. 1993, doi: 10.1016/0925-4005(93)80021-3.
- [87] P. Zijlstra, P. M. R. Paulo, and M. Orrit, “Optical detection of single non-absorbing molecules using the surface plasmon resonance of a gold nanorod,” *Nature Nanotechnology*, vol. 7, no. 6, 2012, doi: 10.1038/nnano.2012.51.
- [88] M. Manuel *et al.*, “Determination of probable alcohol yield in musts by means of an SPR optical sensor,” *Sensors and Actuators: B. Chemical*, vol. 11, no. 1–3, 1993, doi: 10.1016/0925-4005(93)85287-K.

- [89] R. Kaňok, D. Ciprian, and P. Hlubina, “Sensing of liquid analytes via the phase shift induced by surface plasmon resonance,” 2018, doi: 10.1117/12.2305718.
- [90] S. Shen, T. Liu, and J. Guo, “Optical phase-shift detection of surface plasmon resonance,” *Applied Optics*, vol. 37, no. 10, 1998, doi: 10.1364/AO.37.001747.
- [91] A. K. Sheridan, R. D. Harris, P. N. Bartlett, and J. S. Wilkinson, “Phase interrogation of an integrated optical SPR sensor,” *Sensors and Actuators, B: Chemical*, vol. 97, no. 1, 2004, doi: 10.1016/j.snb.2003.08.005.
- [92] C.-M. Wu and M.-C. Pao, “Sensitivity-tunable optical sensors based on surface plasmon resonance and phase detection,” *Optics Express*, vol. 12, no. 15, p. 3509, 2004, doi: 10.1364/opex.12.003509.
- [93] S. G. Nelson, K. S. Johnston, and S. S. Yee, “High sensitivity surface plasmon resonance sensor based on phase detection,” *Sensors and Actuators, B: Chemical*, vol. 35, no. 1–3, 1996, doi: 10.1016/S0925-4005(97)80052-4.
- [94] A. v. Kabashin, V. E. Kochergin, A. A. Beloglazov, and P. I. Nikitin, “Phase-polarisation contrast for surface plasmon resonance biosensors,” *Biosensors and Bioelectronics*, vol. 13, no. 12, 1998, doi: 10.1016/S0956-5663(98)00088-8.
- [95] F. Fernández, K. Hegnerová, M. Piliarik, F. Sanchez-Baeza, J. Homola, and M. P. Marco, “A label-free and portable multichannel surface plasmon resonance immunosensor for on site analysis of antibiotics in milk samples,” *Biosensors and Bioelectronics*, vol. 26, no. 4, pp. 1231–1238, Dec. 2010, doi: 10.1016/j.bios.2010.06.012.
- [96] J. Dostálek, H. Vaisocherová, and J. Homola, “Multichannel surface plasmon resonance biosensor with wavelength division multiplexing,” in *Sensors and Actuators, B: Chemical*, Jul. 2005, vol. 108, no. 1-2 SPEC. ISS., pp. 758–764, doi: 10.1016/j.snb.2004.12.096.

- [97] J. Homola, H. B. Lu, G. G. Nenninger, J. Dostálek, and S. S. Yee, “A novel multichannel surface plasmon resonance biosensor,” in *Sensors and Actuators, B: Chemical*, Jun. 2001, vol. 76, no. 1–3, pp. 403–410, doi: 10.1016/S0925-4005(01)00648-7.
- [98] Y. G. Kim, J. Jung, M. H. Oh, S. K. Lee, and M. Taya, “A novel surface plasmon resonance multisensing by multichannels,” in *Digest of Technical Papers - International Conference on Solid State Sensors and Actuators and Microsystems, TRANSDUCERS '05*, 2005, vol. 2, pp. 1800–1803, doi: 10.1109/sensor.2005.1497443.
- [99] P. Chang *et al.*, “The temperature responsive mechanism of fiber surface plasmon resonance sensor,” *Sensors and Actuators, A: Physical*, vol. 309, p. 112022, Jul. 2020, doi: 10.1016/j.sna.2020.112022.
- [100] Y. Shao *et al.*, “Mechanism and Characteristics of Humidity Sensing with Polyvinyl Alcohol-Coated Fiber Surface Plasmon Resonance Sensor,” *Sensors*, vol. 18, no. 7, p. 2029, Jun. 2018, doi: 10.3390/s18072029.
- [101] A. K. Sharma and A. Gupta, “Design of a plasmonic optical sensor probe for humidity-monitoring,” *Sensors and Actuators, B: Chemical*, vol. 188, pp. 867–871, Nov. 2013, doi: 10.1016/j.snb.2013.08.002.
- [102] Z. Zhang, P. Zhao, F. Sun, G. Xiao, and Y. Wu, “Self-referencing in optical-fiber surface plasmon resonance sensors,” *IEEE Photonics Technology Letters*, vol. 19, no. 24, pp. 1958–1960, Dec. 2007, doi: 10.1109/LPT.2007.909669.
- [103] P. Zhang, B. Lu, Y. Sun, H. Yu, K. Xu, and D. Li, “Side-polished flexible SPR sensor modified by graphene with in situ temperature self-compensation,” *Biomedical Optics Express*, vol. 10, no. 1, p. 215, Jan. 2019, doi: 10.1364/boe.10.000215.
- [104] A. N. Naimushin, S. D. Soelberg, D. U. Bartholomew, J. L. Elkind, and C. E. Furlong, “A portable surface plasmon resonance (SPR) sensor system with

- temperature regulation,” *Sensors and Actuators, B: Chemical*, vol. 96, no. 1–2, pp. 253–260, Nov. 2003, doi: 10.1016/S0925-4005(03)00533-1.
- [105] Q. Wang, J. Y. Jing, X. Z. Wang, L. Y. Niu, and W. M. Zhao, “A D-Shaped Fiber Long-Range Surface Plasmon Resonance Sensor with High Q-Factor and Temperature Self-Compensation,” *IEEE Transactions on Instrumentation and Measurement*, vol. 69, no. 5, pp. 2218–2224, May 2020, doi: 10.1109/TIM.2019.2920187.
- [106] M. Piliarik and J. Homola, “Surface plasmon resonance (SPR) sensors: approaching their limits?,” *Optics Express*, vol. 17, no. 19, p. 16505, Sep. 2009, doi: 10.1364/oe.17.016505.
- [107] C. E. H. Berger, T. A. M. Beumer, R. P. H. Kooyman, and J. Greve, “Surface Plasmon Resonance Multisensing,” *Analytical Chemistry*, vol. 70, no. 4, pp. 703–706, Feb. 1998, doi: 10.1021/ac970929a.
- [108] R. Otupiri, E. K. Akowuah, and S. Haxha, “Multi-channel SPR biosensor based on PCF for multi-analyte sensing applications,” *Optics Express*, vol. 23, no. 12, 2015, doi: 10.1364/oe.23.015716.
- [109] J. Homola, H. Vaisocherová, J. Dostálek, and M. Piliarik, “Multi-analyte surface plasmon resonance biosensing,” *Methods*, vol. 37, no. 1, 2005, doi: 10.1016/j.ymeth.2005.05.003.
- [110] J. Hammond, N. Bhalla, S. Rafiee, and P. Estrela, “Localized Surface Plasmon Resonance as a Biosensing Platform for Developing Countries,” *Biosensors*, vol. 4, no. 2, pp. 172–188, Jun. 2014, doi: 10.3390/bios4020172.
- [111] M. Trzaskowski, A. Napiórkowska, E. Augustynowicz-Kopeć, and T. Ciach, “Detection of tuberculosis in patients with the use of portable SPR device,” *Sensors and Actuators, B: Chemical*, vol. 260, pp. 786–792, May 2018, doi: 10.1016/j.snb.2017.12.183.

- [112] M. Moznuzzaman, M. Rafiqul Islam, M. Biplob Hossain, and I. Mustafa Mehedi, “Modeling of highly improved SPR sensor for formalin detection,” *Results in Physics*, vol. 16, p. 102874, Mar. 2020, doi: 10.1016/j.rinp.2019.102874.
- [113] W. G. Lee, Y. G. Kim, B. G. Chung, U. Demirci, and A. Khademhosseini, “Nano/Microfluidics for diagnosis of infectious diseases in developing countries,” *Advanced Drug Delivery Reviews*, vol. 62, no. 4–5. Elsevier, pp. 449–457, Mar. 18, 2010, doi: 10.1016/j.addr.2009.11.016.
- [114] “MATLAB - MathWorks - MATLAB & Simulink.” <https://www.mathworks.com/products/matlab.html> (accessed Jan. 15, 2021).
- [115] “CST Studio Suite 3D EM simulation and analysis software.” <https://www.3ds.com/products-services/simulia/products/cst-studio-suite/> (accessed Jan. 08, 2021).
- [116] L. Novotny, B. Hecht, L. Novotny, and B. Hecht, “Surface plasmons,” in *Principles of Nano-Optics*, Cambridge University Press, 2012, pp. 369–413.
- [117] S. J. Orfanidis, D. Ramaccia, and A. Toscano, “Electromagnetic Waves and Antennas Exercise book,” 2002. Accessed: Jan. 08, 2021. [Online]. Available: www.ece.rutgers.edu/~orfanidi/ewa.
- [118] J. Homola, “Electromagnetic Theory of Surface Plasmons,” 2006, pp. 3–44.
- [119] E. D. Palik, *Handbook of optical constants of solids*, vol. 1, Academic Press, 2012.
- [120] O. S. Heavens, “Handbook of Optical Constants of Solids II,” *Journal of Modern Optics*, vol. 39, no. 1, 1992, doi: 10.1080/716099804a.
- [121] X. Y. He, Q. J. Wang, and S. F. Yu, “Analysis of dielectric loaded surface plasmon waveguide structures: Transfer matrix method for plasmonic

- devices,” in *Journal of Applied Physics*, Apr. 2012, vol. 111, no. 7, p. 073108, doi: 10.1063/1.3703468.
- [122] Ş. K. Özdemir, “Surface plasmon resonance theory and applications in optical sensing,” Ankara, 1995.
- [123] J. Čtyroký *et al.*, “Theory and modelling of optical waveguide sensors utilising surface plasmon resonance,” *Sensors and Actuators, B: Chemical*, vol. 54, no. 1, pp. 66–73, Jan. 1999, doi: 10.1016/S0925-4005(98)00328-1.
- [124] A. Suzuki, J. Kondoh, Y. Matsui, S. Shiokawa, and K. Suzuki, “Development of novel optical waveguide surface plasmon resonance (SPR) sensor with dual light emitting diodes,” in *Sensors and Actuators, B: Chemical*, Apr. 2005, vol. 106, no. 1 SPEC. ISS., pp. 383–387, doi: 10.1016/j.snb.2004.08.021.
- [125] T. Hu, Y. Zhao, and A. ning Song, “Fiber optic SPR sensor for refractive index and temperature measurement based on MMF-FBG-MMF structure,” *Sensors and Actuators, B: Chemical*, vol. 237, pp. 521–525, Dec. 2016, doi: 10.1016/j.snb.2016.06.119.
- [126] J. Pollet *et al.*, “Fiber optic SPR biosensing of DNA hybridization and DNA-protein interactions,” *Biosensors and Bioelectronics*, vol. 25, no. 4, pp. 864–869, Dec. 2009, doi: 10.1016/j.bios.2009.08.045.
- [127] Y. Zhao, Z. Q. Deng, and H. F. Hu, “Fiber-Optic SPR Sensor for Temperature Measurement,” *IEEE Transactions on Instrumentation and Measurement*, vol. 64, no. 11, pp. 3099–3104, Nov. 2015, doi: 10.1109/TIM.2015.2434094.
- [128] Y. Zhao, Z. Q. Deng, and Q. Wang, “Fiber optic SPR sensor for liquid concentration measurement,” *Sensors and Actuators, B: Chemical*, vol. 192, pp. 229–233, Mar. 2014, doi: 10.1016/j.snb.2013.10.108.
- [129] Y. Li, *Plasmonic Optics: Theory and Applications*. SPIE, 2017.

- [130] B. H. Ong, X. Yuan, S. C. Tjin, J. Zhang, and H. M. Ng, "Optimised film thickness for maximum evanescent field enhancement of a bimetallic film surface plasmon resonance biosensor," *Sensors and Actuators, B: Chemical*, vol. 114, no. 2, pp. 1028–1034, Apr. 2006, doi: 10.1016/j.snb.2005.07.064.
- [131] S. Zynio, A. Samoylov, E. Surovtseva, V. Mirsky, and Y. Shirshov, "Bimetallic Layers Increase Sensitivity of Affinity Sensors Based on Surface Plasmon Resonance," *Sensors*, vol. 2, no. 2, pp. 62–70, Feb. 2002, doi: 10.3390/s20200062.
- [132] K. S. Lee, J. M. Son, D. Y. Jeong, T. S. Lee, and W. M. Kim, "Resolution enhancement in surface plasmon resonance sensor based on waveguide coupled mode by combining a bimetallic approach," *Sensors*, vol. 10, no. 12, pp. 11390–11399, Dec. 2010, doi: 10.3390/s101211390.
- [133] E. M. Yeatman, "Resolution and sensitivity in surface plasmon microscopy and sensing," in *Biosensors and Bioelectronics*, Jan. 1996, vol. 11, no. 6–7, pp. 635–649, doi: 10.1016/0956-5663(96)83298-2.
- [134] K. Johansen, H. Arwin, I. Lundström, and B. Liedberg, "Imaging surface plasmon resonance sensor based on multiple wavelengths: Sensitivity considerations," *Review of Scientific Instruments*, vol. 71, no. 9, pp. 3530–3538, Sep. 2000, doi: 10.1063/1.1287631.
- [135] K. Johansen, R. Stålberg, I. Lundström, and B. Liedberg, "Surface plasmon resonance: Instrumental resolution using photo diode arrays," *Measurement Science and Technology*, vol. 11, no. 11, pp. 1630–1638, Nov. 2000, doi: 10.1088/0957-0233/11/11/313.
- [136] B. Ran and S. G. Lipson, "Comparison between sensitivities of phase and intensity detection in surface plasmon resonance," *Optics Express*, vol. 14, no. 12, p. 5641, Jun. 2006, doi: 10.1364/oe.14.005641.
- [137] T. M. Chinowsky, J. G. Quinn, D. U. Bartholomew, R. Kaiser, and J. L. Elkind, "Performance of the Spreeta 2000 integrated surface plasmon

- resonance affinity sensor,” *Sensors and Actuators, B: Chemical*, vol. 91, no. 1–3, pp. 266–274, Jun. 2003, doi: 10.1016/S0925-4005(03)00113-8.
- [138] I. Stemmler, A. Brecht, and G. Gauglitz, “Compact surface plasmon resonance-transducers with spectral readout for biosensing applications,” *Sensors and Actuators, B: Chemical*, vol. 54, no. 1, pp. 98–105, Jan. 1999, doi: 10.1016/S0925-4005(98)00317-7.
- [139] C. Thirstrup and W. Zong, “Data analysis for surface plasmon resonance sensors using dynamic baseline algorithm,” *Sensors and Actuators, B: Chemical*, vol. 106, no. 2, pp. 796–802, May 2005, doi: 10.1016/j.snb.2004.09.032.
- [140] G. G. Nenninger, M. Piliarik, and J. Homola, “Data analysis for optical sensors based on spectroscopy of surface plasmons,” *Measurement Science and Technology*, vol. 13, no. 12, pp. 2038–2046, Nov. 2002, doi: 10.1088/0957-0233/13/12/332.
- [141] F. Bardin, A. Bellemain, G. Roger, and M. Canva, “Surface plasmon resonance spectro-imaging sensor for biomolecular surface interaction characterization,” *Biosensors and Bioelectronics*, vol. 24, no. 7, pp. 2100–2105, Mar. 2009, doi: 10.1016/j.bios.2008.10.023.
- [142] M. Piliarik, M. Vala, I. Tichý, and J. Homola, “Compact and low-cost biosensor based on novel approach to spectroscopy of surface plasmons,” *Biosensors and Bioelectronics*, vol. 24, no. 12, pp. 3430–3435, Aug. 2009, doi: 10.1016/j.bios.2008.11.003.
- [143] “Permittivity - Wikipedia.” <https://en.wikipedia.org/wiki/Permittivity> (accessed Jan. 30, 2021).
- [144] F. Wooten, *OPTICAL PROPERTIES OF SOLIDS*, 1st ed. Academic Press, 1972.
- [145] P. Drude, *The Theory of Optics*. New York: Longmans Green, 1922.

- [146] Y. Li, “Optical Properties of Plasmonic Materials,” in *Plasmonic Optics Theory and Applications*, SPIE PRESS, 2017, pp. 1–41.
- [147] A. D. Rakić, A. B. Djurišić, J. M. Elazar, and M. L. Majewski, “Optical properties of metallic films for vertical-cavity optoelectronic devices,” *Applied Optics*, vol. 37, no. 22, p. 5271, Aug. 1998, doi: 10.1364/ao.37.005271.
- [148] B. Ung and Y. Sheng, “Interference of surface waves in a metallic nanoslit,” *Optics Express*, vol. 15, no. 3, p. 1182, Feb. 2007, doi: 10.1364/oe.15.001182.
- [149] H. U. Yang, J. D’Archangel, M. L. Sundheimer, E. Tucker, G. D. Boreman, and M. B. Raschke, “Optical dielectric function of silver,” *Physical Review B - Condensed Matter and Materials Physics*, vol. 91, no. 23, p. 235137, Jun. 2015, doi: 10.1103/PhysRevB.91.235137.
- [150] D. Gerard and S. K. Gray, “Aluminium plasmonics,” *Journal of Physics D: Applied Physics*, vol. 48, no. 18, p. 184001, May 2015, doi: 10.1088/0022-3727/48/18/184001.
- [151] J. Zhao, S. Wan, and S. Li, “Investigation of SPR mechanical performance with aluminum alloy sheet,” in *Applied Mechanics and Materials*, 2010, vol. 37–38, pp. 599–602, doi: 10.4028/www.scientific.net/AMM.37-38.599.
- [152] B. Meshginqalam and J. Barvestani, “Aluminum and phosphorene based ultrasensitive SPR biosensor,” *Optical Materials*, vol. 86, pp. 119–125, Dec. 2018, doi: 10.1016/j.optmat.2018.10.003.
- [153] P. F. Robusto and R. Braunstein, “Optical measurements of the surface plasmon of copper,” *physica status solidi (b)*, vol. 107, no. 2, pp. 443–449, Oct. 1981, doi: 10.1002/pssb.2221070207.
- [154] D. B. Pedersen and S. Wang, “Surface plasmon resonance spectra of 2.8 ± 0.5 nm diameter copper nanoparticles in both near and far fields,” *Journal of*

- Physical Chemistry C*, vol. 111, no. 47, pp. 17493–17499, Nov. 2007, doi: 10.1021/jp075076x.
- [155] R. Boidin, T. Halenkovič, V. Nazabal, L. Beneš, and P. Němec, “Pulsed laser deposited alumina thin films,” *Ceramics International*, vol. 42, no. 1, pp. 1177–1182, Jan. 2016, doi: 10.1016/j.ceramint.2015.09.048.
- [156] “The index of refraction of seawater.” <https://escholarship.org/uc/item/8px2019m> (accessed Oct. 09, 2020).
- [157] X. Quan and E. S. Fry, “Empirical equation for the index of refraction of seawater,” *Applied Optics*, vol. 34, no. 18, p. 3477, Jun. 1995, doi: 10.1364/ao.34.003477.
- [158] J. v. Leyendekkers, “Prediction of the refractive index of seawater as a function of temperature, pressure, salinity and wavelength,” *Marine Chemistry*, vol. 5, no. 1, pp. 29–42, Feb. 1977, doi: 10.1016/0304-4203(77)90013-5.
- [159] W. S. Pegau, D. Gray, J. Ronald, and V. Zaneveld, “Absorption and attenuation of visible and near-infrared light in water: dependence on temperature and salinity,” 1997. Accessed: Oct. 09, 2020. [Online].
- [160] R. M. Pope and E. S. Fry, “Absorption spectrum (380–700 nm) of pure water II Integrating cavity measurements,” *Applied Optics*, vol. 36, no. 33, p. 8710, Nov. 1997, doi: 10.1364/ao.36.008710.
- [161] V. Ball and J. J. Ramsden, “Buffer dependence of refractive index increments of protein solutions,” *Biopolymers*, vol. 46, no. 7, pp. 489–492, Dec. 1998, doi: 10.1002/(sici)1097-0282(199812)46:7<489::aid-bip6>3.0.co;2-e.
- [162] R. L. Qian, R. Mhatre, and I. S. Krull, “Characterization of antigen-antibody complexes by size-exclusion chromatography coupled with low-angle light-scattering photometry and viscometry,” *Journal of*

- Chromatography A*, vol. 787, no. 1–2, pp. 101–109, Nov. 1997, doi: 10.1016/S0021-9673(97)00666-3.
- [163] J. A. de Feijter, J. Benjamins, and F. A. Veer, “Ellipsometry as a tool to study the adsorption behavior of synthetic and biopolymers at the air–water interface,” *Biopolymers*, vol. 17, no. 7, pp. 1759–1772, Jul. 1978, doi: 10.1002/bip.1978.360170711.
- [164] R. Somaraju and J. Trumpf, “Frequency, temperature and salinity variation of the permittivity of seawater,” *IEEE Transactions on Antennas and Propagation*, vol. 54, no. 11, pp. 3441–3448, 2006, doi: 10.1109/TAP.2006.884290.
- [165] G. T. McNeil, “Metrical Fundamentals of Underwater Lens System,” *Optical Engineering*, vol. 16, no. 2, p. 162128, Apr. 1977, doi: 10.1117/12.7972089.
- [166] S. Carrara, *Nano-bio-sensing*. Springer, 2011.
- [167] T. Akimoto, S. Sasaki, K. Ikebukuro, and I. Karube, “Effect of incident angle of light on sensitivity and detection limit for layers of antibody with surface plasmon resonance spectroscopy,” *Biosensors and Bioelectronics*, vol. 15, no. 7–8, pp. 355–362, Oct. 2000, doi: 10.1016/S0956-5663(00)00091-9.
- [168] H. Chen, J. Huang, J. Lee, S. Hwang, and K. Koh, “Surface plasmon resonance spectroscopic characterization of antibody orientation and activity on the calixarene monolayer,” *Sensors and Actuators, B: Chemical*, vol. 147, no. 2, pp. 548–553, Jun. 2010, doi: 10.1016/j.snb.2010.03.033.
- [169] T. Srivastava, R. Jha, and R. Das, “High-performance bimetallic SPR sensor based on periodic-multilayer-waveguides,” *IEEE Photonics Technology Letters*, vol. 23, no. 20, pp. 1448–1450, 2011, doi: 10.1109/LPT.2011.2162828.

- [170] D. Monzón-Hernández and J. Villatoro, “High-resolution refractive index sensing by means of a multiple-peak surface plasmon resonance optical fiber sensor,” *Sensors and Actuators, B: Chemical*, vol. 115, no. 1, pp. 227–231, May 2006, doi: 10.1016/j.snb.2005.09.006.
- [171] D. Monzón-Hernández, J. Villatoro, D. Talavera, and D. Luna-Moreno, “Optical-fiber surface-plasmon resonance sensor with multiple resonance peaks,” *Applied Optics*, vol. 43, no. 6, pp. 1216–1220, Feb. 2004, doi: 10.1364/AO.43.001216.
- [172] P. Adam, J. Dostálek, and J. Homola, “Multiple surface plasmon spectroscopy for study of biomolecular systems,” *Sensors and Actuators, B: Chemical*, vol. 113, no. 2, pp. 774–781, Feb. 2006, doi: 10.1016/j.snb.2005.07.029.
- [173] S. J. Kim, K. V. Gobi, H. Iwasaka, H. Tanaka, and N. Miura, “Novel miniature SPR immunosensor equipped with all-in-one multi-microchannel sensor chip for detecting low-molecular-weight analytes,” *Biosensors and Bioelectronics*, vol. 23, no. 5, pp. 701–707, Dec. 2007, doi: 10.1016/j.bios.2007.08.010.
- [174] C. Boozer, J. Ladd, S. Chen, and S. Jiang, “DNA-directed protein immobilization for simultaneous detection of multiple analytes by surface plasmon resonance biosensor,” *Analytical Chemistry*, vol. 78, no. 5, pp. 1515–1519, Mar. 2006, doi: 10.1021/ac051923l.
- [175] T. M. Chinowsky, “Optical multisensors based on surface plasmon resonance,” 2000.

APPENDIX

A. SUM OF GEOMETRIC SERIES

Sum of the infinite geometric series required to calculate the exact result of the infinite number of reflections analytically, in a bouncing-system as explained in Chapter 2. Geometric series with k-terms can be expressed as

$$a u^n = a u, a u^1, a u^2, a u^3, a u^4, \dots, a u^k \quad (\text{A.1})$$

and the sum of the geometric series required In Chapter 2 can be expressed as

$$\sum_{n=0}^k (a u^n) = a u + a u^1 + a u^2 + a u^3 + \dots a u^n + \dots a u^{k-1} a u^k \quad (\text{A.2})$$

In the case of the geometric series in Equation 2.38, i.e., when $k \rightarrow \infty$, the series only has a solution if

$$-1 < u < 1 \quad (\text{A.3a})$$

$$u \neq 0 \quad (\text{A.3b})$$

These conditions are satisfied simultaneously for SPR calculations since u is the reflection coefficient, and the reflection coefficient automatically satisfies both conditions as its magnitude never becomes 1 or 0 due to imperfections on real materials. Hence, if the conditions given in Equation A.3 is satisfied, the sum of the geometric series given in Equation A.2 can be expressed as

$$\sum_{n=0}^{\infty} (a u^n) = a \left(\frac{1}{1-u} \right) \quad (\text{A.4})$$

Now, rewriting Equation 2.48:

$$r_{tot} = r_{123} = r_{12} + t_{12}t_{21}r_{12} \sum_{n=0}^{\infty} (a u^n) \quad (\text{A.5})$$

where $a=1$ and

$$\exp(-2nj k_{2x} d) = \exp(-2j k_{2x} d)^n \quad (\text{A.6a})$$

$$u^n = r_{12}^n r_{23}^n \exp(-2j k_{2x} d)^n \quad (\text{A.6b})$$

Substituting Equation A.4 into A.5

$$r_{123} = r_{12} + t_{12}t_{21}r_{12} \frac{1}{1-u} \quad (\text{A.7})$$

and substituting Equation A.6 into A.7

$$r_{123} = r_{12} + t_{12}t_{21}r_{12} \frac{1}{1 - r_{12}r_{23} \exp(-2j k_{2x} d)} \quad (\text{A.8})$$

Rearranging Equation A.8

$$r_{123} = r_{12} + \frac{t_{12}t_{21}r_{12}}{1 - r_{12}r_{23} \exp(-2j k_{2x} d)} \quad (\text{A.9})$$

